2014

A spatial and economic analysis for land conservation planning

Sudiksha Joshi

GROWTH OF NIOBIUM DIOXIDE THIN FILMS
AND THEIR METAL-TO-INSULATOR
TRANSITIONS INDUCED BY ELECTRIC FIELD

Toyanath Joshi

Dissertation submitted to the Eberly College of Art and Science
at West Virginia University
in partial fulfillment of the requirements
for the degree of

Doctor of Philosophy

in

Physics

David Lederman, Ph.D., Committee Chairperson

Mohindar Seehra, Ph.D.

Matthew Johnson, Ph.D.

Cheng Cen, Ph.D.

Fabien Goulay, Ph.D.

Department of Physics and Astronomy

Morgantown, West Virginia

2017

ABSTRACT

GROWTH OF NIOBIUM DIOXIDE THIN FILMS AND THEIR METAL-TO-INSULATOR TRANSITIONS INDUCED BY ELECTRIC FIELD

Toyanath Joshi

The 4d transition metal oxide, NbO_2, is a key material for a wide range of potential applications. It exhibits a thermally driven metal-to-insulator transition (MIT) with very high transition temperature (T_{MIT} = 1083 K). High T_{MIT}, electric field induced sharp threshold switching and current-controlled negative differential resistance (NDR) characteristics makes this material most suitable for current switching devices. Metal-to-insulator transition in NbO_2 is accompanied by a structural transition from a rutile (high temperature) to a tetragonal (low temperature) structure with lowering temperature. In this work, pulsed laser deposition growth of NbO_2 thin films and their structural and electrical characterization were investigated.

To study the switching mechanism in epitaxial NbO_2 (110) film lateral devices, 20 nm thick films were grown by pulsed laser deposition on Al_2O_3 (0001) substrates. The Ar/O_2 total pressure during growth was varied to demonstrate the gradual transformation between NbO_2 and Nb_2O_5 phases, which was verified using x-ray diffraction, x-ray photoelectron spectroscopy, and optical absorption measurements. Electrical resistance threshold switching in current characteristics was studied in a lateral geometry using interdigitated Pt top electrodes to preserve the epitaxial crystalline quality of the films. Volatile and reversible transitions between high and

low resistance states were observed in epitaxial NbO_2 films, while irreversible transitions were found in the case of Nb_2O_5 phase. Electric field pulsed current measurements confirmed thermally-induced threshold switching.

Switching mechanism in the polycrystalline thin film of NbO_2 was also investigated. Polycrystalline thin films were grown on the TiN coated SiO_2/Si substrate using pulsed laser deposition. Thickness and contact size dependent study in threshold switching in current characteristics of NbO_2 films grown using different growth pressures were performed. Threshold switching and current oscillations produced by the films having different defect densities were measured and compared. To increase defect density, such as oxygen vacancies, films grown in different growth pressures or using different oxygen mass flow ratios were used.

Finally, electrical properties of the polycrystalline thin film were compared with the epitaxial films grown using similar growth conditions. The epitaxial film was grown on Si-doped GaN coated substrate where Si:GaN layer acted as the bottom contact. Pulsed *I-V* as well as the input voltage dependent and time dependent frequency measurements were performed and compared with each other. Stability and switching rapidity of the thin film vertical devices were analyzed and compared in terms of the defect density presented in the film.

Dedicated to my mother

Harina Devi Joshi

ममतामयी आमा

हरिना देवी जोशी

मा सादर समर्पित /

ACKNOWLEDGMENTS

Lastly, I would like to thank my wife: Yashoda, sons: Shalin and Suprim, as well as, other family members and friends for being supportive during this entire venture. Without their support, I would not have been able to stay on track. I am eternally grateful to them.

TABLE OF CONTENTS

LIST OF FIGURES

LIST OF TABLES

LIST OF ABBRIBATIONS

μm	Micrometer	nm	Nanometer
μs	Microsecond	ns	Nanosecond
°C	Degree Celsius	NVM	Non-volatile Memory
3D	Three dimensional	O	Oxygen
Å	Angstrom	PDF	Powder diffraction file
A	Ampere	PLD	Pulsed Laser Deposition
AFM	Atomic force microscopy	PVD	Physical vapor deposition
BE	Binding energy	R	Resistance
EBL	Electron-beam lithography	R	Resistance
eV	Electron volt	RHEED	Reflection high energy electron diffraction
f	Frequency		
FFT	Fast-Fourier Transform	R_L	Load Resistor
f_{osc}	Frequency of oscillation	RRAM	Resistance Random Access Memory
FWHM	Full-width-at-half-maximum		
GIXRD	Grazing incidence x-ray diffraction	R_S	Sense Resistor
		s	Second
HT	High temperature	SEM	Scanning electron microscopy
I	Current	T	Temperature
IDE	Interdigitated electrode	T_{MIT}	Metal-to-insulator transition temperature
I-V	Current-voltage		
K	Kelvin	V	Voltage
kΩ	Kilo-Ohm	V	Voltage
LT	Low temperature	V_{in}	Input voltage
mA	Milliampere	V_{out}	Output voltage
MBE	Molecular beam epitaxy	XPS	X-ray photo-emission spectroscopy
MHz	Megahertz		
MIT	Metal-to-insulator transition	XRD	X-ray diffraction
Nb	Niobium	XRR	X-ray reflectivity
NbO_2	Niobium dioxide	Ω	Ohm

CHAPTER 1

INTRODUCTION

NbO$_2$ has attracted attention recently because of its metal-to-insulator transition (MIT) and its possible applications in electronic devices.[1-17] NbO$_2$ in bulk form transforms from an insulator to a metal at a transition temperature T_{MIT} = 1083 K, accompanied by a structural transition from a distorted rutile (low temperature) to a rutile (high temperature) structure, with increasing temperature.[16,17] Electric field induced reversible threshold resistance switching has been reported in NbO$_2$ thin film devices at room temperature caused by local joule heating which triggers the MIT.[1,2] The switching is volatile in nature in the sense that the current turns off immediately after lowering the input voltage (V_{in}) below the threshold value (V_{th}).

Current-voltage (*I-V*) characteristics usually exhibit current-controlled negative differential resistance (dV/dI < 0) while switching from a low current semiconducting to a high current metallic state.[1,16-20] Within the region of negative differential resistance, the current remains unstable and self-sustained current oscillations can be generated. The high MIT temperature of NbO$_2$ favors fast switching and high frequency current oscillations because the device can cool quickly below T_{MIT}.

Besides the temperature-induced structural change in stoichiometric NbO$_2$, other types of conduction mechanisms have been reported. Switching in amorphous NbO$_x$ film takes place via the formation of a crystalline conducting path after an electroforming current pulse is sent.[21] The

variation of the Nb oxidation state in NbO_x films have also been reported. For example, the insulating Nb_2O_5 phase can be reduced to metallic NbO and semiconducting NbO_2, the latter being the predominant phase. As a result, non-volatile resistive switching of the thin film element is possible.[3,4] Thus NbO_x thin films could be used for memory devices and electrical switching applications, while stoichiometric NbO_2 junctions are suitable as volatile threshold switching elements.[5-7,21-24]

1.1. BACKGROUND/MOTIVATION

In 1967, J. G. Simmons and R. R. Verderber published an article about reversible memory phenomena in thin insulating films.[25] Leon Chau, in 1971, postulated the new two-terminal circuit element as a 'Memristor – the missing circuit element'.[26] As defined by Chau, the memristor (memory + resister) is the fourth circuit element characterized by a relationship between the charge (q(t)) and the flux-linkage (ϕ(t)).[26] The resistance of a memristor depends on the history of the current that had previously flowed through the device and the direction of that current. Thus, a memristor have non-volatility property because it can memorize its past resistance state.

Resistive memories have been argued to bring the concept of memristor to life, first proposed by Chua,[26] as discussed above. Since then, bi-stable resistive switching of amorphous oxides,[27-32] chalcogenides,[33] amorphous Si[34] have been widely studied for non-volatile memory (NVM) applications.

In case of memristive materials, movement of ions or atoms takes place forming a conducting channel changing the conductivity of the material.[35] The process of changing conductivity is reversible and, hence applicable to future technology electronic devices. Because

of their resistance-reversible features, materials can be applied to memory devices for resistance random access memory (RRAM).

The proposed RRAM consists of the combination of two nonlinear elements: memory element and current switching element. Current switching element is added to prevent sneak path leakage current as discussed in Section 1.3, below. NbO_2, which is the material interest for this project, is a highly anticipated material for current switching element in a RRAM device.

1.2. MEMRISTIVE MATEIRLS AND RESISTIVE RANDOM ACCESS MEMORY (RRAM) DEVICES

Current Si-based technology is limited to feature sizes of 10 nm. Transistors smaller than 10 nm are likely to experience quantum tunneling through their logic gates, increasing the leakage current which eventually causes large power dissipation in the electronic device.[32,36] This means existing technology will soon reach this edge limit and thus violate Moore's law, which states doubling of device density in each 2 year. Resistive random access memory (RRAM) is one of the most promising technologies because of its simple architecture, fast operation, and low power consumption.[32] Because of RRAMs 3D architecture, device density can be increased by stacking structures along the vertical direction.

Some of the oxide thin films, such as NiO and Nb_2O_5, behave as a memristor. Under the influence of external field (flux-linkage), movement of O-atom or O-vacancy takes place changing the resistivity of the device. They nucleate near one of the electrodes forming conducting channel, called current filament, changing resistance state of the film as shown in Figure 1.1.[35] For oxide thin films, either excess oxygen atoms or oxygen vacancies can be the dominant charge carriers.
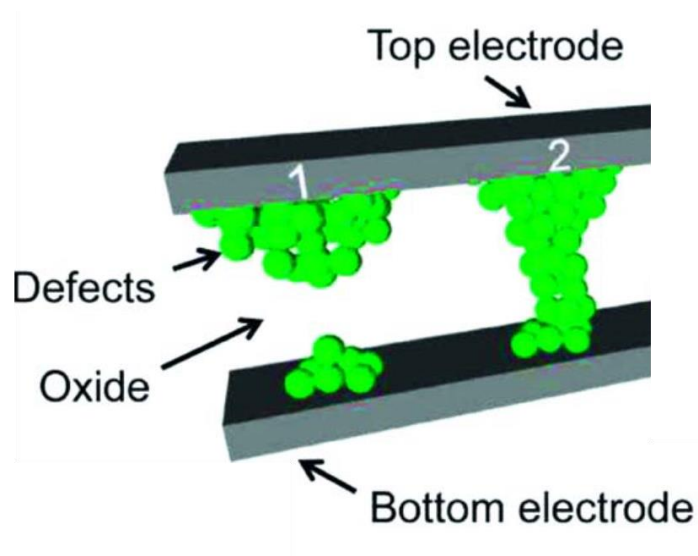
Figure 1.1: Schematic of the nucleation of defects (oxygen vacancies) and formation of filamentary pathways in a metal-oxide-metal sandwich device.[35]

The application of a positive input voltage, for example, results in negatively charged oxygen atoms being forced to move toward the positive electrode. An accumulation of large numbers of oxygen atoms near electrode ends up with a conducting channel between the electrodes, changing the film to a low resistance state. When input voltage is reversed, the oxygen atoms move away from the electrode, rupturing the conducting channel and switching the film back to its high resistance state. Because of their resistance-reversible features, these materials can be applied to memory devices for RRAM. Furthermore, because the resistance will not change even after the power source has been disconnected, RRAM is a nonvolatile memory device.

Figure 1.2 shows the structure of 3D-crossbar arrays proposed for a future RRAM device. Each of the memory units includes a bottom electrode, a top electrode and a robust nonlinear element in between.[32] The non-linear element might either be in the high resistance state, called
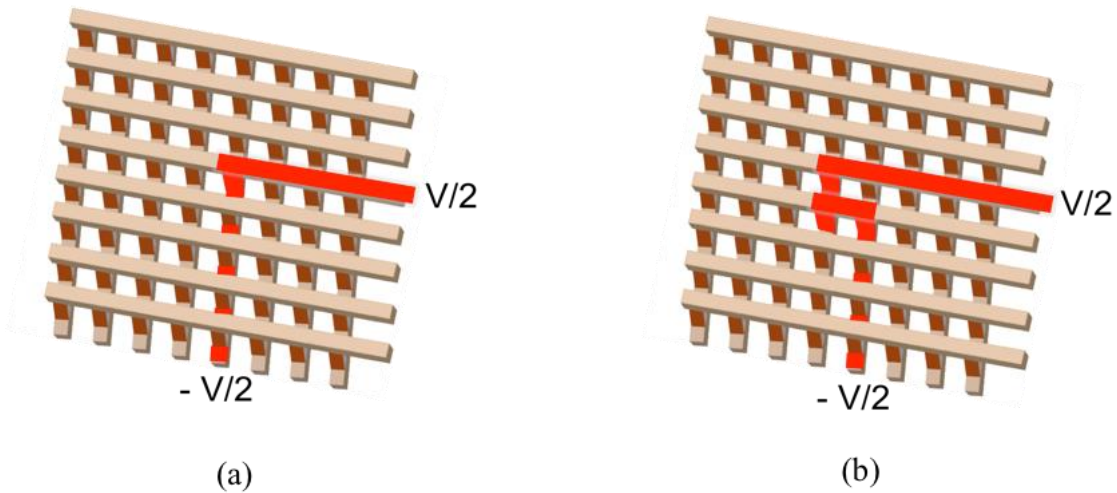
Figure 1.2: 3D-crossbar RRAM memory structure arrays. (a) Current path (red) when the device element is ON state. (b) Sneak current path when the targeted element at potential difference V is OFF state but some other elements at potential V/2 are at ON state.

OFF (or, 0) state or in the low resistance state, called ON (or, 1) state. A read voltage of $V/2$ and -$V/2$ applied to the top and bottom electrodes, respectively so that the targeted element experiences a potential difference of V and other elements remain at potential difference of $\pm V/2$. If the targeted element is in ON state, high current is detected along the path as indicated by red color in Figure 1.2(a). If the target element is in the OFF state, no current should be flowing through it.

1.3. NEED FOR A SELECTOR ELEMENT

A RRAM cell basically consists up of two metal cross bars connected by a memristor nonlinear element. In real crossbar arrays, however, multiple parallel conduction paths between

the pair of top and bottom electrodes, called sneak paths, add error to the current reading.[32] To prevent sneak path leakage current, a combination of threshold switching and resistive elements is essential.[32] In presence of threshold switching elements with threshold switching voltage (V_{th}) > ±$V/2$, all of the elements at potential difference of ±$V/2$ remain at off state preventing current flowing through them. In this project, I investigate possible application of NbO_2 thin films as a threshold switching element for a RRAM device.

1.4. WHY NIOBIUM DIOXIDE?

Several materials, such as perovskites $SmNiO_3$,[37] $SmCoO_3$,[38] $NdNiO_3$,[37] and transition metal oxides VO_2,[12] V_2O_3,[12] and NbO_2 [17] demonstrate metal-to-insulator transition characteristics. NbO_2 was selected for this project because of the following reasons:

1.4.1. Existence of Multiple Oxide Phases

Niobium has multiple oxide phases.[39,40] NbO is conducting with a superconducting transition at 1.4 °K[41,42] and is widely studied for memristive switching devices. NbO_2 is semiconducting with metal-to-insulator transition at 1083 K.[17] The band gap of NbO_2 has been measured to be between 0.6 and 1 eV. Nb_2O_5, on the other hand, is a high dielectric insulating material with band gap energy above 3 eV. Nb_2O_5 is being used for capacitors. In the presence of O_2, NbO and NbO_2 oxidize to their most stable phase Nb_2O_5 and it is possible to control thin film stoichiometry by changing oxygen concentration during growth.[43,44] Detail of these oxides will be discussed below in Section 1.5.

1.4.2. High MIT Temperature

NbO_2 has an insulator-to-metal transition at 1083 K with increasing temperature.[17] VO_2 is another similar material studied widely for current switching device applications. The metal-to-

insulator transition (MIT) temperature of VO_2 is close to room temperature (T_{MIT} = 340 K) which can easily be reached by heat dissipation while used in electronic devices. T_{MIT} of NbO_2, on the other hand, is very high so that MIT characteristics sustain in elevated temperature of electronic devices when used in practical application. The high T_{MIT} in NbO_2 is also advantageous for the generation of high frequency current oscillations because the film can cool down very quickly below T_{MIT}. Detail of these oxides will be discussed below in Section 1.5.

1.4.3. Sharp Electric Field Induced MIT

It is also possible to induce an MIT in NbO_2 by applying an electric field, where local joule heating produced by the applied electric field can induce the transition. Electric field induced sharp transitions from low current insulating to high current metallic state are observed with a change in resistivity above an order of magnitude.[20-22] Also, the switching time of 0.7 ns[2] is reported which is fast enough to use this material for electronic switching devices.

1.5. OXIDES OF NIOBIUM

1.5.1. NbO

Niobium monoxide (NbO) has a rock-salt type closed packed structure with space group $Pm3m$ and a lattice parameter $a = 4.21$ Å.[40] Face centered cubic sublattices of Nb and O atoms corresponding to (0,0,0) and (½, ½, ½) are unoccupied, creating vacancies as shown in Figure 1.3. NbO has metallic-type conductivity with a superconducting transition at 1.4 K.[45,46] NbO is the least stable of the Nb oxides and can easily be oxidized to NbO_2 or Nb_2O_5 when exposed to air.[40,43,44]

1.5.2. NbO₂

Niobium dioxide (NbO_2) is semiconducting in nature and undergoes an insulator-to-metal transition above 1083 K accompanied by a change in crystal structure[19,47-49] from a low
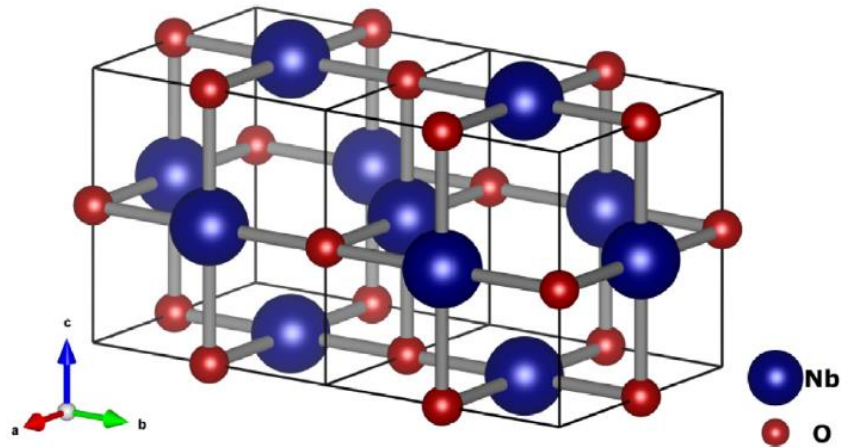
Figure 1.3: Crystal structure of niobium monoxide.[45] Nb atoms are represented by blue spheres and O atoms are represented by red spheres.

temperature distorted rutile to a high temperature rutile structure. Also, sharp electric field induced reversible threshold resistance switching is possible at room temperature which is volatile in nature.[5-7, 22-24] The detail of the crystal structure is discussed in Section 1.6.

1.5.3. Nb₂O₅

Niobium pentoxide is the most thermodynamically stable oxide of niobium in atmospheric conditions.[50-52] Nb_2O_5 exists in several polymorphic forms.[45-50] Brauer[51] described T, M and H - Nb_2O_5 forms, or the Nb_2O_5 - γ, β and α forms, which are successively formed after crystallization of amorphous films. The different niobium pentoxides are built on a volumetric arrangement of NbO_6 coordinated octahedra which allows changes in stoichiometry to be accommodated (Figure 1.4).[52,53] Schäfer described these phase as TT, T- and B-Nb_2O_5 phases[50] which could be successively or simultaneously formed after post-oxidation of ordered NbO_2 at the substrate
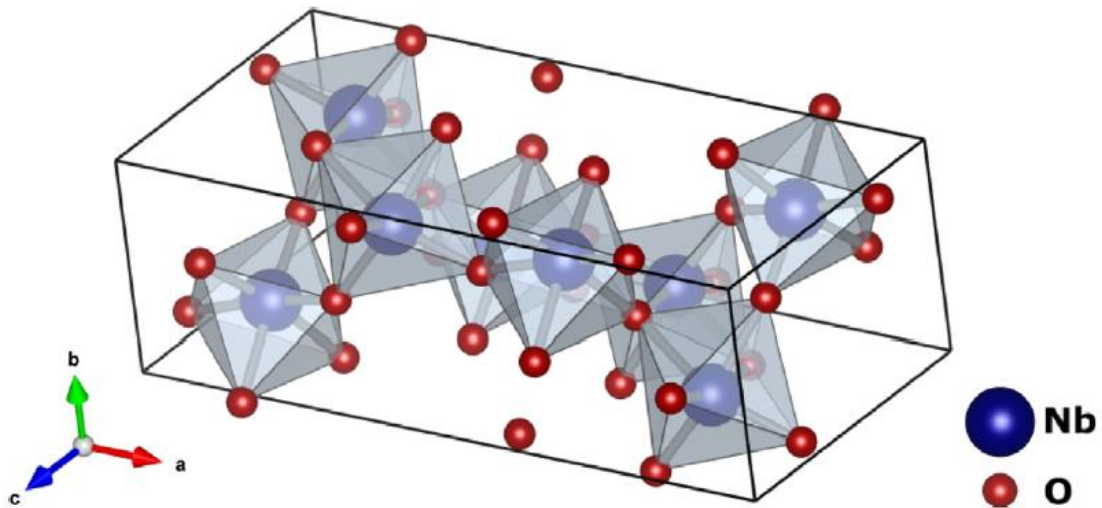
Figure 1.4: Crystal structure of monoclinic B-Nb_2O_5 adopted from Ref. 45. Nb atoms are represented by blue spheres and O-atoms are represented by red spheres.

temperature 650 °C, with the corresponding unit cells of a = 3.607 Å and c = 3.925Å (pseudo-hexagonal,[52] a = 6.168 Å, b = 29.312 Å, c = 3.936Å (orthorhombic L-phase[53]), and a = 12.744 Å, b = 4.885Å, c = 5.563Å, β = 105.03° (monoclinic[53]). The monoclinic phase crystal structure is shown in Figure 1.4. The crystalline monoclinic γ phase (a = 7.31Å, b = 15.72Å, c = 10.75Å and β = 120.42°) appears just after heating at about 500 °C. After 1000 °C the second modification to the β form is produced. Heating above 1100 °C gives rise to the α form which is irreversible. The α form is also monoclinic with a = 21.34 Å, b = 3.816 Å, c = 19.47 Å and β = 120.20°.

1.6. NIOBIUM DIOXIDE CRYSTAL STRUCUTRE

Room temperature NbO_2 has a tetragonal unit cell (space group $I4_1/a$), with lattice parameters $a_T = b_T = 13.702$ Å and $c_T = 5.985$ Å.[16,40] The atomic positions are listed in Table 1. The high temperature phase has a rutile cell structure (space group $P4_2/mnm$, similar to TiO_2) with lattice parameters of a = b = 4.846 Å and C = 3.032 Å.[16] With lowering temperature, the high T rutile phase gets distorted. It is assumed that the distance between Nb-atoms along c-axis alternatively becomes shorter (2.71 Å) and longer (3.30 Å). Schematics of the NbO_2 high temperature (HT) and low temperature (LT) phases are shown in Figure 1.5.

The axis transformation between low temperature tetragonal (T) phase to high temperature rutile phase (R) is described as[16]

$$\vec{a}_T = 2\,(\vec{a}_R - \vec{b}_R), \tag{1}$$

$$\vec{b}_T = 2\,(\vec{a}_R + \vec{b}_R) \tag{2}$$

and,

$$\vec{c}_T = 2\,\vec{c}_R \tag{3}$$

The transition is made possible by the so-called Peierls or Mott-Peierls distortion discussed in section 1.7.[54-56] The low temperature phase also has a tetragonal structure with a rotational transformation in lattice vectors with $P4_2/mnm$ crystal symmetry.
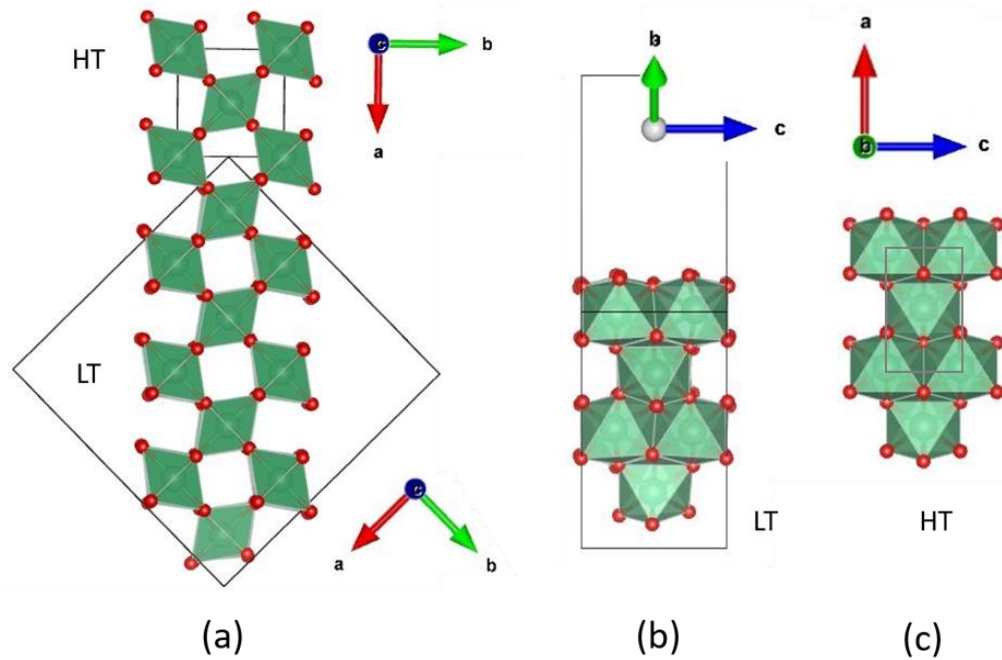
Figure 1.5: NbO$_2$ crystal structures. (a) Top views of the high temperature (HT) rutile (100) NbO$_2$ and low temperature (LT) tetragonal (110) NbO$_2$. Corresponding lattice axes are shown to the right. (b), (c) Side views of the low temperature (LT) tetragonal phase and high temperature (HT) rutile phase, respectively. O-atoms are represented by the red dots.

Table 1: Atomic position of NbO$_2$ tetragonal phase[40]

Atom	X	Y	Z
Nb(1)	0.116	0.123	0.488
Nb(2)	0.133	0.124	0.031
O(1)	0.987	0.133	-0.005
O(2)	0.976	0.126	0.485
O(3)	0.274	0.119	0.987
O(4)	0.265	0.126	0.509

1.7. METAL-TO-INSULATOR TRANSITION (MIT) MECHANISM

1.7.1. *Mott Insulator*

Under conventional band theories, materials with partially filled orbitals are conductors in which electrons can move independently in an effective periodic potential. For many transition metal oxides, however, conventional band theory fails. These oxides are insulators despite of their partially filled 3d, 4d or 4f orbitals due to the strong Coulomb interaction between electrons. These class of materials are called Mott insulators.[57] In Mott insulators, the electron-electron interaction Coulomb repulsion energy (U) is stronger than electron hopping energy (t) which prevents electrons to move through the lattice. This interplay between these two energies can be described by the Hubbard model Hamiltonian, which can be written as[54,57]

$$\mathcal{H}_H = \mathcal{H}_t + \mathcal{H}_U - \mu N, \tag{4}$$

with

$$\mathcal{H}_t = -t \sum_{<i,j>\sigma} \left(\hat{c}_{i\sigma}^\dagger \hat{c}_{j\sigma} + \hat{c}_{j\sigma}^\dagger \hat{c}_{i\sigma} \right), \tag{5}$$

$$\mathcal{H}_U = U \sum_i \hat{n}_{i\uparrow} \hat{n}_{i\downarrow}, \tag{6}$$

and

$$N = \sum_{i\sigma} \hat{n}_{i\sigma} = \sum_{i\sigma} \hat{c}_{i\sigma}^\dagger \hat{c}_{i\sigma}. \tag{7}$$

$\mathcal{H}_t$ represents the nearest-neighbor hopping Hamiltonian, which is related to the kinetic energy of the electron, where $\hat{c}_{i\sigma}^\dagger$ and $\hat{c}_{i\sigma}$ are the creation and annihilation operators for an electron at site i with spin σ. $\mathcal{H}_U$ represents the onsite Coulomb interaction and $\hat{n}_{i\sigma}$ in Eq. 7 is the number operator.

In the presence of a strong electron-electron interaction ($U \gg t$), the d-band splits into two sub-bands called upper and lower Hubbard bands, opening an energy gap as shown in Figure 1.6.
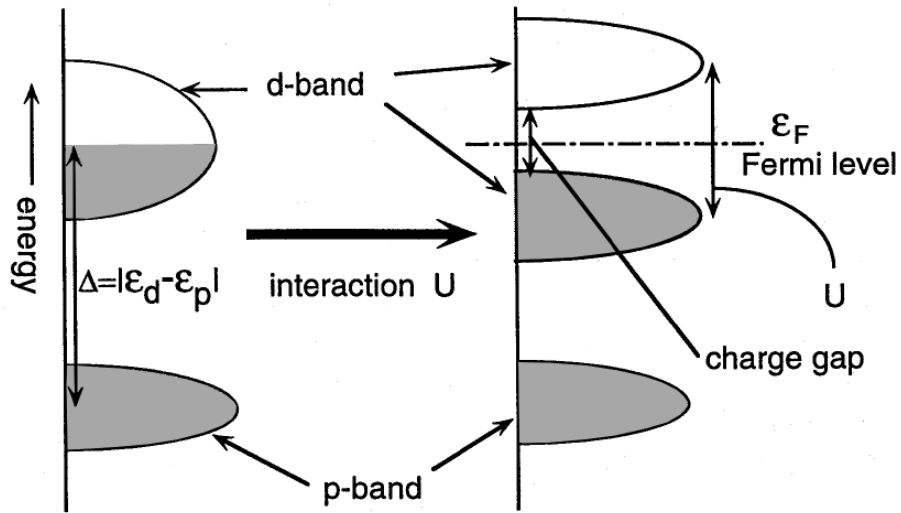
Figure 1.6: Schematic of energy levels for Mott-Hubbard insulators in absence (left) and in presence (right) of electron-electron interaction energy U.[36]

This energy gap hinders electrons from delocalizing and the material therefore behaves like an insulator if the temperature is low enough.

Insulator-to-metal or metal-to-insulator transitions basically arise from the competition between U and t. U and t can be tuned by modifying in the band structure by applying an external perturbation, for example, via strain, electric field, or temperature change. Possible techniques, including lattice modification using strain or electron or hole doping are illustrated in Figure 1.7.

1.7.2. *Peierls Instability and Insulator-to-Metal Transition*

In 1955, Peierls showed that an evenly distributed 1-dimensional atomic chain is unstable.[58] The system is stabilized by forming atomic dimers where the distance between adjacent atoms becomes shorter and longer to minimize electronic energy.[54-56] This dimerization is called
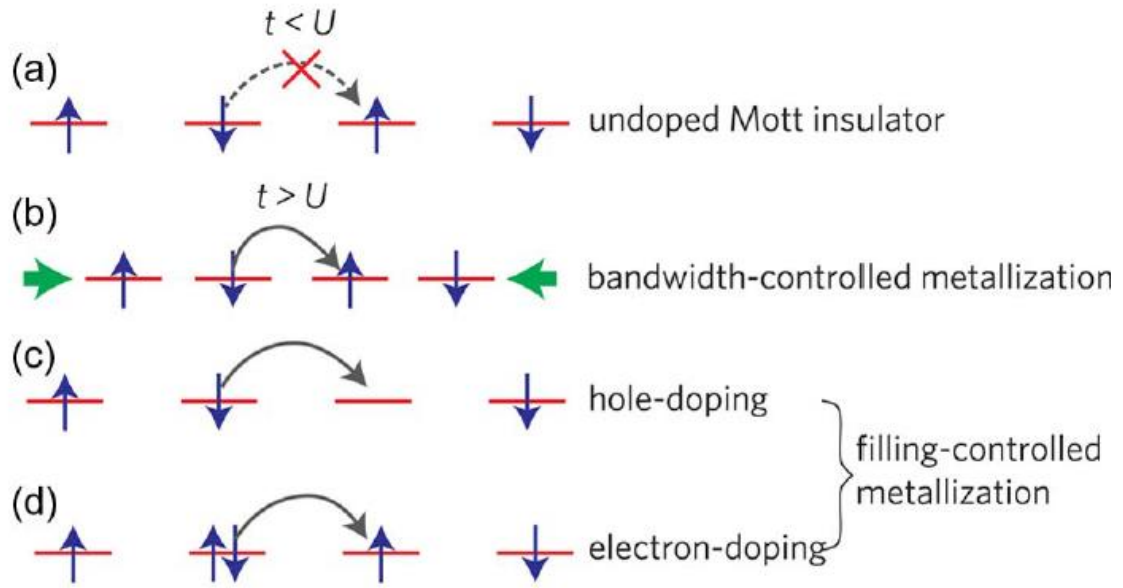
Figure 1.7: Insulator-to-metal transition in Mott insulators. (a) Electron arrangement in Mott insulator. (b) Metallization via. bandwidth control (lattice modification). (b), (c) Metallization via. filling control [hole (c) and electron (d) doping][36]

Peierls transition. As the result of Peierls transition, many of the materials become insulators upon cooling.

The insulating phase in NbO_2 is believed to be stabilized by a Peierls transition. Metal-to-insulator transitions, however, are not just due to a Peierls transition; they are described by a combined Mott + Peierls transition. Because Nb is a $4d$ transition metal, electron correlations responsible for the Mott-insulator behavior in NbO_2 should play a weaker role than it does in VO_2, V being a $3d$ transition metal.[10,59] Therefore, the Peierls transition is relatively stronger in NbO_2. The higher dispersion of the $4d$ valance Nb bands is responsible for the higher T_{MIT} because of the larger Nb-Nb extension of $4d$ orbitals, which also results in a greater energy splitting between
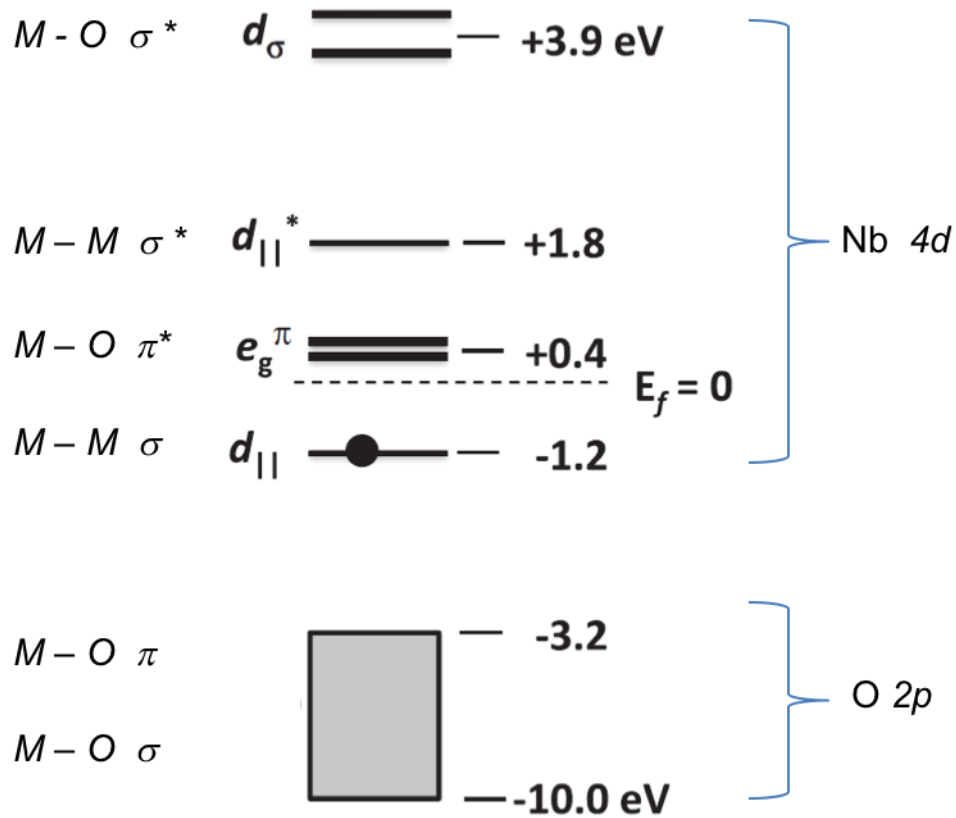
Figure 1.8: An estimation of energy arrangement of electron levels of insulating NbO_2.[10,54,60] At metallic state, energy bands $d_{\parallel}$ and e_g^{π} overlap at the Fermi energy.

occupied $d_{\parallel}$ states and unoccupied e_g^{π} states as discussed in Ref. 10. Figure 1.8 shows the energy ordering of the different bands with respect to the Fermi level in NbO_2.[10,60]

In the metallic state, $d_{\parallel}$ and e_g^{π} states overlap at Fermi level. During dimerization, $d_{\parallel}$ band splits into bonding $d_{\parallel}$ and antibonding $d_{\parallel}^*$ states. Tilting of the dimer, on the other hand, provides instability to the e_g^{π} band, resulting an uplift of the band above the Fermi energy, E_f.[59,60] Wong et

al. have estimated the energy splitting between $d_{\parallel}$ and e_g^{π} to be larger by 0.3 eV in NbO_2 than the energy splitting in VO_2, which makes T_{MIT} in NbO_2 much higher than VO_2.[10]

1.8. METAL-TO-INSULATOR TRANSITION (MIT) IN NIOBIUM DIOXIDE

The MIT in bulk NbO_2 is experimentally observed with a conductivity change of over an order in magnitude at 1083 K, as demonstrated in Ref. 17 [Figure 1.9(a)]. Additionally, electric-field-induced MIT in NbO_2 thin films is also reported in the literature where an applied electric field in the order of 10^6 V/m leads this material to MIT [Figure 1.9(c)].[5-7,22-24] The exact mechanism of electric-field-induced MIT in NbO_2, however, is under debate.

1.8.1. Electric Field Induced Transition

Electric field induced transitions have been widely studied in VO_2 because of its lower T_{MIT} (~ 340 K), which provides convenience in the temperature-dependent measurements near room temperature. Several authors assume that the low temperature tetragonal phase is a Mott insulator and that the insulator-to-metal transition takes place before the structural transition.[59,64-68] Rice et al. in 1994[61] suggested that the M2 phase (in which only one-half of the V atoms in chain twist without pairing during rutile to monoclinic phase transition but other half of the atoms pairs without a twist) of VO_2 has Mott transition. Stefanovich et al.[66] in 2000 claimed that the MIT in VO_2 is triggered by a Mott transition followed by a Peierls-like structural transition. Temperature dependent Raman spectroscopy measurements performed by Kim et al.[67] in 2005 agreed with Stefanovich's point of view. Kim et al.[68] confirmed the separation between insulator-to-metal transition and structural phase transition using microscopic x-ray diffraction measurement.
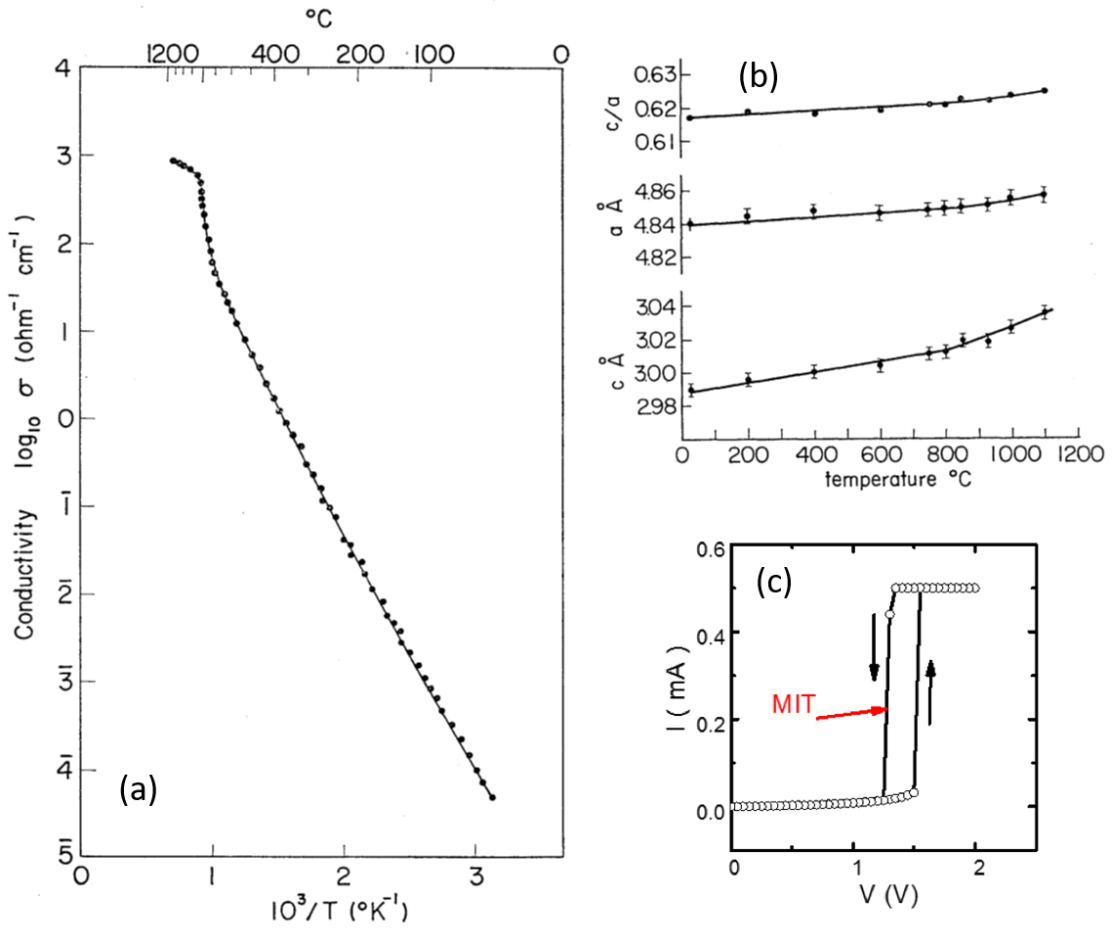
Figure 1.9: (a) Temperature dependent MIT by Sakai et al.[17] An increase in conductivity across MIT of an order magnitude was observed. (b) Change in lattice parameter with temperature.[63] (c) Electric field induced insulator-to-metal transition in NbO$_2$ film.

1.8.2. *Joule Heat Induced Transition*

Besides the electric field induced metal-to-insulator transitions, there are several reports supporting Joule heat-induced structural change during MIT in VO$_2$.[59,62,64,69-71] Lee et al. mapped local temperature increase during MIT in VO$_2$ using IR reflectance.[69] Zimmers et al.[71] also

demonstrated local joule heating induced insulator-to-metal transition in VO_2 using fluorescence spectra assisted direct temperature measurement technique.

1.8.3. MIT in NbO₂: Peierls or Mott?

The switching mechanism in NbO_2 has not been extensively studied. Jannick et al, in 1965, observed temperature-dependent conductivity change above 1073 K indicating thermally induced insulator-to-metal transition in NbO_2.[72] Sakata et al, in 1969, published conductivity change [Figure 1.9(a)][17], as well as the change in lattice parameters above 1070 K [Figure 1.9(b)][63] demonstrating that the conductivity change is associated with the structural change.

Most of the researchers agree that low temperature insulating phase of NbO_2 has a distorted rutile structure stabilized by the Peierls instability.[9,54,56] Only a few reports, however, have been published on the electric field induced switching model. Slesazeck et al. recently published a switching model claiming that the insulator-to-metal transition occurs at 550 K in NbO_2 thin films as a result of local Joule heating and a Frenkel-Poole conduction mechanism.[73] However, the latter work was based on disordered NbO_x/Nb_2O_5 thin films, and the effect of disorder was not assessed since films with proper stoichiometry were not measured.

1.8.4. Redox Based Switching

Chudnovskii et al. has reported redox-base switching in several transition metal binary oxides including NbO_2.[21] A phase change phenomenon in NbO_2 is obtained via oxidation and/or reduction processes. Dissociation of an oxygen atom from NbO_2 yields a conducting NbO while combination with an oxygen atom results the insulating Nb_2O_5 phase. Excess Nb atoms, if present in the film, combine with NbO_2 or Nb_2O_5 to reduce the valency of Nb yielding NbO or NbO_2. Variations of the Nb oxidation state in polycrystalline NbO_x films take place after an electroforming current pulse is sent.[12] Nonstoichiometric NbO_x thin films, therefore, can be used

for memory switching applications while stoichiometric NbO_2 junctions are suitable as volatile threshold switching elements.[5-7,22-24]

Similar to the VO_2, the transition mechanism in NbO_2 is also under debate, as discussed above. An in-depth study is essential to understand the exact switching mechanism in NbO_2. Since both materials have similar type of crystal structure, they are expected to have similar type of transition mechanism. NbO_2, however, has $4d$ electron system and must have a stronger Peierls type distortion as predicted by several researchers.[9,56] In this project, experimental studies of NbO_2 thin film switching mechanism using various types of films is presented.

1.9. PROJECT OUTLINE

In this project, study of NbO_2 films grown on the variety of substrates with film quality varying from polycrystalline to epitaxial structures are presented. The prior works as described above is based on NbO_2 that is usually not stoichiometric, whereas here I investigate films with the best possible stoichiometry and crystallinity in order to determine the role of defects. In doing so, I hope to understand the intrinsic electronic behavior of NbO_2 thin films and to determine the role of defects. Specifically, I investigate NbO_2 epitaxial thin film devices grown on Al_2O_3 and doped GaN coated Al_2O_3 substrates, and polycrystalline thin film devices grown on TiN coated SiO_2/Si substrate. Current is measured along the lateral direction using inter-digitated electrode (IDE) structures in epitaxial devices grown on Al_2O_3 while current is measured along the vertical direction in the devices grown on Si-doped GaN substrate using GaN layer as a bottom contact. Similarly, current is measured along the vertical direction in the case of polycrystalline film device grown on TiN coated substrate where conducting TiN layers are used as bottom contacts. I compare the switching mechanism between epitaxial and polycrystalline thin film vertical devices,

for the first time, using films grown on doped GaN (epitaxial) and TiN (polycrystalline). The following is the outline of this dissertation:

In CHAPTER 2, experimental techniques will be discussed including pulsed laser deposition (PLD) growth technique and structural characterization techniques such as x-ray diffraction (XRD), x-ray reflectivity (XRR), x-ray photo-emission spectroscopy (XPS) and atomic force microscopy (AFM), as well as, electrical characterization techniques.

CHAPTER 3 includes a description of pulsed laser deposition (PLD) growth and structural characterization of NbO_2 epitaxial thin films on Al_2O_3 and doped GaN substrates, and polycrystalline thin films on TiN/Si substrates, all using PLD. Structural characterization techniques include XRD, XRR, AFM, and XPS. Optical band gap measurement technique will also be discussed in this chapter. General θ-2θ XRD, however, is not very effective in case of polycrystalline films because the intensity of the Bragg peaks remains suppressed in comparison to the substrate peaks. Therefore, grazing incidence x-ray diffraction (GIXRD) was used to investigate polycrystalline films.

The electrical characterization of NbO_2 epitaxial thin film *lateral* devices will be discussed in CHAPTER 4. The current-voltage characteristics of the lateral devices made up of epitaxial thin films grown on Al_2O_3 substrates were investigated using inter-digited electrode (IDE) structures as two terminal devices. The thermally-induced nature of insulator-to-metal transition in NbO_2 was demonstrated using pulsed-width dependent *I-V* measurements and current vs temperature measurements. The electrical characterization of polycrystalline thin film *vertical* devices grown on TiN-coated SiO_2 substrate will also be described in CHAPTER 4. An epitaxial film grown on Si-doped GaN on Al_2O_3 substrates will be used to compare epitaxial films with polycrystalline films. The bottom conducting Si doped GaN layer works as the bottom contact similar to the TiN

layer in the case of polycrystalline film device. The role of thickness and contact size on current voltage measurements will be discussed, and the switching characteristics of the two types of samples (epitaxial and polycrystalline) with different defect densities will be compared. Self-sustained current oscillation generated by NbO_2 polycrystalline and epitaxial vertical devices will also be discussed, and oscillatory behavior of thin films grown in different growth conditions will be compared.

Finally, overall conclusions of this project work will be presented in CHAPTER 5.

CHAPTER 2

EXPERIMENTAL TECHNIQUES

In this chapter, experimental methods for thin film growth and their structural and electric characterization techniques will be discussed. Pulsed laser deposition (PLD) was used to grow epitaxial and polycrystalline films. The structural characterization was performed using reflection high energy electron diffraction (RHEED), x-ray diffraction (XRD) (both out-of-plane and in-plane), and x-ray reflectivity (XRR). The chemical valency state was determined using x-ray photoelectron spectroscopy (XPS). Atomic force microscopy (AFM) was used for surface topography and conductive probe AFM was used to measure contact size dependent current-voltage (*I-V*) characteristics. For lateral devices, current-voltage (*I-V*) measurements were performed using two-point contacts in vacuum to avoid possibility of oxidation of the film by atmospheric oxygen. In the case of vertical devices, *I-V* characteristics was measured using a probe-station tip in atmospheric pressure.

2.1. SUBSTRATE PREPARATION

Prior to loading into the deposition chamber, the substrates were cleaned to remove dust particles in an ultrasonic bath using acetone and methanol for 15 and 10 minutes, respectively. The substrates were dried by blowing with high purity nitrogen over the surface. The substrates were mounted on the substrate heater using clipped substrate holder or glued using a fast drying silver

paste to provide a good thermal contact. An additional step was performed in case of sapphire (Al_2O_3) substrates. After cleaning in acetone and methanol, the substrates were annealed at 1200 °C for 2 hours in air in a high temperature furnace in a pure alumina tube. The temperature ramping and cooling rate used was about 300 °C/hr. Atomic terraces due to surface reconstruction on the surface of Al_2O_3 was verified using AFM surface scans. The details of Al_2O_3 substrate preparation techniques can be found elsewhere.[74]

2.2. PULSED LASER DEPOSITION (PLD)

All thin films reported in this dissertation were deposited using pulsed laser deposition (PLD). PLD is a versatile thin film deposition technique based on physical vapor deposition (PVD)[75] and the process characteristics are similar to molecular beam epitaxy (MBE) and sputter deposition. The process is carried out in a vacuum system with base pressure below 10^{-9} Torr. A high power pulsed laser beam is focused to strike a solid target of the desired material. Using a laser pulse with sufficiently high energy, the material from the target is vaporized forming a highly energetic plasma plume. The plume of the ejected material is directed normal to the target surface providing material flux for the growth.[76,77]

PLD has proven remarkably effective at inorganic thin film deposition because of its attractive features, such as stoichiometric transfer the of target material, generation of energetic plasma, hyperthermal reaction between ablated atomic cations within the plasma. Additional interaction with background gas helps to maintain desired thin film stoichiometry. The system has compatibility with background pressure ranging from ultrahigh vacuum to several Torr. Most importantly, compound films can be deposited with PLD using a single stoichiometric target of the
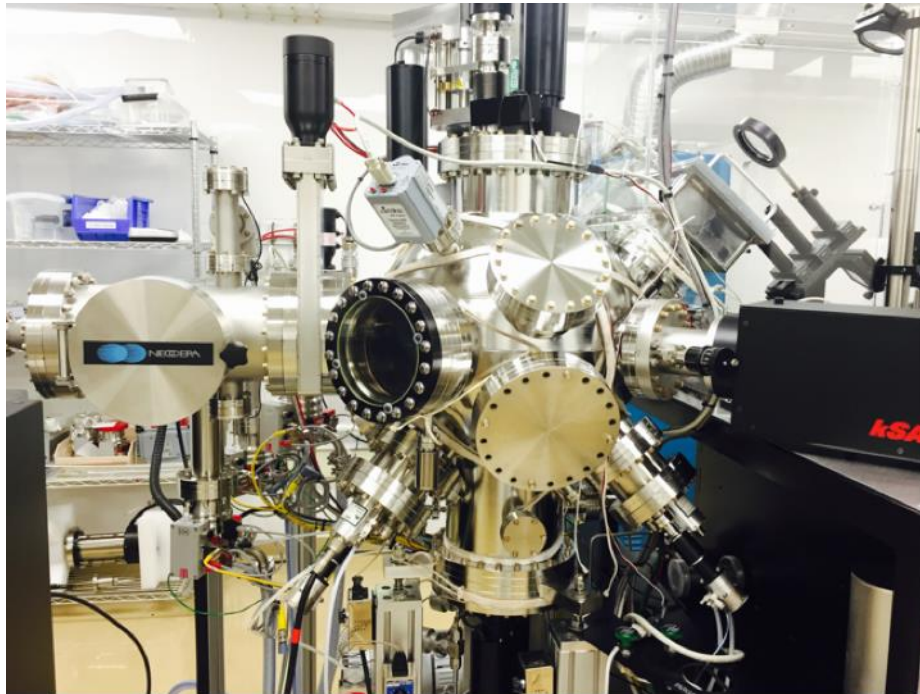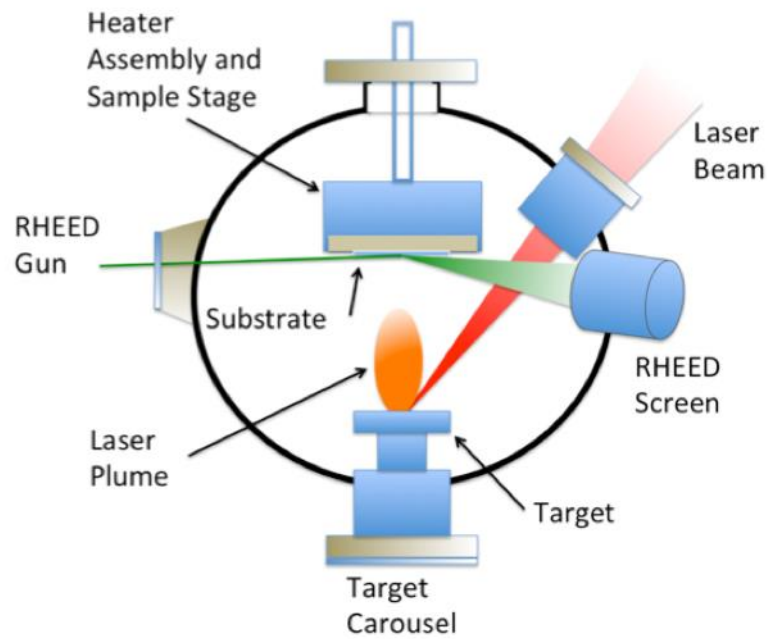
Figure 2.1: Laser deposition setup for a Pulsed Laser Deposition (PLD) system. (a) photograph of PLD chamber at WVU, and (b) schematic diagram showing thin film deposition using PLD.

material of interest. At the same time, the range of substrate temperature can be chosen from room temperature to 1050 °C.

The PLD system consists of three main components: the vacuum chamber, the laser unit and laser optics. The vacuum chamber has two parts: main chamber and load-lock chamber. Two of the chambers are separated by a gate valve so that the main chamber always remains in vacuum. The laser optics are used to redirect the laser pulses produced by laser unit toward the chamber and focus them to the target surface. The schematic diagram of the PLD chamber is shown in Figure 2.1.

The rotation/rastering of the target provides uniform wear of the target surface. Targets can be switched during growth so that the growth of multilayer, heterostructures or alloy samples is possible. Also, the growth of a wedge-shaped sample with varying thickness is possible using gradual deposition servo shutter.

The physical phenomena of laser-target interaction and film growth are quite complex and measurement of various state variables of the plasma, such as, temperature and density as well as ionization state and behavior of the various species in the plasma is not trivial. When the laser pulse is absorbed by the target, energy is first converted to electronic excitation and then into thermal, chemical and mechanical energy resulting in evaporation, ablation and plasma formation. The deposition process is generally divided into following three sub-processes as described below.[75]

2.2.1. Laser Ablation (Laser Matter Interaction)

During ablation, a particle's expulsion takes place in the periods of time between nano to microseconds when a laser pulse hits the target. The target material absorbs the laser light and emits electrons. The emitted electrons transfer some of their energy to the lattice. The surface material now gets hot and is evaporated. The penetration depth depends on the target material, typically, the optical absorption depth and the thermal diffusion length. In dielectric materials, optical absorption depth

becomes dominant over thermal diffusion length. In case of metal, on the other hand, thermal diffusion length dominates over optical absorption depth.

The thermal diffusion length is defined by the equation[76]

$$\lambda = 2\sqrt{\alpha t}, \tag{8}$$

where t is the time duration of the pulse. The thermal diffusivity term, α, is given by the relation $\alpha = \frac{K_T}{\rho_m c_g}$, where, K_T is the thermal conductivity, ρ_m is the density and c_g is the heat capacity per gram of the target material.

2.2.2. Plume Propagation

The material expelled from the target material expands towards the normal vector of the target surface and is directed toward the substrate placed in front of the target as shown in Figure 2.2. A plume contains atoms, particles or even the droplets of materials ejected from the target surface. Inside the plume, interaction between the particles as well as between ambient gas molecules takes place. The shape of the plume depends on the background pressure inside the PLD chamber. Highly energetic particles reaching the substrate and the particles emitted from the target form a collision region where condensation of particles take place.

2.2.3. Deposition (Interaction of the Plume with Substrate Material)

Finally, the nucleation of the ablated material on the substrate takes place. Nucleation and growth kinetics of the film depend on laser parameters, such as laser energy density, pulse repetition rate, and the deposition flux. Also, nucleation density is largely effected by surface temperature, surface roughness, and lattice mismatch between the substrate and the prospective material to be grown. Increasing substrate temperature yields a decreased nucleation density.
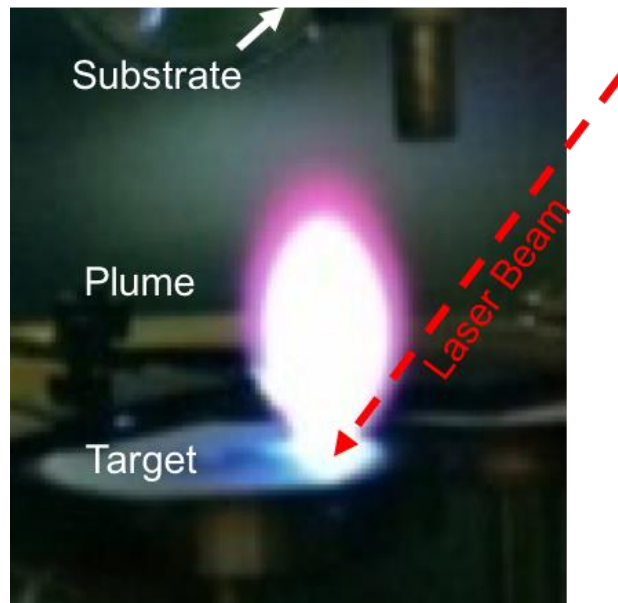
Figure 2.2: Inside view of a PLD chamber with a laser plume generated after a laser pulse hits the target surface. The red arrow shows the direction of the incident laser beam.

An oxygen background is needed during oxide thin film deposition to ensure stoichiometric transfer from the target to the film. Thin film growth rate in PLD depends on multiple factors, such as, target-substrate distance, background gas pressure, laser spot size and laser energy density.

PLD is most effective technique for crystalline and polycrystalline oxide thin film growth. Desired oxide phase formation requires the delivery of a growth flux with the correct oxidizing ambient. By controlling oxygen pressure with substrate temperature and laser energy, the synthesis of complex oxides thin films with desired stoichiometry becomes possible.

A PLD system manufactured by Neocera with a KrF excimer laser (248 nm) from Coherent, Inc. was used to grow all films used in this work. The fully automated Neocera PLD system contains

in-situ RHEED monitoring system. The base pressure in the main chamber remains below 10^{-8} Torr. The system has two separate mass flow controllers for Ar and O_2 with maximum mass flow capacity of 50 and 200 sccm, respectively. The turbo pump speed can be varied from 164 Hz to 820 Hz. The system can hold three 2" diameter targets or six 1" targets.

2.3. TARGET PREPARATION

The Nb_2O_5 target was prepared from 99.99% purity of corresponding powders purchased from Sigma-Aldrich. The powder was pressed into a pellet and sintered for 72 hours in air at 1300 °C. A NbO_2 target with purity level above 99.99% was purchased from Sigma-Aldrich later to replace the Nb_2O_5 target, which seemed to yield better results, in terms of improved stoichiometry.

The target needs to be polished after being used for a long time to remove surface defects or damage produced by thermal shock. Also, irregular ware produces high roughness or curvature on the surface. Unusual changes in the growth rate or a change in plume shape while rastering target from center to the edges or any other visible irregularities on the surface of the target indicate that the target needs to be polished.

To polish the target, a circular foil of sandpaper 6" to 10" in diameter was used. The sandpaper is placed on the flat surface in fume hood and the target is manually polished at the center of the foil. The surface to be polished must be placed downward, in contact with the sandpaper surface. The target is pressed uniformly using four fingers and rubbed in a figure-eight until the surface becomes visibly smooth. Sandpaper from Deerfos America (CC261) with grit 240 was used to polish the target during this project.

2.4. REFLECTION HIGH ENERGY ELECTRON DIFFRACTION (RHEED)

The surface quality of the substrates and crystalline quality of the films was monitored during the entire interval of growth using an *in-situ* reflection high-energy electron diffraction (RHEED) system from STAIB Instruments. RHEED is a powerful technique for real-time *in-situ* monitoring of the crystal properties of the surface during growth.[78] The system consists of a fluorescent screen, an electron source (energy range from 500 eV to 30 keV, beam current up to 1.55 mA), and a power supply with beam blanking and deflection control for focusing and positioning of the electron beam. The schematic diagram the RHEED apparatus is shown in Figure 2.3(a).

Electrons in an electron beam are accelerated by high voltages (about 20 to 30 kV) which hits the film surface with a small angle relative to the surface plane forming RHEED patterns on the florescent screen as shown in Figure 2.3(a). The small angle ensures small penetration into the film making RHEED sensitive to the surface geometry. The diffraction of electron beam leads to a change in electron momentum providing a set of diffraction pattern on either side of the specularly reflected beam. If the incident electron beam is parallel to the rows of surface atoms that are separated by the lattice vector d_S in the direction perpendicular to the beam direction, then the diffracted electron beams contribute to constructive interference. The angle of diffracted electrons relative to the incident direction, fulfills the well-known Bragg diffraction formula[80,81]

$$2d_S \sin \theta = n\lambda_E \tag{9}$$

where n is an integer and λ_E is the de Broglie wavelength of the electrons. Using energy and momentum relations $\frac{1}{2}mv^2 = eV$ and $mv = h/\lambda_E$, where v and V are velocity of the electron and accelerating potential difference, respectively, the de Broglie wavelength is given by
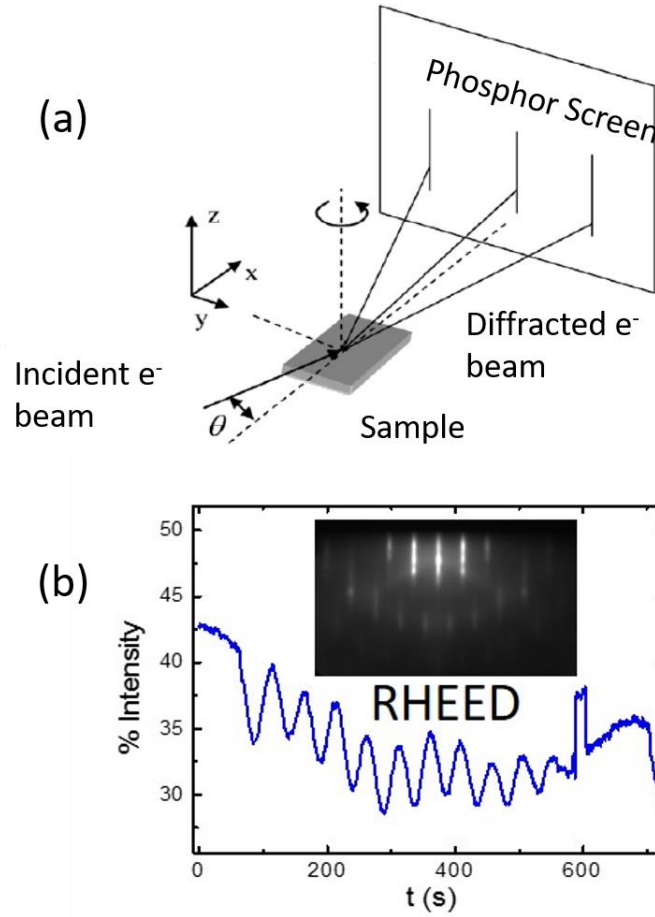
Figure 2.3: Reflection high energy electron diffraction (RHEED). (a) Schematics of RHEED geometry.[79] (b) A representative RHEED image (inset) and intensity of oscillations obtained during the growth of 3 nm Cr_2O_3 film using PLD.

$$\lambda_E = \sqrt{\frac{mh^2}{2eV}}.$$
(10)

Therefore, the de Broglie wavelength for an accelerating voltage range of 20 to 30 kV will be in the range of 0.09 to 0.07 Å.

Qualitative information of the crystal roughness can be obtained from the diffraction pattern. Using RHEED, it is possible to distinguish if the film surface is smooth or rough or even if the growth is 3-dimentional (island like). Streaky RHEED patterns usually result from crystalline films smoothly grown on the substrate while RHEED patterns with transmission spots (spots that have the symmetry of the bulk crystal) indicate crystalline but rough film surfaces or island-like growth. Polycrystalline films have circular RHEED patterns (similar to an x-ray diffraction Laue pattern from a polycrystalline sample) while no RHEED pattern indicates that the film is amorphous.

Lattice parameters can be measured *in-situ* using RHEED diffraction pattern. For the case of layer-by-layer deposition, where a monolayer grows at a time, the growth rate can be calibrated using RHEED intensity of oscillations.[82] During the sub-monolayer surface coverage, the RHEED intensity decreases while the intensity becomes high after completion of a unit cell.[82,83] These fluctuations in RHEED intensity provide a time dependent oscillation pattern in the intensity plot during growth. Figure 2.3(b) shows an example of RHEED pattern and intensity of oscillations measured during growth of 3 nm Cr_2O_3 film grown using the same PLD system used for the growth of the samples in this project.

2.5. X-RAY DIFFRACTION (XRD) AND X-RAY REFLECTIVITY (XRR)

2.5.1. *Out-of-Plane (θ-2θ) and In-Plane (ϕ) X-ray Diffraction Scans*

X-ray diffraction is widely used for structural characterization of crystals. The technique was discovered by Bragg in the 20th century.[84] The wavelength of the x-rays from a copper target, for example, is comparable to the distance between atomic or molecular structures. This makes x-ray diffraction ideally suited for crystallographic characterization of materials.[84-87]
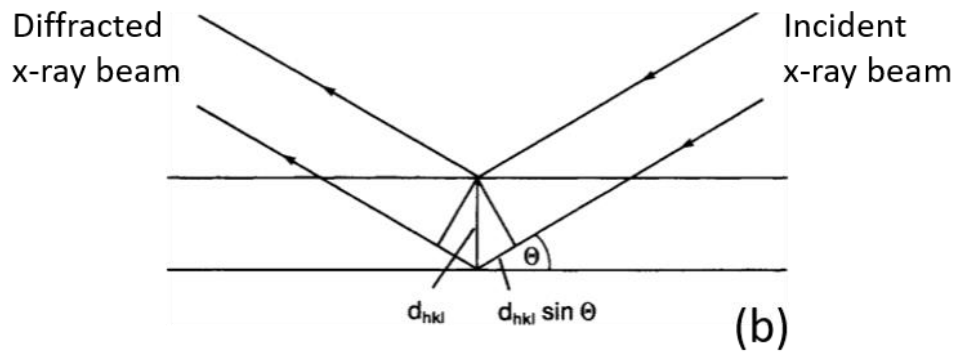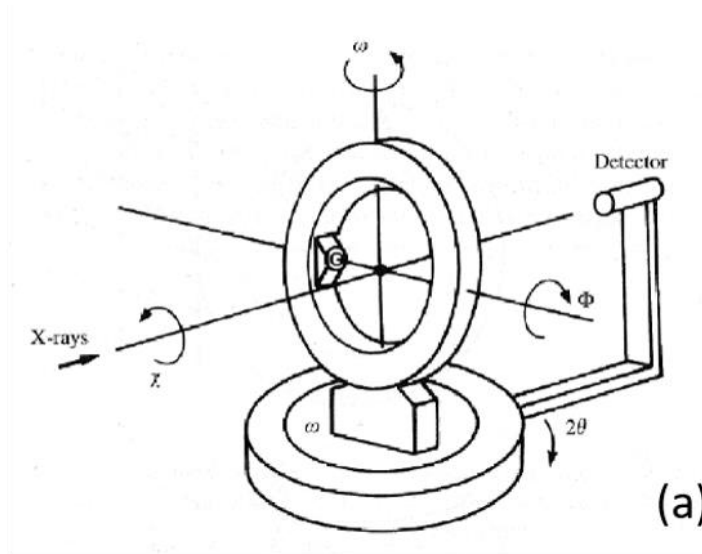
Figure 2.4: Schematics of x-ray diffraction system.[84-88] Four-circle diffractometer with rotation directions (a) and illustration of x-ray diffraction from a periodic lattice (b).

Crystalline materials are composed of stacked planes of infinite regular atomic arrays. Those planes act as diffraction grating for x-rays. The diffracted monochromatic beam from adjacent planes will have a path difference of $2d_{hkl} \sin \theta_{hkl}$, where d_{hkl} is the spacing between the adjacent lattice planes and θ_{hkl} is the angle of incidence of x-ray with respect to the surface

normal [Figure 2.4(b)]. For constructive interference, this path difference must be an integral number of wavelengths of the incident light satisfying Bragg's law,[87]

$$n\lambda = 2d_{hkl} \sin \theta_{hkl} \tag{11}$$

where the d_{hkl} is the spacing between adjacent lattice planes with Miller indices (hkl) and λ is the wavelength of the incident radiation. Figure 2.4(a) shows a schematic representation of x-ray diffractometer. The sample is located at the center of the four rotation axes of the diffractometer.

For out-of-plane measurements, the incidence and detector angles are changed by an amount of θ and 2θ, respectively and corresponding maxima in intensity, called Bragg's peaks, are measured. The positions of these Bragg peaks are compared to the powder diffraction files of prospective material to conform the crystal stoichiometry. Out-of-plane lattice parameters can be determined by calculating d_{hkl} from Braggs equation. General expression for d_{hkl} (e.g., triclinic crystal structure) is given by:[89]

$$\frac{1}{d_{hkl}^2} = \frac{S_{11}h^2 + S_{22}k^2 + S_{33}l^2 + 2S_{12}hk + 2S_{23}kl + 2S_{13}hl}{V} \tag{12}$$

Where,

$$S_{11} = b^2c^2\sin^2\alpha,$$

$$S_{22} = c^2a^2\sin^2\beta,$$

$$S_{33} = a^2b^2\sin^2\gamma,$$

$$S_{12} = abc^2(\cos\alpha \cos\beta - \cos\gamma),$$

$$S_{23} = a^2bc(\cos\beta\cos\gamma - \cos\alpha),$$

$$S_{13} = ab^2c(\cos\gamma\cos\alpha - \cos\beta),$$

and,

$$V = abc\sqrt{1 - cos^2\alpha - cos^2\beta - cos^2\gamma + 2cos \propto cos\beta cos\gamma}$$

For tetragonal crystal structure, $a = b$ and $\alpha = \beta = \gamma = 90°$, Eq. 12 becomes:

$$\frac{1}{d_{hkl}^2} = \frac{h^2 + k^2}{a^2} + \frac{l^2}{c^2} \tag{13}$$

To estimate in-plane lattice parameters, in-plane scan (ϕ-scan) need to be performed to find a reflection with a scattering (k-)vector component in the plane of the sample, which usually involves adjusting the tilt angle χ. After that, a modified version of a θ-2θ is performed to determine the lattice parameter.[90]

The crystal quality can be further characterized by performing a rocking curve scan. This involves scanning of θ along ω direction keeping 2θ fixed at Bragg peak position. Comparing peak intensity and full-width-at-half-maximum (FWHM), an estimation of crystal quality is obtained.

2.5.2. Grazing Incidence X-ray Diffraction Scans (GIXRD)

Generally, θ-2θ XRD is not very effective in case of polycrystalline films because the intensity of the Bragg peaks remain suppressed in comparison to the substrate peaks. Grazing incidence x-ray diffraction (GIXRD) technique is used to investigate polycrystalline films. In the case if GIXRD, the angle of incidence remains fixed at very low angle, $< 5°$, and a detector scan is performed. Using Scherrer's formula[91] to a film peak,

$$l = \frac{k\lambda}{\beta \cos\theta}, \tag{14}$$

where k is the shape factor ~ 0.9, λ is the wavelength of the x-ray used (~0.154 nm) and β is full-width-at-half-maximum (FWHM), the crystal domain size l is obtained.

2.5.3. X-ray Reflectivity (XRR)

In case of x-ray reflectivity, the incidence angle (θ) is kept small, basically below 10°, so that the reflections become sensitive to interfacial film roughness and thickness.[92] Intensity oscillations, called Keissig Fringes, are obtained due to the interference between reflected beams from different interfaces. Using minima fitting with the equation

$$n^2 = m \ sin^2\theta, \tag{15}$$

where

$$m = \frac{4d^2}{\lambda^2}, \tag{16}$$

the thickness of the film, d, is obtained. The thickness and roughness can be determined precisely using the fitting software GenX.[93] This freeware software first determines the optical constants of the different layers from their electron densities and the reflectivity as a function of incidence angle 2θ is calculated from the standard Fresnel's equations. The software also calculates the roughness of surfaces and buried interfaces.

A four-axis Rigaku x-ray diffraction (XRD) system with a Cu K_α rotating anode and a Huber goniometer was used for structural characterization of as grown NbO_2 films used in this study. Different polycrystalline peaks of NbO_2 were verified from corresponding powder diffraction files (PDFs) #00-043-1043.[94]

2.6. X-RAY PHOTOELECTRON SPECTROSCOPY (XPS)

Information about the surface oxidation states was obtained from x-ray photoelectron spectroscopy (XPS) measurements using a PHI 5000 VersaProbe x-ray photoelectron spectrometer. The XPS data were calibrated with respect to the carbon 1s peak at 284.8 eV. XPS
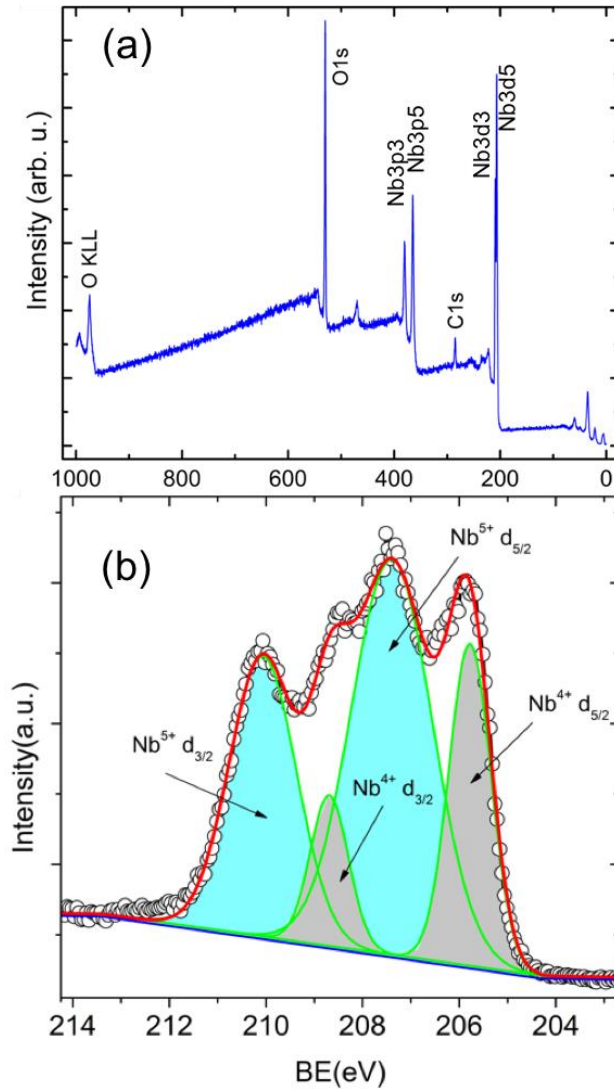
Figure 2.5: XPS scan. (a) A survey scan obtained from NbO_2 film. (b) Detailed peak scan of Nb 3d level peaks. The shaded areas obtained by peak fitting represent Nb^{5+} and Nb^{4+} valance state.

is an important tool to analyze polycrystalline film where XRD is less sensitivities because of the suppressed peak intensity.

Photoelectron spectroscopy utilizes photo-ionization and analysis of the kinetic energy distribution of the emitted photoelectrons to study the electronic state of the film surface. The spectroscopy is based upon a single photon in/electron out process. During XPS, the sample surface is irradiated by monoenergetic soft x-rays with photon energies of 1253.6 eV (Mg K) or 1486.7 eV (Al K). The kinetic energy distribution of the emitted electrons is measured and analyzed to obtain valency state of the film material.

The energy of the incoming radiation is given by[95]

$$E = hv \tag{17}$$

where, h is the Planck's constant and v is the frequency of the incoming radiation. Conservation of energy then requires that

$$E(A) + hv = E(A+) + E(e^-) \tag{18}$$

The electron's kinetic energy (KE) is

$$KE = hv - (E(A+) - E(A))$$

or

$$KE = hv - BE \tag{19}$$

where BE is the binding energy of the electron. When the electron is emitted from the surface, the work function of the material ϕ must be taken into account, such that

$$KE = hv - BE - \phi \tag{20}$$

and therefore, the binding energy is given by:

$$BE = hv - KE - \phi. \tag{21}$$

Figure 2.5(a) shows an example of a survey scan obtained from a NbO_2 thin film. In a survey scan, the entire range of energy (from 0 to 1200 eV) is measured to estimate the types of elements presented in the material. The detailed scan of the desired peaks with a reference peak, for example the C 1s, is then preformed with higher energy resolution. Figure 2.5(b) shows Nb 3d core level spectrum. Because of the multiple valance state of Nb, two peaks are visible at 205.6 and 207 eV, corresponding to 4+ and 5+ valence states of Nb, respectively. Also, due to the electron spin-orbit coupling, each valence state has two peaks (the doublets). A d-shell electron has $l = 2$ and $s = 1/2$, which gives two possible total angular momentum j-values of 3/2 and 5/2 (the doublet), with the latter being lower in energy.

The detailed peak spectra are fitted using Origin software with a Shirley background to obtain peak values and the area as shown in Figure 2.5(b). The fraction of NbO_2 to Nb_2O_5 is obtained by comparing the area under corresponding peaks. The value obtained, however, might not represent the actual fractional value for an *ex-situ* measurement because of the possibility of the post-growth surface oxidation of NbO_2 during transport of the sample to the XPS system.

2.7. TEST DEVICE FABRICATION

2.7.1. Lateral devices

For lateral devices of epitaxial films grown on Al_2O_3, an interdigitated electrode (IDE) structure was used because Al_2O_3 single crystal substrates are highly insulating and therefore there is no way to perform vertical measurements in these samples. IDEs were composed of a 50 nm thick Pt film grown via sputtering at room temperature on top of the samples and patterned using standard photolithography. Photolithography is the process of transferring geometric shapes from a mask to

the surface of the film or substrate. The process involves spin coating, soft baking, mask alignment, exposure and development.

For lateral device fabrication, films were spin coated using photoresist, heated for 30 s at 90 $^{\circ}$C and exposed to UV light for 30 sec. The film was then dipped in a developer solution for 35 s. A 50 nm platinum was sputtered on top of it using sputtering, and then the underlying photoresist was dissolved using acetone, leaving behind the desired IDE structure. The process known as lift-off lithography. Figure 2.6 shows one such device after lift-off. The IDEs had 25 fingers from each side with a length of 500 μm and finger widths and gaps of 5 μm each.

2.7.2. *Vertical Devices*

The current-voltage (*I-V*) characteristics were measured using a probe station tungsten tips (Picoprobe) from GGB Industries Inc. (Figure 2.7) as a top contact. The bottom conducting layers of doped GaN or TiN were used as the bottom contacts. The nominal size of the probe station tip used was ~2 μm. For contact-size dependent conductivity measurements, top Pt contacts were sputtered in form of circles with the thickness of 50 nm and diameters ranging from 6.5 to 0.1 μm, using the e-beam lithography technique. Electron-beam lithography (EBL) is a technique used for nano-device fabrication drawing shapes using a focused electron beam of electron on a target surface covered by an electron sensitive resist. The electron beam changes the solubility of the resist in the solvent, enabling selective removal of the exposed resist during development.

First, the samples were bath-sonicated in acetone, isopropanol alcohol, and DI-water for 5 minutes each. The samples were then heated to 150 °C for 30 minutes using a hot plate. In the next step, the samples were spin-coated using 915 PMMA A4 photoresist and baked at 180 °C for 90 sec. Circular dot patterns with sizes ranging from 0.1 to 10 μm were designed using CAD software and transferred to the sample using e-beam lithography. The developer MIBK:IPA 1:3 solution was used
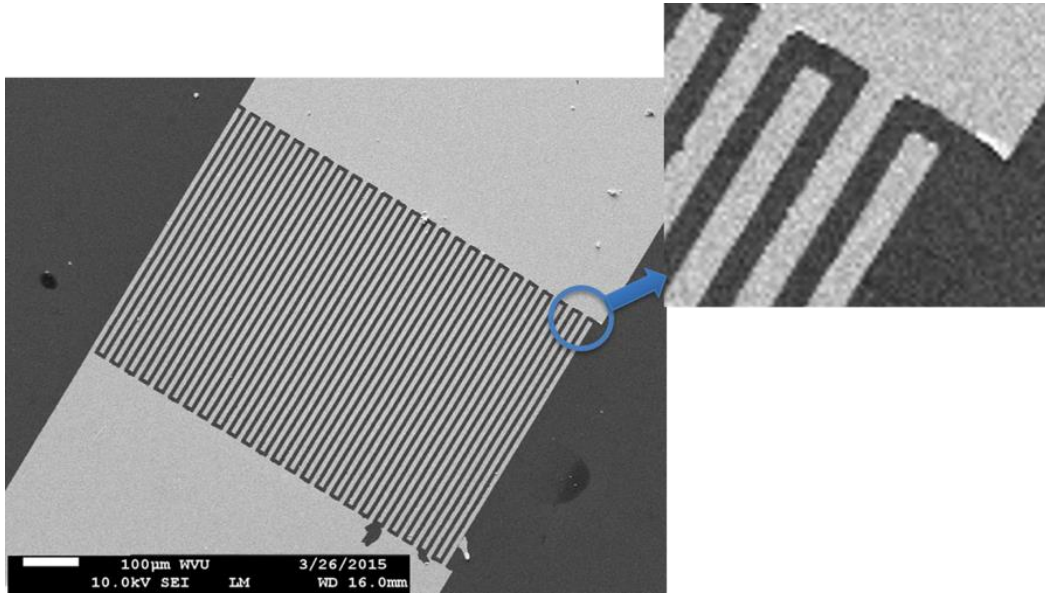
Figure 2.6: An inter-digitated electrode IDE structure used to measure current-voltage characteristic in NbO$_2$ thin film in lateral direction. The left figure shows the zoomed view.

to develop the patterns and a 50 nm platinum was deposited on top of the film. Finally, the photoresist was lifted by dipping samples in acetone for at least an hour.

2.8. ELECTRICAL CHARACTERIZATION

2.8.1. Mechanical Probe Station

A mechanical probe station contains a manipulator and a conductive tip and is used to acquire signals from small electrodes (< 1 mm in diameter). The manipulator allows the precise positioning of thin needles to touch the contact surface. A probe station from GGB Industries and

Figure 2.7: Mechanical probe manipulator with tip.[96]

Picoprobe tip with nominal tip size of 2 μm was used for vertical device measurements (Figure 2.7).

During current-voltage (*I-V*) measurements, a Keithley 2400 sourcemeter was used as a dc voltage source and current meter. Stanford Research DS340 or WAVETEK 182A function generators were used to apply triangular and rectangular pulses to the sample. A Tektronix 224 oscilloscope was used to acquire output data via a LabVIEW automated program.

2.8.2. Conductive Probe Atomic Force Microscopy

Atomic force microscopy (AFM) was used to characterize surface topography. An AFM contains a cantilever with a nanoscale tip with a tip radius of approximately 10 nm. There are two widely used mechanisms for AFM feedback, known as contact and tapping modes. In contact mode, the tip is held at a constant vertical displacement from the surface. Short-range interactions

between the tip and the sample surface create a topographic map of the sample surface.[97,98] In non-contact, or tapping mode, the cantilever is oscillated at its natural frequency and the change in amplitude at each point is used to create topographic map of the surface of interest.[99,100]

Conductive-probe AFM is the powerful technique for electrical characterization. It allows current measurement in the range of 10^{-12} to 10^{-5} A. Also, a simultaneous measurement of surface topography and current measurement is possible using conductive AFM.[97]

In this project, platinum coated conductive tips were used to measure current voltage characteristics. The film surface was scanned to identify the desired contact area. The cantilever tip was moved to the desired place and current-voltage was scanned using voltage sweeps with a 1 Hz frequency.

CHAPTER 3

STRUCTURAL CHARACTERIZATION

In this chapter, I describe the growth and structural characterization of various types of NbO_2 thin films. The films on $Al_2O_3(0001)$ grow epitaxially with a $(110)_T$ (the subscript indicates the tetragonal basis) out of plane orientation. Because the substrate is an insulator, these films were used to fabricate lateral devices where the current is applied in the plane of the sample. Films grown on Si-doped GaN coated Al_2O_3 substrates were also epitaxial and grew along the $(110)_T$ out of plane orientation. Films grown on TiN-coated SiO_2/Si substrates, on the other hand, were polycrystalline. Both Si:GaN and TiN layers are conducting and applicable for vertical device fabrication. Electrical properties of these films with current measured along lateral and vertical direction are presented in CHAPTER 4.

3.1. EPITAXIAL FILMS ON Al₂O₃ SUBSTRATES

Epitaxial thin films of NbO_2 grown on $Al_2O_3(001)$ substrate were studied to determine the role that defects play in the current switching mechanism of NbO_2. The possibility of controlling the stoichiometry and defect density of niobium oxide films with a gradual transformation from the NbO_2 to Nb_2O_5 phase by changing oxygen mass flow during the growth was explored. This

phase transformation was verified using x-ray diffraction (XRD), x-ray photoelectron spectroscopy (XPS), and optical band gap measurements. Current-voltage measurement shown in CHAPTER 4 were consistent with these results.

There are some previous efforts to grow epitaxial quality films by other research groups. Films grown by Wong et al. on Al_2O_3 (0001) substrates using magnetron reactive sputtering resulted in NbO_2 (110) and (111) crystal orientations,[8] while films grown by Posadas et al. on $(La,Sr)_2(Al,Ta)_2O_6$ (111) substrates using molecular beam epitaxy had both (100) and (320) out-of-plane orientations.[9] Wang et al.[101] and Hadamek et al.,[102] on the other hand, were able to grow highly epitaxial thin films of NbO_2 with single $(110)_T$ out of plane orientation using reactive-biased target ion beam and molecular beam epitaxy, respectively.
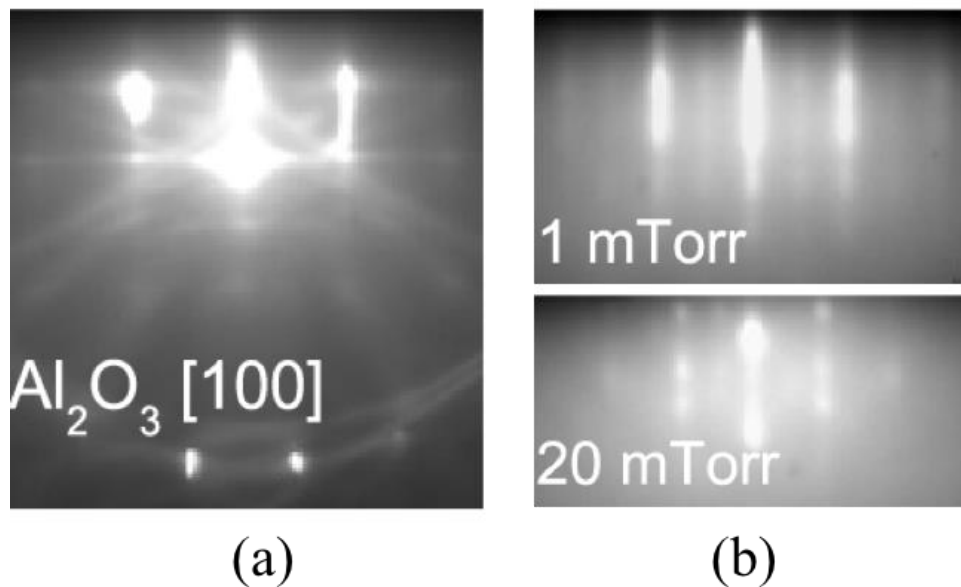
Figure 3.1: (a) RHEED images of the Al_2O_3 substrate along [100] direction. (b) RHEED images of the films grown in 1 mTorr (top) and 20 mTorr (bottom).[103]

The structural characterization techniques used in this project included *in-situ* reflection high energy electron diffraction (RHEED), in-plane and out-of-plane x-ray diffraction (XRD), x-ray reflectivity (XRR), atomic force microscopy (AFM), x-ray photoelectron spectroscopy (XPS) and optical band gap measurement.

3.1.1. **Reflection High Energy Electron Diffraction (RHEED)**

Reflection high energy electron diffraction (RHEED) is the *in-situ* crystal growth monitoring technique. Figure 3.1(a) is the RHEED from the Al_2O_3 substrate with the electron beam along the [100] direction. The RHEED pattern indicated that the substrate surface was clean. Figure 3.1(b) shows RHEED patterns observed during and after the growth of NbO_2 films grown in 1 mTorr (top) and 20 mTorr (bottom) O_2/Ar growth pressure. Streaky patterns indicated that the film surface was relatively smooth. The RHEED spacing between streaks for Al_2O_3 substrates and films grown in 1-15 mTorr was practically the same, while the films grown in 20 mTorr had a smaller RHEED pattern spacing. As discussed in more detail below in Section 3.1.2, the spacings correspond to the formation of NbO_2 and Nb_2O_5, respectively. The pattern of the films grown in 1-15 mTorr also had 6-fold azimuthal rotational anisotropy, in agreement with the existence of three structural twin domains measured via x-ray diffraction, as discussed below in Section 3.1.2.

3.1.2. *X-ray Diffraction (XRD)*

Figure 3.2 shows the θ-2θ scans of x-ray diffraction (XRD) spectra of NbO_2 films grown in 1 to 20 mTorr O_2/Ar pressures. The reference scan obtained from Nb_2O_5 powder scan is shown by the gray curve at the bottom of the figure. Thin film interference fringes around the main film peaks in θ-2θ scans (zoomed view in inset diagram) indicated relatively low film roughness. All films grown in the pressure range of 1 - 15 mTorr had single (110) out-of-plane orientation in terms of the low temperature tetragonal unit cell, in agreement with previous results.[10] The growth
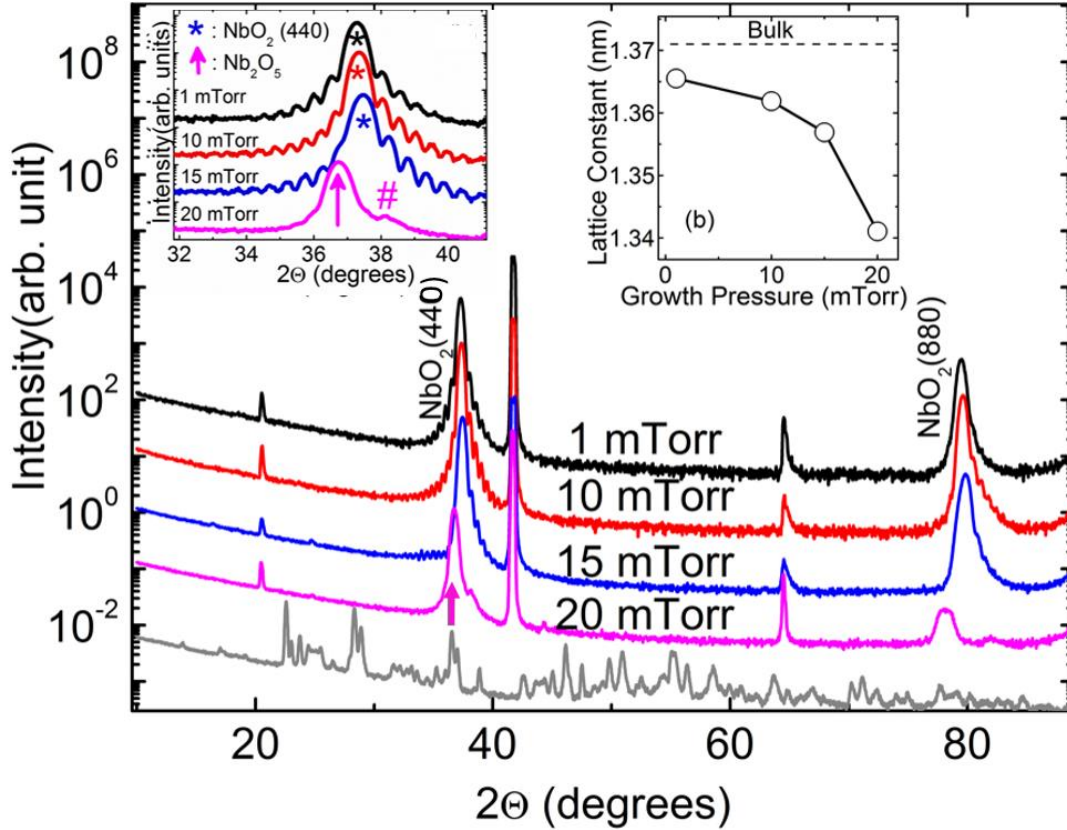
Figure 3.2: X-ray diffraction spectra from samples grown at different growth pressure. (b) Extended view of NbO₂ (440) and Nb₂O₅ [20 mTorr] peaks measured on films grown in 1-15 mTorr and 20 mTorr pressure, respectively. Corresponding lattice parameter are shown to the right inset.[103]

can be best understood if the rutile subcell ($a_R = 4.844$ Å and $c_R = 2.993$ Å)[16] is considered instead of the conventional tetragonal supercell (a_T and c_T), with $[100]_R \parallel [110]_T$ and $[001]_R \parallel [001]_T$. Using the rutile subcell, the $(110)_T = (100)_R$ NbO₂ growth is similar to that of (100) VO₂ on Al₂O₃ (0001) substrates, if the high temperature rutile unit cell of VO₂ is considered.[10]

The films grown in 20 mTorr pressure had a main peak, indicated by the arrow in Figure 3.2, which could not be assigned to a NbO₂ but should correspond to the Nb₂O₅. Due to the

pronounced polymorphism of Nb_2O_5,[50] the exact crystal Nb_2O_5 phase is difficult to determine. Assuming that the initial layer growth took place in the form of NbO_2, due to the favorable lattice match with the substrate, with a subsequent oxidation to Nb_2O_5, then TT-, T- and B-Nb_2O_5 phases[50] could successively or simultaneously form at the substrate temperature 650 °C, with the corresponding unit cells of a = 3.607 Å and c = 3.925Å (pseudo-hexagonal),[52] a = 6.168 Å, b = 29.312 Å, c = 3.936Å (orthorhombic L-phase),[53] and a = 12.744 Å, b = 4.885Å, c = 5.563Å, β = 105.03° (monoclinic).[53] The main peak in Figure 3.2 for the 20 mTorr sample can then be ascribed to (101), (181) or (020) reflections of TT, T or B-Nb_2O_5, respectively. The smaller peak next to it can thus belong either to the strained $(110)_T$ NbO_2 or to the (40-2) B-Nb_2O_5.

A gradual appearance of Nb_2O_5 phase with increasing O_2/Ar pressure was observed in the form of an increasing asymmetry around the $(110)_T$ NbO_2 peaks. The Nb_2O_5 phase is predominant in the film grown in 20 mTorr, as verified by XPS, optical absorption and *I-V* measurements discussed below. Evidently, increasing the O_2 partial pressure during the growth resulted in increasing oxidation rates for Nb^{5+} vs. Nb^{4+} ablated from the Nb_2O_5 ceramic target, while the additional Ar content helped to establish a relatively slow thin film growth.

The inset on the left of Figure 3.2 shows the zoomed view of NbO_2(440) peak while the inset on the right shows the out-of-plane lattice parameters of the film grown in different growth pressures. With increasing growth pressure, the out-of-plane lattice parameter decreased and deviated away from the bulk value. Here, it is assumed that the small peak of the film grown in 20 mTorr belongs to strained $(440)_T$ NbO_2.

Figure 3.3(a) shows the top view of the (001) Al_2O_3 substrate (top), low temperature tetragonal $(110)_T$ NbO_2 film (middle) and high temperature rutile $(100)_R$ NbO_2 crystal structures (bottom). Corresponding lattice axes are shown to the right. Figure 3.3(b) shows the schematic
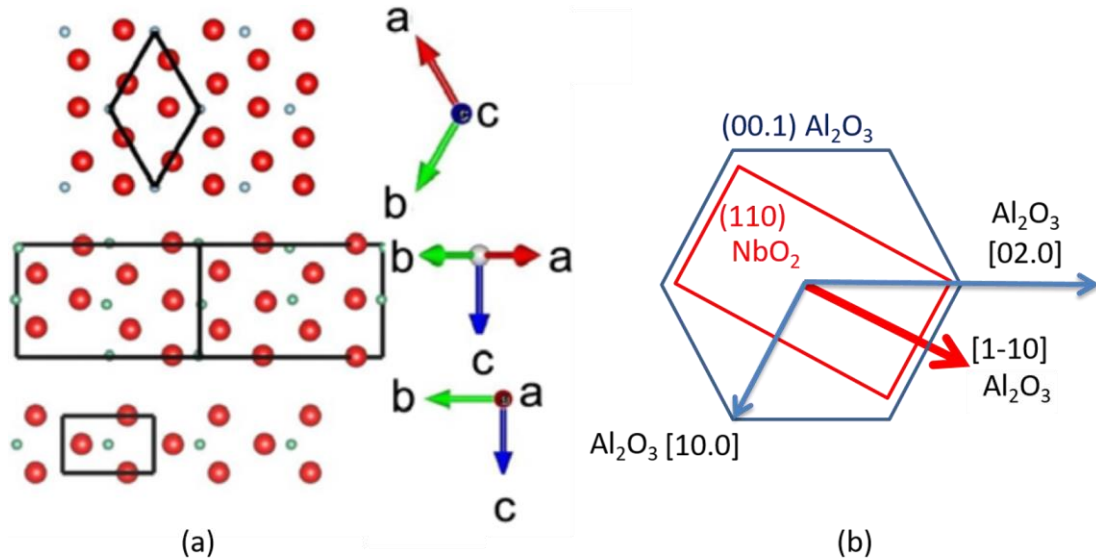
Figure 3.3: Crystal structures of substrate and film. (a) From the top to the bottom: (00.1) Al_2O_3, low temperature tetragonal $(110)_T$ NbO_2, high temperature rutile $(100)_R$ NbO_2. Corresponding lattice axes are shown to the right. Solid black lines signify unit cells. Large (red) and small spheres denote anions (O) and cations (Nb), respectively. (b) Schematic representation of the epitaxial relationship of the $(110)_T$ NbO_2 film with (001) Al_2O_3 substrate.[103]

representation of the epitaxial orientation of $(110)_T$ NbO_2 film and (001) Al_2O_3 substrate. c-axis of the $(110)_T$ NbO_2 lies along [1-10] of (001) Al_2O_3 thus providing Nb-Nb dimerization and distortion of NbO_2 along the substrate plane as discussed in Section 1.7.2.[10] Estimated in-plane lattice mismatch between film and substrate is about -1.2% along [100] and -4.5% along [1-10] direction of the substrate.

Rocking curve scans (Figure 3.4) were performed using a Bruker XRD system around the (440) and (0006) reflection of NbO_2 film grown in 10 mTorr total pressure and Al_2O_3 substrate, and the corresponding full-width-at-half-maximum (FWHM) values were found to be 0.02 and
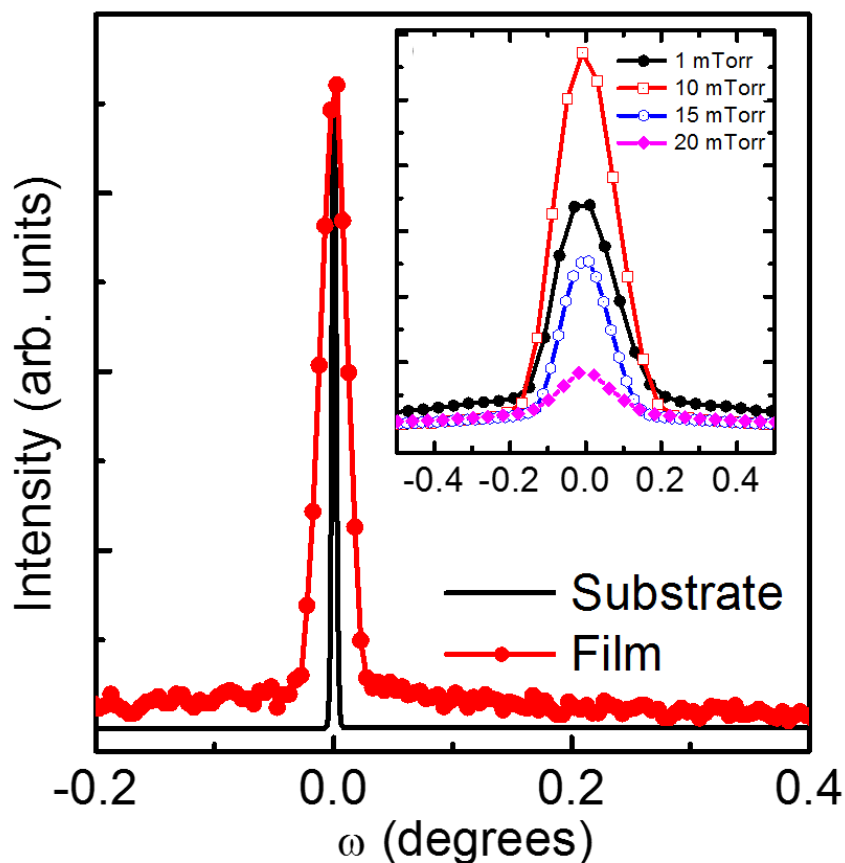
Figure 3.4: Rocking curve of (440) and (0006) peak of NbO_2 film grown in 10 mTorr pressure and Al_2O_3 substrate, respectively using Bruker XRD. Inset figure shows rocking curves of the films grown in 0.1 to 20 mTorr measured using Rigaku XRD.[103]

0.003 degrees, respectively, thus indicating the high degree of the out-of-plane and in-plane crystalline orders in NbO_2 thin films. These FWHM values were also lower than those reported in Ref. 9 (FWHM = 0.07°) and those in Ref. 8 (FWHM = 0.18°). Rocking curve scans performed using Rigaku XRD system on all of the films grown in 1 to 20 mTorr are shown in inset of Figure 3.4. Film grown in 10 mTorr has the largest intensity with the smallest FWHM.
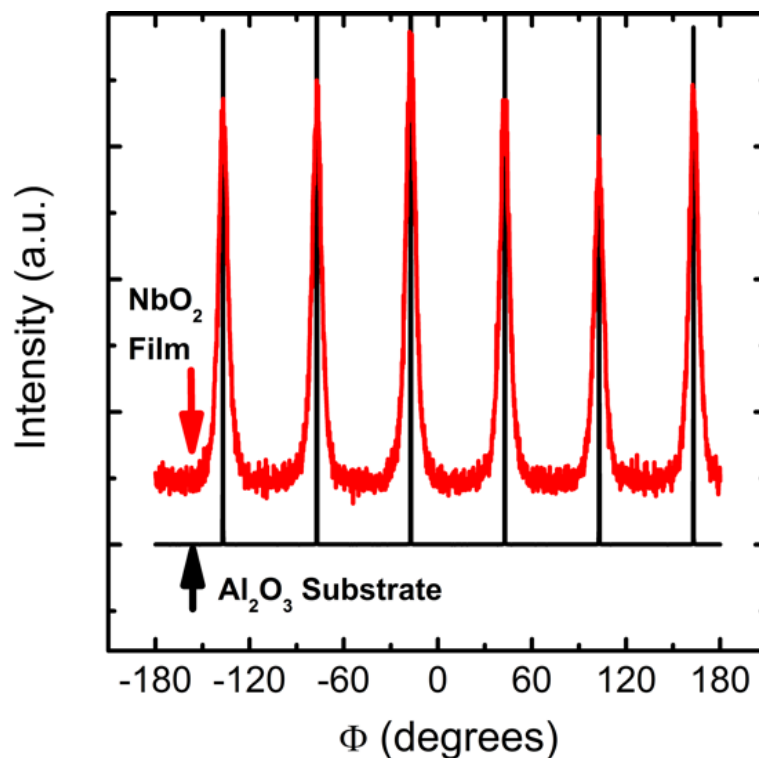
Figure 3.5: ϕ-scans of (202) and (400) peaks from the Al_2O_3 substrate and NbO_2 film grown in 10 mTorr, respectively.[103]

The in-plane orientation of the film with respect to the substrate was determined from XRD ϕ-scans of (202) and (400) peaks for the Al_2O_3 substrate and NbO_2 films, respectively. Figure 3.5 shows result for the film grown in 10 mTorr pressure. A six-fold rotational symmetry of the film was found, which is explained by the presence of three twin NbO_2 growth domains with the corresponding {001} of the tetragonal NbO_2||{1–1.0} axis of the Al_2O_3 substrate, i.e. along the oxygen sub-lattice main axis (in agreement with Ref. 8), thus confirming the in-plane epitaxy of the films.
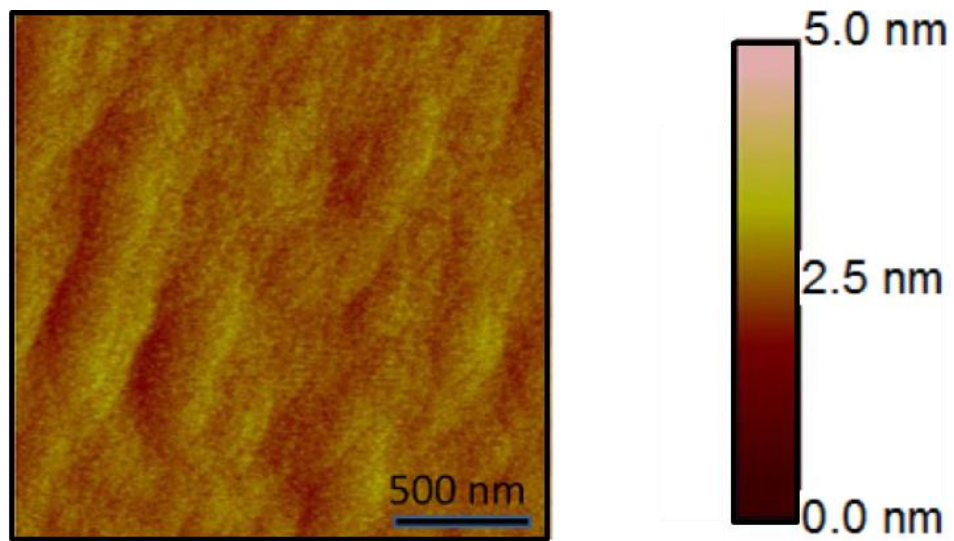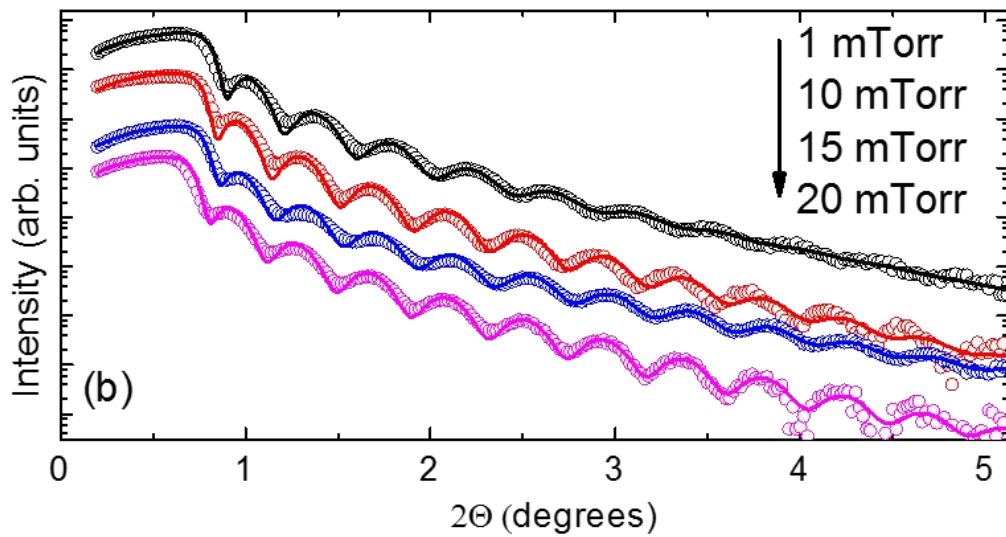
Figure 3.6: (a) Atomic force microscopy image of NbO_2 film grown in 1 mTorr pressure. (b) X-ray reflectivity spectra measured on NbO_2 films grown in different pressures (open circles) with the corresponding fits (solid lines).[103]

X-ray diffraction (XRD), however, is not sensitive to amorphous part of the film. X-ray photoelectron spectroscopy (XPS) is an important tool to determine if any other phases of niobium oxide are presented in the film in amorphous form. XPS performed with these samples is discussed below in Section 3.1.4.

3.1.3. X-ray Reflectivity (XRR) and Atomic Force Microscopy (AFM)

Figure 3.6(a) shows the representative atomic force microscopy (AFM) image of a film grown in 1 mTorr pressure. All films were smooth without any grain formation. Root-mean-square (RMS) roughness of this film was 0.3 nm. X-ray reflectivity scans of the films grown in $1 - 20$ mTorr [Figure 3.6(b)] had thickness approximately 20 nm, 19.4 ± 0.6 nm, and the surface roughness obtained from the fits using GenX software was approximately 0.5 nm. The roughness obtained from XRR is slightly larger than the roughness obtained from AFM due to the difference in the active area of the scan. The area covered by an x-ray beam is in the range of 1 mm^2, several orders of magnitude larger than the AFM scan area.

3.1.4. X-ray Photoelectron Spectroscopy (XPS)

XPS Nb 3d level core spectra are shown in Figure 3.7. Films grown in 1 to 15 mTorr exhibited two $3d_{5/2}$ level peaks of Nb at 205.4 and 206.9 eV. With decreasing growth pressure, the intensity of the peak at 205.4 eV increased while the intensity of the peak at 206.9 eV decreased. Thus, the 205.4 eV and 206.9 eV peaks are related to lower and higher Nb valencies, respectively. The reference spectrum taken on Nb_2O_5 powder (solid line curve in Figure 3.7) confirmed that the most intense peak at 206.9 eV was from the $3d_{5/2}$ level of Nb^{+5}. Similarly, $3d_{3/2}$ level peaks were found at 209.6 eV and at 208.2 eV for Nb^{+5} and Nb^{+4}, respectively, as shown by de-convoluted peaks in the inset of the Figure 3.7.
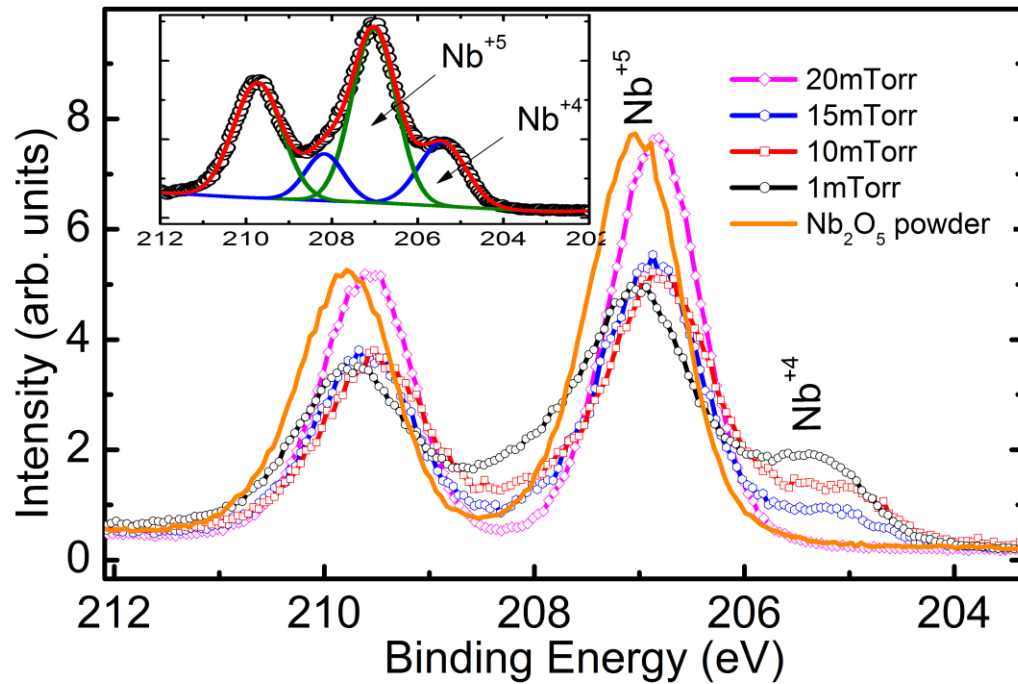
Figure 3.7: X-ray photoelectron spectroscopy pattern of the NbO_2 films grown in different growth pressures. Inset shows de-convoluted peaks for the film grown in 10 mTorr. The solid curve with orange color is the reference spectrum taken on Nb_2O_5 powder.[103]

There are two views about XPS NbO_2 data in the literature. One group of authors[7,10,104] has claimed that the most intense and less intense peaks at 206.9 eV and at 205.4 - 205.6 eV correspond to $3d_{5/2}$ peaks of Nb^{5+} and Nb^{+4}, respectively, while another group[9,105-107] assigned them to Nb^{+4} and Nb^{3+}. My interpretation agrees with that of the first group. Therefore, decreasing the total growth pressure with constant oxygen mass flow content helped to reduce the nominal Nb^{5+} in Nb_2O_5 to Nb^{4+}.
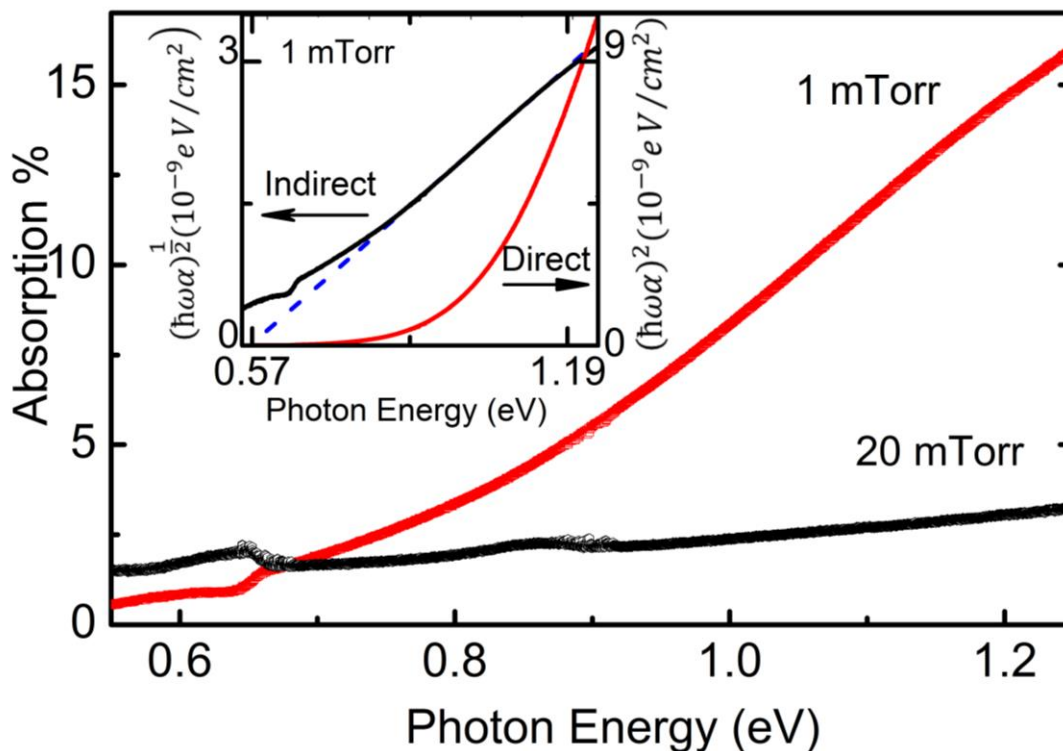
Figure 3.8: Optical absorption spectra for the predominant NbO_2 and Nb_2O_5 film phases grown in 1 and 20 mTorr, respectively. The inset shows Tauc plots, $(\hbar\alpha\omega)^n$ vs. $\hbar\omega$, where α is the absorbance and $\hbar\omega$ the photon energy, for the NbO_2 film grown in 1 mTorr. Left and right scales correspond to indirect ($n = 1/2$) and direct ($n = 2$) optical transitions, respectively. Blue dashed line signifies linear fit for the indirect band gap $E_g = 0.57$ eV.[103]

The presence of the XPS peaks identified as Nb^{5+} for the samples which were characterized by XRD as pure NbO_2 (e.g. sample grown at 1 mTorr) can be explained by the existence of a thin (1-2 nm) surface Nb_2O_5 layer formed after exposure to atmosphere.[10,11] XPS measurements were performed *ex-situ* and the samples were exposed to the atmosphere for several hours before inserting them in the XPS chamber.

3.1.5. Band Gap Measurement

Based on the structural characterization, samples grown in 1 mTorr and 20 mTorr were identified as NbO_2 and Nb_2O_5 phases, respectively. This was confirmed by optical band gap measurements shown in Figure 3.8. The sample grown at 1 mTorr exhibited a band gap of NbO_2 which is approximately 0.6 eV, in agreement with the previous literature values reported 0.3 - 0.4eV,[10] 0.5 eV,[108] 0.7 eV,[11] 0.88 eV,[23] and at least 1.0 eV.[9] The sample grown in 20 mTorr pressure, on the other hand, showed no significant absorption within the photon energy range, in agreement with the higher Nb_2O_5 band gap energy ranging from 3.5 to 4.8 eV.[11,109,110] The small, broad peaks near 0.65 eV and 0.9 eV are due to water absorption in air.

To further determine the nature of the band gap in NbO_2, Tauc plots were graphed (Figure 3.8 inset), i.e. the absorption coefficient α was plotted as $(\hbar\omega\alpha)^n$ vs. the photon energy $\hbar\omega$ with n = 1/2 and n = 2, which are related to indirect and direct transitions, respectively.[111] The best fit was found for n = 1/2, thus confirming an indirect band gap of 0.57 eV for NbO_2, in agreement with band structure calculation by Weibin et al.[11]

3.2. EPITAXIAL FILMS ON GaN SUBSTRATES

Another substrate used to grow epitaxial NbO_2 consisted of a GaN(001) layer grown epitaxially on top of Al_2O_3(001). Since, a_{GaN} = 3.186 Å and $a_{Al_2O_3}$ = 4.785 Å ($3a_{GaN} \sim 2a_{Al_2O_3}$), both substrates provide similar lattice mismatch to $(110)_T$ NbO_2.[112] Thus, NbO_2 grows epitaxially with a $(110)_T$ orientation as it does on Al_2O_3(001). In this section, the structural characterization of epitaxial thin film of NbO_2 grown on GaN coated wafers is described. Being optically transparent, films grown on GaN could have other optoelectronic applications. For this project, however, the film was used for vertical device characterization of the epitaxial thin film. Like Al_2O_3, the intrinsic

GaN layer is also insulating. For vertical device characterization, a conducting doped Si:GaN layer was used instead, which is discussed later in Section 3.4. During growth of NbO_2 films, a NbO_2 target was used instead of the Nb_2O_5 target used in previous experiments, which therefore required a lower fraction of oxygen pressure in Ar/O_2 gas mixture used during growth.

Figure 3.9 shows a RHEED pattern obtained from a 25.9 nm film grown at 650 °C and 2 mTorr growth pressure with approximately 1% O_2 by mass flow verifying the epitaxial relationship of the film with the substrate. Streaky patterns with some reconstruction indicate excellent quality of the film, which is similar that of the film grown on Al_2O_3 substrate.

Figure 3.10 shows a θ-2θ scan of the epitaxial film grown on (undoped) GaN coated Al_2O_3 substrate. There were multiple peaks visible but most of the peaks corresponded to the Al_2O_3, and GaN layer of the substrate indicated by the symbols '•' and '∇'. Peaks at 37 and 78° (denoted by symbol '*') were from (110)-orientation of low temperature tetragonal NbO_2 which were verified using powder diffraction file PDF#00-043-1043.[94] Thus, the film grew in a similar way to the film grown on Al_2O_3 (001) as discussed in Section 3.1.
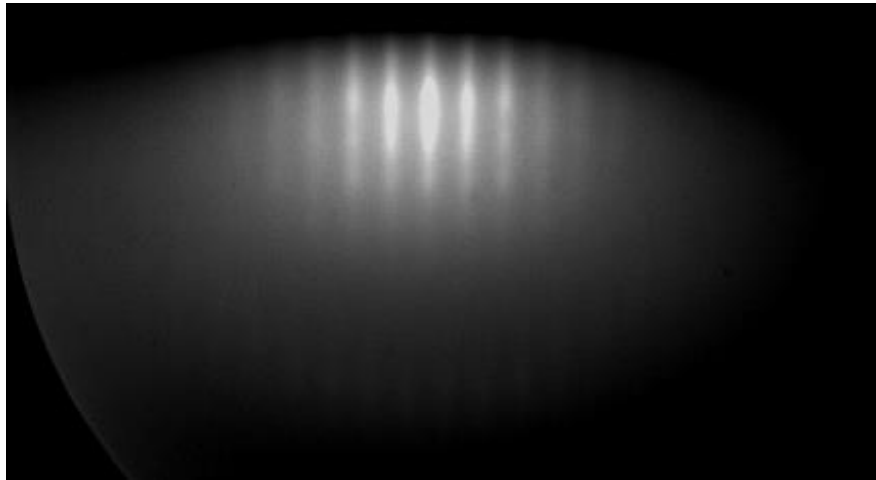
Figure 3.9: Mechanical RHEED image of NbO_2 film grown on GaN coated wafer.
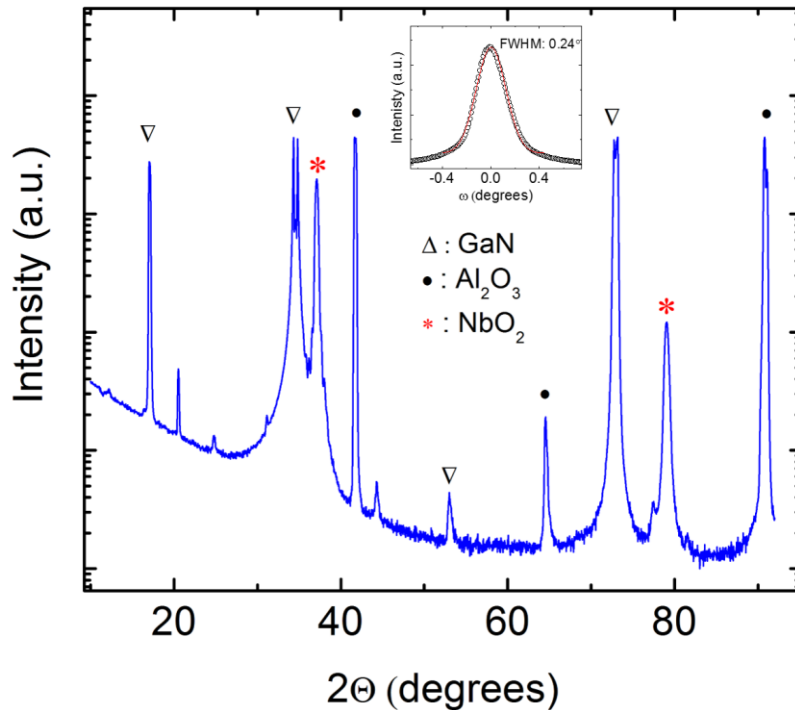
Figure 3.10: X-ray diffraction spectrum from sample grown on GaN coated substrate in 2 mTorr O_2/Ar mixed pressure with 1% O_2 by mass flow. Inset shows the rocking curve of $(440)_T$ peak with FWHM of 0.24°.

The inset of Figure 3.10 shows the rocking curve of $(440)_T$ peak. The FWHM obtained from the Gaussian peak fitting was ~0.24°, which was similar to the FWHM of the films grown on Al_2O_3 (Figure 3.4, inset). No peaks related to Nb_2O_5 or NbO phases were observed.

The x-ray reflectivity of the film is shown in Figure 3.11, which indicates that the film on GaN coated substrate also was smooth with a surface roughness of 0.4 nm, similar to the film grown on Al_2O_3 substrate (Figure 3.6).

Figure 3.12 showed x-ray photoemission (XPS) of the epitaxial film grown. Here, molar ratios of NbO_2 to Nb_2O_5 phases in the films were compared using the area covered by Nb^{4+} and Nb^{5+} valance state spectra. The peak fit was performed using Origin with Gaussian line shapes and
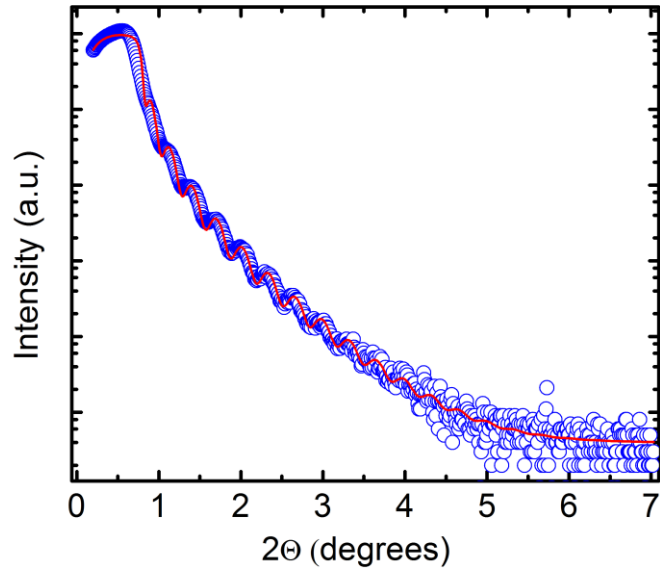
Figure 3.11: X-ray reflectivity curve from sample grown on GaN coated Al_2O_3. Thickness of the film was 25.9 nm with roughness of 0.4 nm.
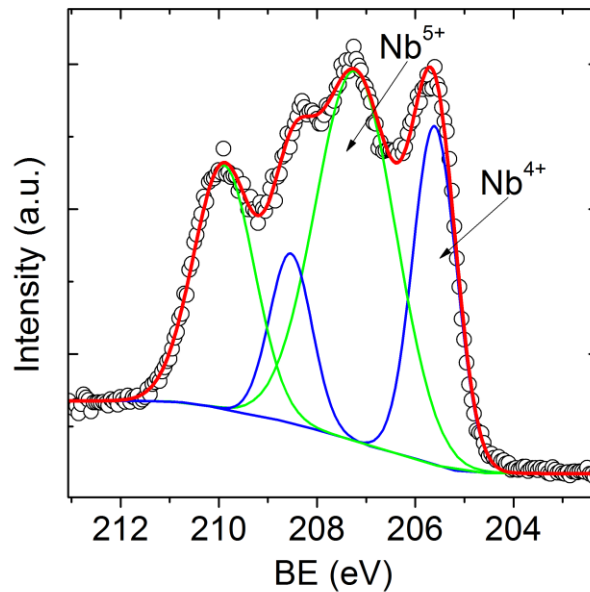
Figure 3.12: X-ray photoelectron spectroscopy pattern of the NbO_2 film grown on GaN coated substrate. Peaks were fitted using Origin with Shirley background. Fraction of NbO_2/Nb_2O_5 obtained from fit is 34%.

Shirley-type background. The ratio of the area covered by Nb^{4+} and Nb^{5+} valance state peaks showed that the film contained approximately 34% NbO_2 and 66% Nb_2O_5. The proportion of NbO_2 in the film grown on GaN layer is significantly higher in comparison to the film grown directly on Al_2O_3 substrates [Figure 3.7 vs. Figure 3.12]. An exact determination of the oxygen stoichiometry, however, is not possible via *ex-situ* measurements because of the film surface oxidation after exposure to the air. The obtained spectra, therefore, contain the combined response from Nb^{5+} states in the oxidized top layer plus Nb^{4+} and Nb^{5+} (if any) in the film bulk.

To compare the electrical properties of epitaxial and polycrystalline films, NbO_2 was grown on TiN coated substrate and Si:GaN substrate using similar growth conditions. Structural characterization of the two of the films grown for this purpose are discussed in Section 3.4 to verify identical film thickness and NbO_2/Nb_2O_5 fraction but different crystal quality.

3.3. POLYCRYSTALLINE FILMS

Fabrication of vertical device requires a bottom conducting layer which is used as a bottom contact. TiN is widely used in the electronics industry as a conductive layer that resists interdiffusion with silicon. In this project, silicon wafers coated with TiN, provided by Micron Corp. for integration of NbO_2 with silicon wafers were used. TiN was used as a bottom contact layer for vertical device measurement. The structural characterization of polycrystalline films grown on the TiN coated substrate are discussed in this section.

Several groups have performed polycrystalline[113] and amorphous[3,4] NbO_2 thin film growth. Device characterization, however, has been performed only by a few of them[5,30,114-116] using amorphous NbO_2 films. Growth-related issues, such as stability of bottom contact material and

relatively high leakage current, are still preventing this material from being suitable for practical electronic appliances.

In the case of amorphous films, it is suggested that a crystalline conducting path is formed during the forming process. Crystallization is mainly governed by nucleation of the thin film material followed by crystal growth.[117] Continuous increase in crystalline area and crystal grain size results in an unstable switching mechanism. OFF-state leakage currents greater than 10^{-5} A, reported so far[5,30,114-116] cause power dissipation greater than 10 µW per bit, assuming the operation voltage of 1 V.

Wang et al. have recently performed a study on polycrystalline film grown on TiN coated substrates where temperature dependent study of switching mechanism with and without Nb top contacts.[113] Growth pressure, thickness and contact size dependent studies, however, were not reported by authors.

Table 2: List of NbO_2 polycrystalline thin film samples used in this work. The symbol NbO represents NbO_x films and the numbers in the bracket for NbO(1) and NbO(10) represent the growth pressures: 1 and 10 mTorr, respectively. The numbers in the brackets for the film grown in constant growth pressure of 2 mTorr represent the oxygen mass flow during the growth with total mass flow of 28.5 sccm.

Target Material	Sample Symbols	Thickness (nm)	p_{total} (mTorr)	O_2 Mass flow %	NbO_2 %
Nb_2O_5	NbO(1)	43.7	1	7	36.3
	NbO(10)	33.2	10	7	24.8
NbO_2	NbO(0.3)	22.4	2	1	35.9
	NbO(0.6)	29.8	2	2.1	34.4
	NbO(1.2)	27.9	2	4.2	24.3
	NbO(1.8)	23.3	2	6.3	4.9

For this project, I performed a detailed investigation of structural and electrical properties of NbO_2 polycrystalline thin films grown using PLD on TiN coated SiO_2/Si substrates in order to help further the development of NbO_2 related electronic technologies. I mainly studied the type of defects in the film and their correlation with the switching mechanism.

Two types of target materials were used for polycrystalline film growth: NbO_2 and Nb_2O_5. Two of the films grown in 1 and 10 mTorr O_2/Ar (7%) mixed growth pressure using Nb_2O_5 target will be discussed. Four other films were grown using the NbO_2 target at 2 mTorr O_2/Ar mixed pressure with $1 - 10\%$ of O_2 by mass flow. These samples are listed in Table 2.

3.3.1. X-ray Diffraction (XRD)

Figure 3.13 shows XRD scans of the NbO_2 films, labeled as NbO(1), grown in 1 mTorr Ar+O_2 (~ 7% O_2) pressure and having a thickness of approximately 44 nm. All peaks related to different crystalline orientations of NbO_2 were verified using PDF#00-043-1043.[94] The sharp peaks denoted by '●' in the out-of-plane θ-2θ scans are related to (100) Si substrate while all other peaks are related to polycrystalline and orientated sample peaks (labeled with red front). Grazing incidence x-ray diffraction (GIXRD) scans were performed using an angle of incidence (α) ranging from 0.25 to 5° on the polycrystalline films. All peaks related to different crystalline orientations of NbO_2 were visible in both types of XRD scans. Except for the case of very small α (= 0.25°), the intensity of the peaks remained constant with increasing α. This indicated that the film quality remains unchanged for the entire film thickness.

Similarly, Figure 3.14 shows θ-2θ and GXRID scans of the NbO_2 film labeled as NbO(10), grown in 10 mTorr Ar+O_2 pressure and having a thickness of 33.2 nm. For the NbO(10) film, additional peaks are visible due to (010) SiO_2 (represented by '⇓'). The intensity of the peaks increases with increased α. The appearance is explained by crystallization of SiO_2 at the growth
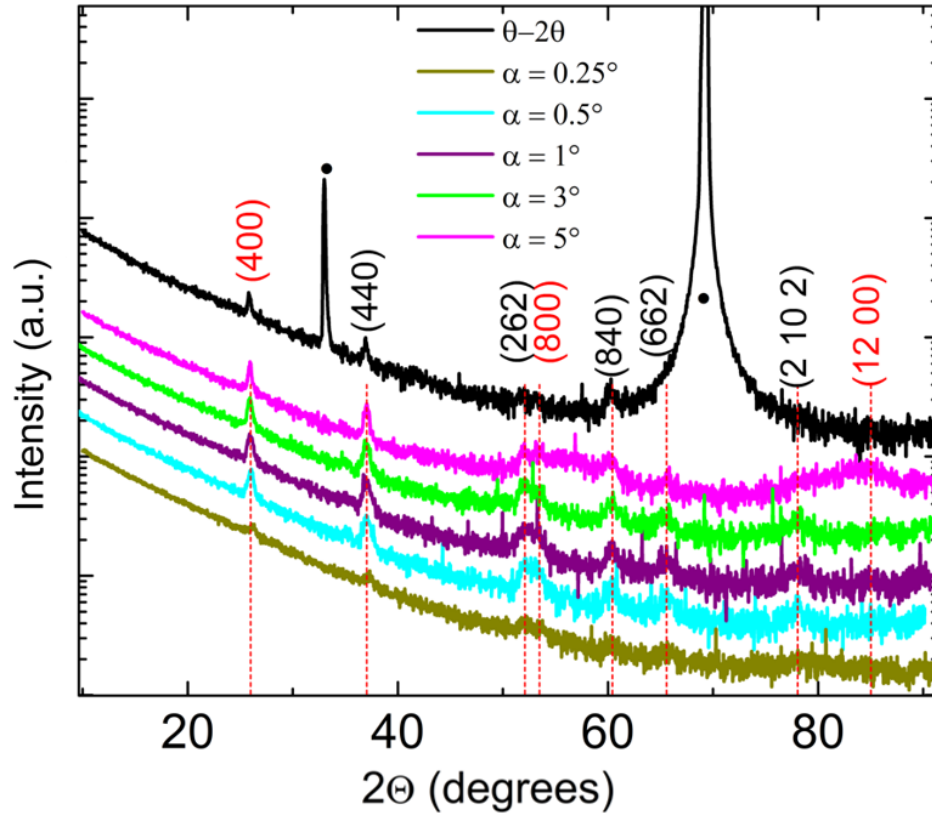
Figure 3.13: θ-2θ and grazing incidence x-ray diffraction (GIXRD) patterns of NbO₂ film NbO(1). Grazing incidence angles (α) used were 0.25 - 5°. Vertical dotted lines represent the peak position from the powder diffraction file (PDF) # 00-043-1043. The peaks indicated by the '●' symbol in the out-of-plane θ-2θ scan are from the (100) Si substrate. All other peaks are related to polycrystalline NbO₂ with some orientated peaks (labeled with red front).

substrate temperature in the oxygen atmosphere. SiO₂ peaks in the sample NbO(1) (Figure 3.13) were absent, which was grown under lower O₂ pressure. No peaks related to Nb₂O₅ or NbO phases were observed in either case.

Using Scherrer's formula,[91]

$$l = \frac{k\lambda}{\beta \cos\theta},$$
(22)
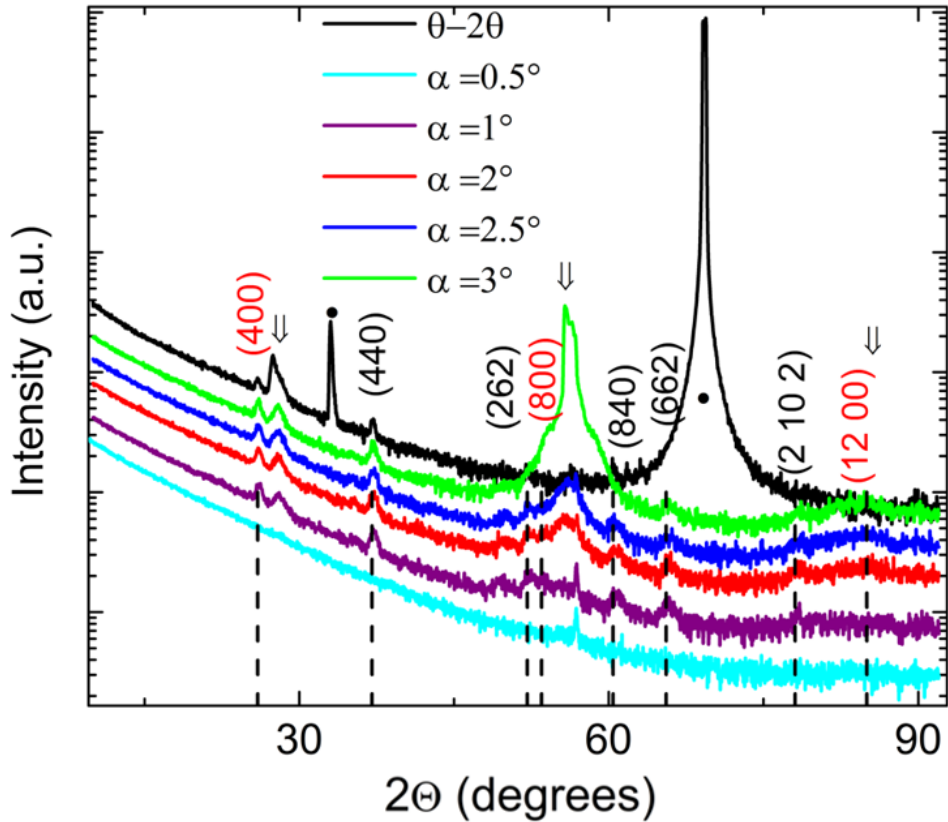
Figure 3.14: θ-2θ and grazing incidence x-ray diffraction (GIXRD) patterns of NbO$_2$ film NbO(10). Grazing incidence angle (α) used was 0.5 - 3°. Vertical dotted lines represent the peak position from the powder diffraction file (PDF) # 00-043-1043. The peaks indicated by the '●' symbol in the out-of-plane θ-2θ scan are from the (100) Si substrate. All other peaks are related to polycrystalline NbO$_2$ with some orientated peaks (labeled with red front).

where k is the shape factor ~ 0.9, λ is the wavelength of the x-ray used (~0.154 nm) and β is full-width-at-half-maximum (FWHM) for (400) NbO$_2$ peak at 2θ = 25.9°, the crystal domain size $l =$ 16 ± 2 nm was obtained.
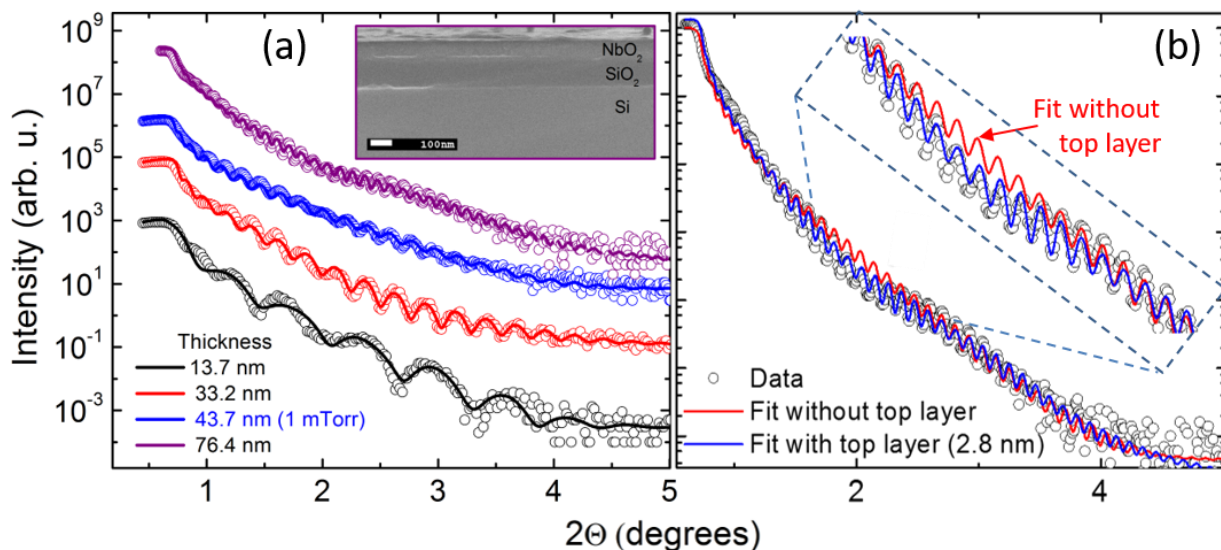
Figure 3.15: X-ray reflectivity (XRR). (a) XRR of NbO_2 films with GenX fitting. Circular symbols represent raw data and solid lines represent the fits. The data with blue solid circles are from 43.7 nm film grown in 1 mTorr total pressure. Inset figure shows the cross-sectional SEM image of the film with thickness 76.4 nm. (b) XRR of 76 nm NbO_2 film with GenX fitting without a top layer (red) and with a 2.8 nm top layer (blue). Inset shows the zoom of 2θ-scale between $1.2 - 2.3°$.

3.3.2. X-ray Reflectivity (XRR)

Figure 3.15 shows x-ray reflectivity curves for the samples with the thickness ranging from 13.7 to 76.4 nm and grown into 1 mTorr (blue solid circles symbols) and 10 mTorr pressures. Fittings (solid lines) were performed using GenX software. The bottom TiN layer had the thickness of 11 nm with the roughness of ~0.4 nm. The maximum film roughness obtained was about 1 nm for 76.4 nm thick film.

The fitting was performed assuming a top layer with the thickness about 2.7 nm with a slightly different index of refraction, which might be a Nb_2O_5 layer formed by oxidation of NbO_2 after exposure to the atmosphere. The fitting with and without a top layer is shown in Figure
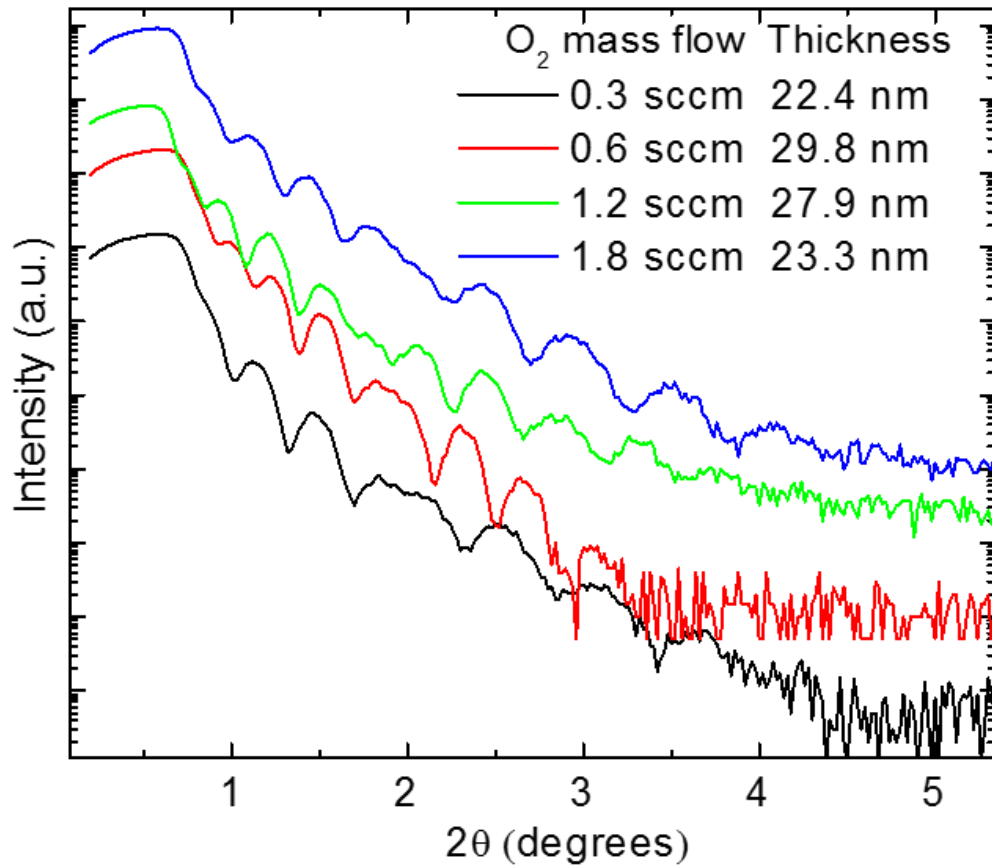
Figure 3.16: X-ray reflectivity (XRR) of films grown in different oxygen mass flow from 0.3 to 1.8 sccm as listed in top right corner.

3.15(b) for the 76.4 nm film, which showed that the model with an additional top layer fits better.

The inset of Figure 3.15(a) shows a cross-sectional SEM image of 76.4 nm film. All four layers: Si, SiO_2, TiN and NbO_2 with thickness matching with nominal values were visible.

Figure 3.16 shows the x-ray reflectivity measured from the set of samples grown at 2 mTorr growth pressure using varying oxygen mass flow concentrations. All films were grown using NbO_2 target and all films were grown using similar growth conditions expect the oxygen concentration. Oxygen mass flow was varied from 0.3 sccm to 1.8 sccm keeping total mass flow ~28.5 sccm. The
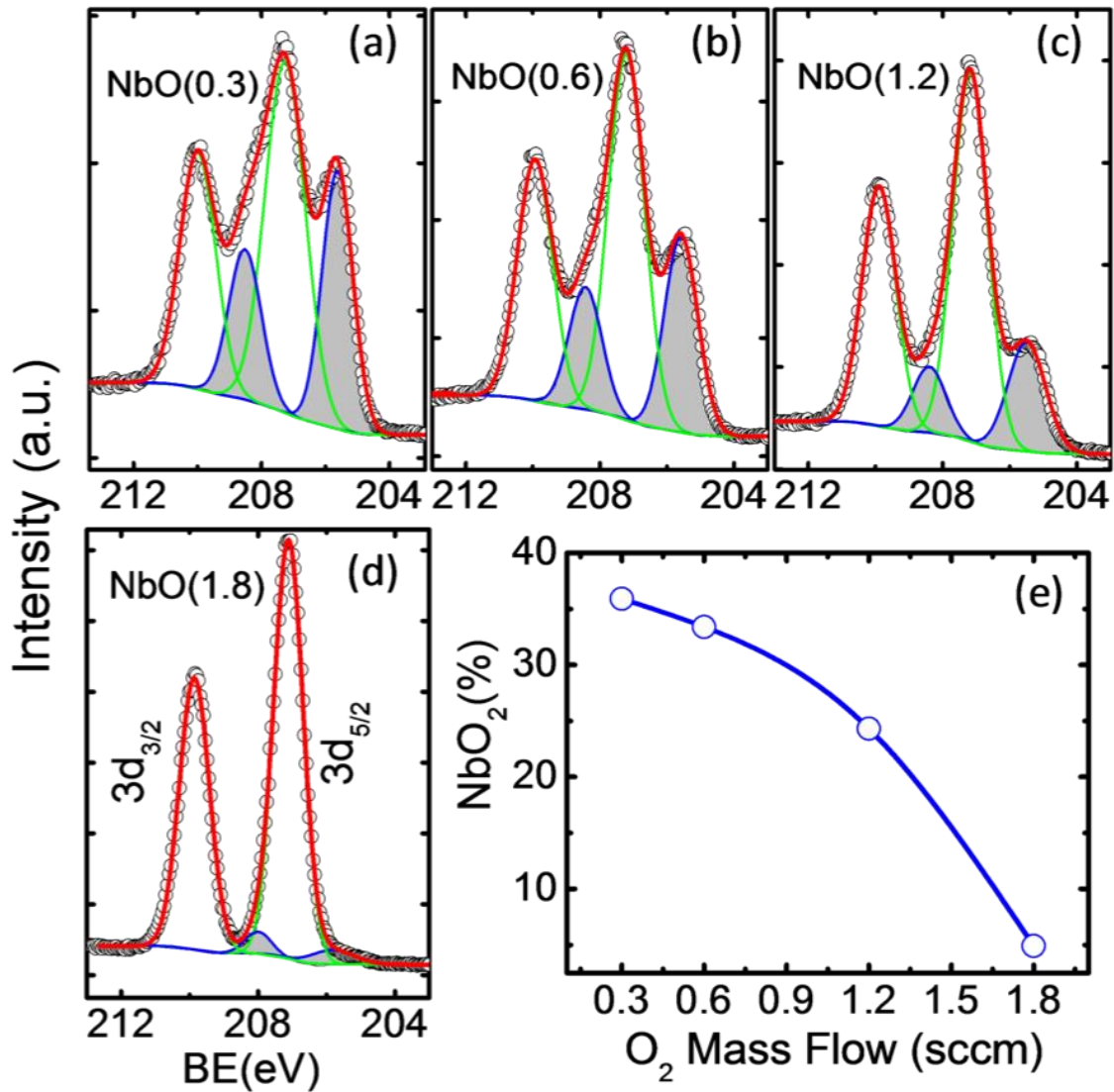
Figure 3.17: X-ray photoelectron spectroscopy pattern of the NbO_2 film grown on TiN coated substrate using oxygen mass flow (a) 0.3 sccm, (b) 0.6 sccm, (c) 1.2 sccm, and (d) 1/8 sccm. (e) Fraction of NbO_2 to Nb_2O_5 obtained from peak fit.

thickness was found different from each other as listed in top right corner of Figure 3.16 and tabulated in Table 2.

3.3.3. *X-ray Photoelectron Spectroscopy (XPS)*

The molar ratios of NbO_2 to Nb_2O_5 crystal phases present in films were measured using Nb-edge 3d core level XPS spectra. Figure 3.17 shows XPS spectra measured on the films grown in 2 mTorr total growth pressure with different oxygen partial pressure values. The shaded areas represent the contribution from the NbO_2 phase. The deconvoluted peak fits show that peaks from Nb^{4+} state of Nb were at about 205.6 and 209 eV, in agreement with previous studies.[7,8,104] Predominant peaks at 207 and 210 eV were observed for Nb^{5+} state of Nb, probably due to the surface oxidation of the film after exposer to the atmosphere. The shaded areas mark the peaks related to Nb^{4+}, i.e. to NbO_2 phase.

With increasing O_2 mass flow, the resulting relative fraction of the NbO_2 phase decreased as shown in Figure 3.17(e). With increased oxygen concentration during growth, the valency state of Nb increases, thus increasing the proportion of Nb_2O_5. Estimation of the exact oxygen stoichiometry, however, is not possible using *ex-situ* measurement due to the possibility of surface oxidation of the film after exposer to the atmospheric oxygen. The large Nb^{5+} valency peak might result from the top oxidized part of the film.

3.4. POLYCRYSTALLINE VS. EPITAXIAL FILMS

In this section, the structural quality of two of the NbO_2 films grown on Si-doped epitaxial GaN on Al_2O_3 and TiN coated SiO/Si substrates are compared. The structural characterization of NbO_2 film grown on intrinsic GaN was already presented in Section 3.2. The overall idea here is to prepare two films using similar growth conditions so that the films having identical thickness and chemical compositon but different crystal quality can be compared. The film grown on Si doped GaN had epitaxial quality similar to the film grown on undoped GaN and the film grown

on TiN was polycrystalline, as discussed in previous sections. The electrical properties of these films will be compared later in CHAPTER 4.

Epitaxial GaN (150 um)/AlN (350 nm)/Al_2O_3 templates from MTI Corporation and TiN(11 nm)/SiO2(100 nm)/Si wafers provided by Micron Technology with nominal surface roughnesses < 0.5 nm were used as substrates for growth. Both of the films were grown using similar growth condition using pulsed laser deposition (PLD). The nominal substrate temperature during growth was 650 °C. Films were grown in 2 mTorr O_2/Ar mixed gas atmosphere with approximately 1% O_2 mass flow and ~28.5 sccm total mass flow. The structural characterization, here, also includes reflection high-energy electron diffraction (RHEED), *ex-situ* x-ray photoelectron spectroscopy (XPS), x-ray diffraction (XRD), x-ray reflectivity (XRR) and atomic force microscopy (AFM). In case of polycrystalline film, grazing incidence x-ray diffraction(GIXRD) scan was also performed.
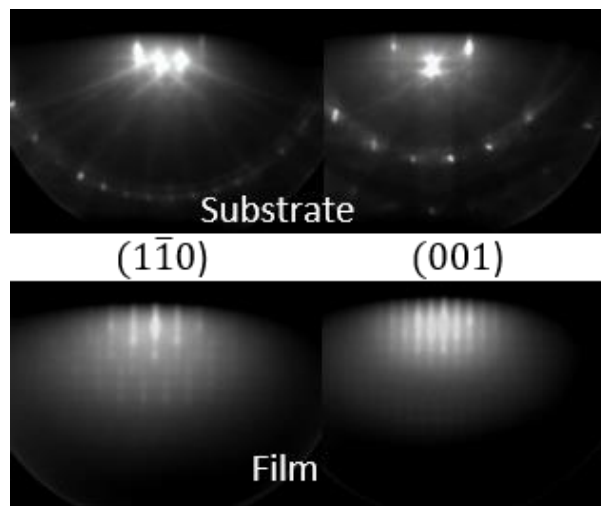
Figure 3.18: RHEED patterns along [1-10] and [001] (top) azimuth of substrate (top) and corresponding patterns from epitaxial film (bottom).
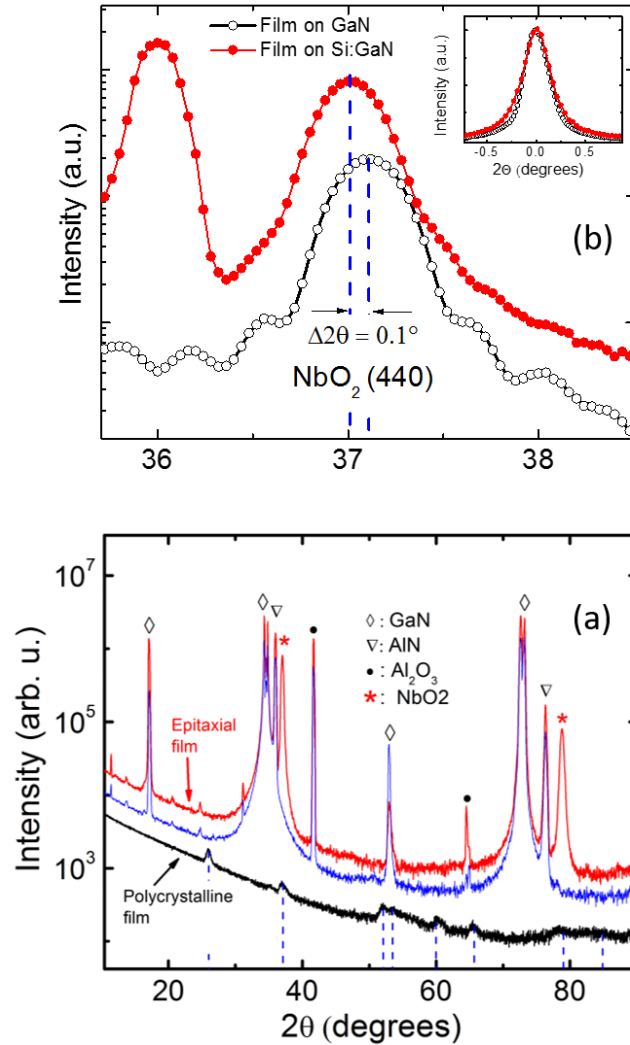
Figure 3.19: X-ray diffraction spectrum of NbO_2. (a) Epitaxial film (top red curve) grown on $GaN(0001)/AlN/Al_2O_3$ (0001) substrate (blue curve) and GIXRD spectrum of the polycrystalline film grown on $TiN/SiO_2/Si$ (bottom black curve) wafer. The vertical blue lines indicate the positions of the NbO_2 peaks from the PDF file. (b) Expanded view of NbO_2 $(440)_T$ peaks from two of the epitaxial films grown on undoped GaN (from Figure 3.10) and Si:GaN film [from Figure 3.19]. The dotted lines are peak positions. Inset figure shows corresponding rocking curves.

In case of GIXRD, the incidence angle was set to 1°. Polycrystalline peaks of NbO_2 were verified using powder diffraction file #00-043-1043.[94]

Figure 3.18 shows the RHEED patterns of the substrate along $(1\bar{1}0)$ and (001) azimuth and the films verifying epitaxial relationship of the film with the substrate. The film grown on doped GaN had a streaky pattern similar to the film grown on undoped GaN. Figure 3.19 shows θ-2θ scans of the 31 nm thick epitaxial film grown on GaN and GIXRD of the polycrystalline film grown on TiN coated wafers. The middle blue curve is the θ-2θ scan from a blank substrate. The substrate had additional AlN buffer layer, which was not present in the undoped GaN substrate, and therefore an additional peak of AlN (represented by '∇') is visible. The data indicate that the epitaxial film only had a (110)-orientation (represented by '*'), with all other peaks corresponding to the Al_2O_3 (•) and GaN (◊) layers of the substrate, as verified by a blank substrate scan [blue curve in Figure 3.19(a)].

Figure 3.19(b) shows the extended view of $NbO_2(440)_T$ peaks obtained from films grown on Si:GaN [Figure 3.19(a)] and intrinsic GaN (Figure 3.10). A peak shift in 2θ by 0.1° was observed. Intensity normalized rocking curves from the corresponding peaks is shown in the inset figure. The film grown on Si:GaN had a rocking curve with broadened peak width. The shift in peak position and broadening of rocking curve is probably a result of the increased disorder from the doping. Figure 3.20 shows the in-plane x-ray diffraction along (400) plane of the film and (113) plane of the $Al_2O_3(001)$, verifying the epitaxial relationship between film and substrate.

Figure 3.21 shows XRR data with corresponding AFM surface scans for both films. Fits of the XRR data using the GenX software[90] demonstrated that both films had identical film thickness (31 ± 0.8 nm) with identical roughness (0.8 ± 0.1 nm) within the measurement uncertainties. Corresponding AFM scans with the scan area of 500×500 nm^2 (Figure 3.21, insets)
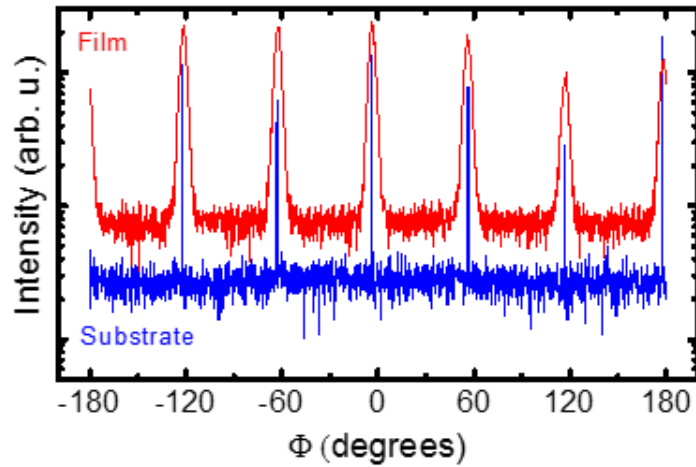
Figure 3.20: In-plane x-ray diffraction scan from (400) planes of film and (113) planes of the Al_2O_3 (001) substrate (right).
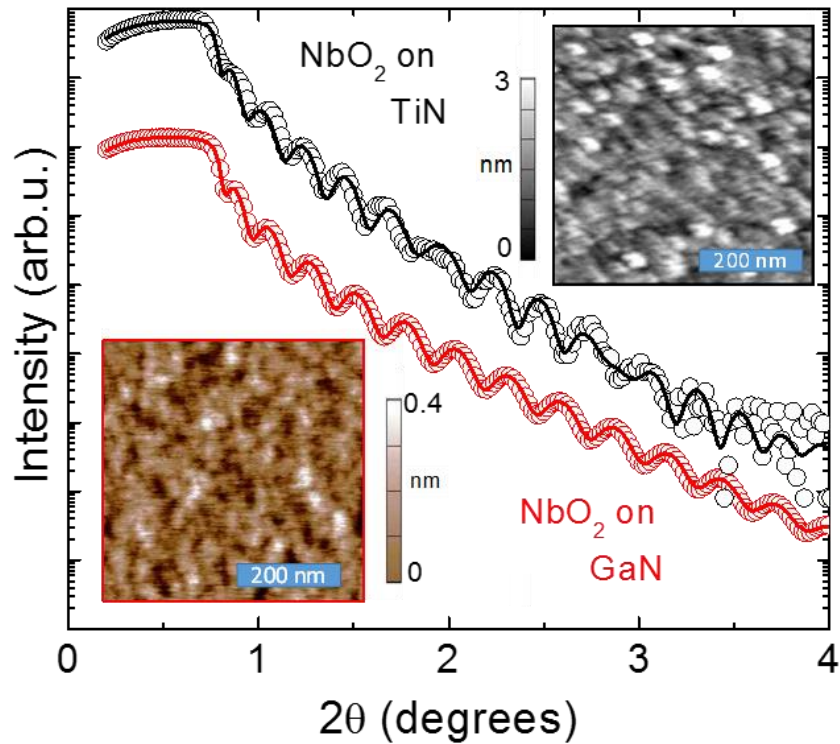
Figure 3.21: X-ray reflectivity of NbO_2 films with GenX fitting. Circular symbols represent raw data and solid curves represent the fits. Insets show corresponding AFM images of the surfaces of the films.
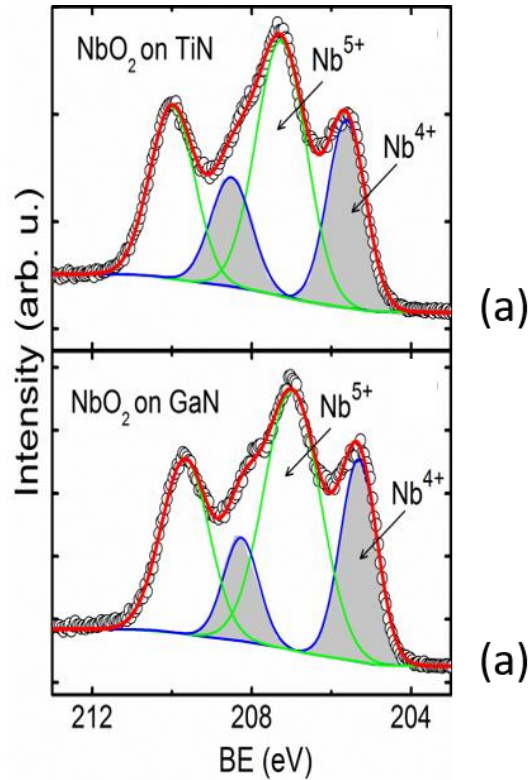
Figure 3.22: XPS data for Nb $d_{5/2}$ and Nb $d_{3/2}$ spectra of polycrystalline (a) and epitaxial (b) films with deconvoluted peak fitting. The shaded areas are the contributions from Nb^{4+} valency state.

demonstrated that the film surfaces were smooth with surface roughnesses of 0.4 and 0.2 nm, respectively. The discrepancy in roughness between XRR and AFM data can be explained by the difference in the active area proved during scans. For XRR, the area estimated from the beam width was > 1 mm^2.

The molar ratios of NbO_2 to Nb_2O_5 phases in polycrystalline and epitaxial films were estimated using Nb-edge 3d core level XPS spectra as shown in Figure 3.22(a) and (b), respectively. The peak fits using Gaussian line shapes showed approximately 34% NbO_2 and 66% Nb_2O_5 in each case. Peaks corresponding to Nb_2O_5 were not visible in XRD or GIXRD spectra in

Figure 3.19, which suggests that either the Nb_2O_5 top layer was amorphous or that its thickness was below the detection limit of XRD. It was not possible to determine the exact oxygen stoichiometry from these *ex-situ* measurements due to the possibility of the film surface oxidation after exposure to the air.

Thus, the films grown on Si:GaN and TiN coated substrates had the similar film thickness, surface roughness and film composition as verified by XRR, AFM, and XPS. However, film grown on Si:GaN was epitaxial while the film grown on TiN was polycrystalline as verified by x-ray diffraction (XRD).

CHAPTER 4

ELECTRICAL CHARACTERIZATION

In this chapter, the electrical properties of various type of NbO_2 thin films are investigated. From lateral devices constructed from epitaxial films grown on $Al_2O_3(001)$ substrate, the nature of threshold switching in NbO_2 (Joule heating) was demonstrated. Further in-depth investigation of polycrystalline thin film vertical devices was performed using thickness-dependent and contact-size-dependent current-voltage measurements. Finally, electrical properties of epitaxial and polycrystalline vertical devices were compared to investigate the effect of defect density on the electrical switching properties of NbO_2.

4.1. EPITAXIAL FILMS LATERAL DEVICES

In this section, transport measurements in epitaxial NbO_2 films grown on Al_2O_3 are presented. Because, Al_2O_3 substrate is an insulator, the measurements were performed with a current-in-plane geometry using top interdigitated electrodes (IDEs) so that no bottom electrode was needed, which eliminates the risk of jeopardizing the film quality.

4.1.1. Test Device Fabrication

An IDE structure patterned on the top of the film was used as two-terminal NbO_2 lateral devices as discussed in Section 2.7.1. Two of the pads (bright regions in Figure 2.6) were used as contact pads and electrical contacts were made using silver paste. IDEs were composed of a 50 nm Pt film grown via sputtering at room temperature and patterned via the standard photolithography

technique. The IDEs had 25 fingers from each side with a length of 500 μm and width and finger gaps of 5 μm each.

4.1.2. I-V Characteristics

Current vs. voltage (*I-V*) characteristics of NbO$_2$ lateral devices were measured with the electric field applied in-plane using IDEs. An input voltage sweep was applied as 0 → 12 V → 0 → -12 V → 0 with the scan rate of 0.2 V/s as discussed in experimental section (CHAPTER 2). *I-V* characteristics showed a typical threshold switching from high resistance to low resistance state as shown in Figure 4.1. This high resistance state refers to the insulating state while the low resistance state refers to the metallic state of the film. Thus, with the application of an electric field, the device switched from insulating to metallic, and went back to its initial state after removal of the electric field. This type of switching is called volatile switching. In the case of non-volatile switching (also called memristive switching), the device remains in low resistance state unless a negative pulse is applied to turn the device OFF.

Reversible MITs are mainly driven by a local heating effect which is discussed below in detail. The magnitude of threshold voltage (V$_{th}$) required to switch the device was found to be 10.8 V, which is equivalent to an electric field of E_{th} = 2.2 x 10^6 V/m. Typical threshold fields reported for vertical devices are on the order of 10^8 V/m.[5,7]

The film grown at 20 mTorr showed a different behavior (Figure 4.2), in agreement with its predominant Nb$_2$O$_5$ phase nature. This film had a much larger resistance than the NbO$_2$ films, so that an electric field greater than 34.6 x 10^6 V/m was needed to switch the initial low current state to a high current state. This state was retained to low current state even the electric field was removed, in agreement with the non-volatile switching characteristics. During the reversed cycle,
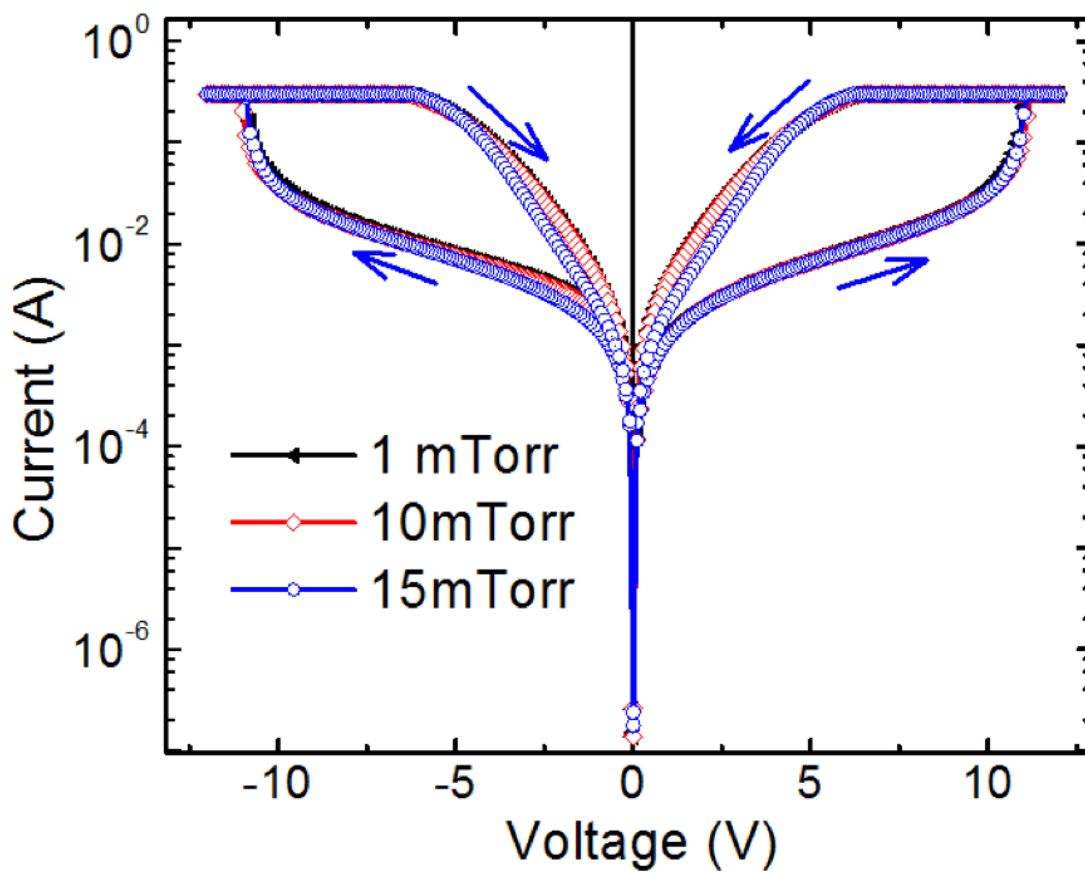
Figure 4.1: *I-V* characteristics measured on the film grown in 1 - 15 mTorr growth pressures. The flat regions in the current are due to compliance limits of 10^{-3} A. Blue arrows indicate the direction of voltage sweep.

a transition to further higher current state occurred, that is, the switching behavior was irreversible.

No Nb^{4+} valences were found in this film by the surface sensitive XPS technique (Figure 3.7). The most likely switching scenario for the film grown in 20 mTorr pressure involved oxygen migration
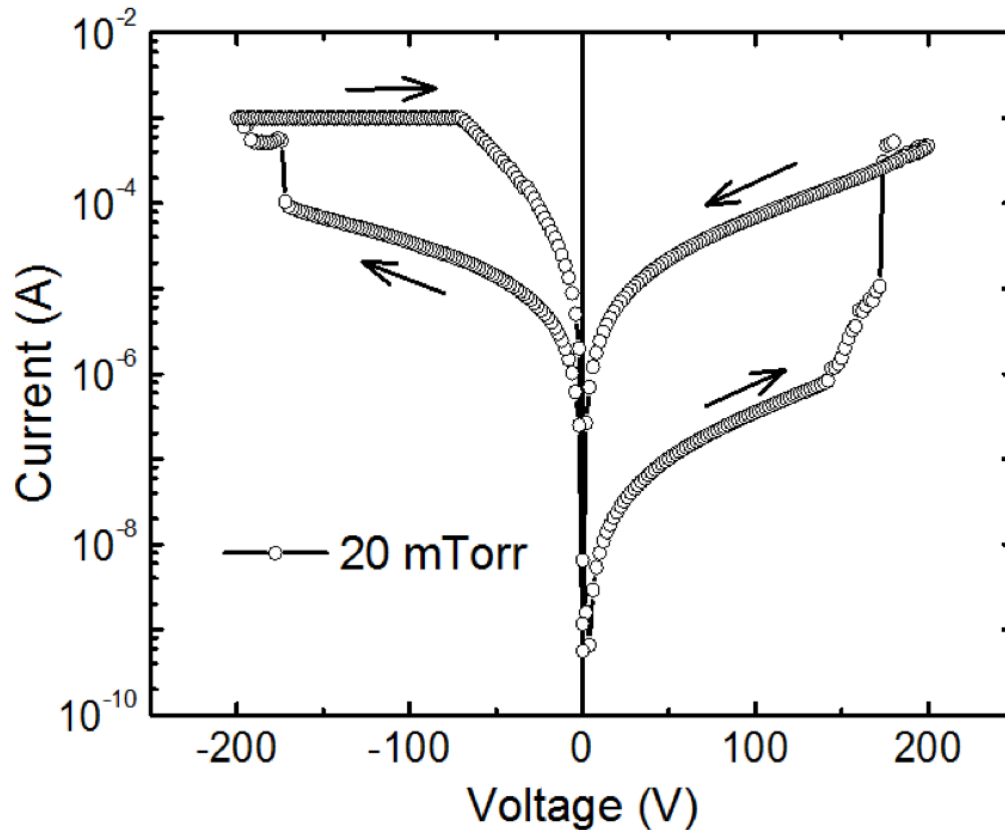
Figure 4.2: *I-V* characteristics measured on the film grown in 20 mTorr. The flat regions in the current are due to compliance limits of 10^{-3} A. Nb_2O_5 predominant phase was verified from XRD (Figure 3.2) and XPS (Figure 3.7).

and electroforming processes typical for Nb_2O_5 systems.[6] Also, the reduction of Nb_2O_5 to NbO_2

$[Nb_2O_5 \rightarrow 2NbO_2 + O^{2-}]$ may have increased the local temperature due to Joule heating, which

could have occurred during negative cycle, thus taking the dev2ice to a lower resistance state.

Figure 4.3 shows the corresponding variation of the temperature during the measurements

of *I-V* cycles on the NbO_2 film grown in 15 mTorr pressure. During switching, the local heat

dissipated by the film was absorbed by copper holder increasing the temperature of the block.
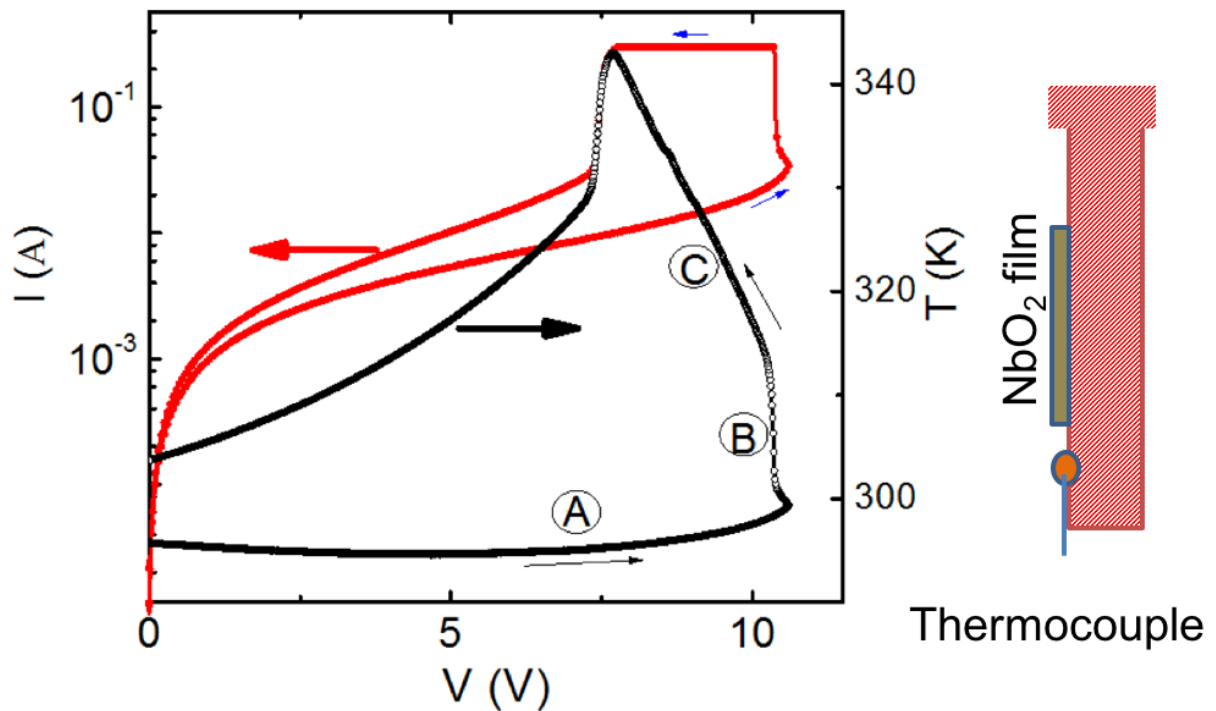
Figure 4.3: *I-V* curve (red filled circles) and the simultaneous temperature variation (black open circles) measured on the film grown in 15 mTorr. The flat regions in the current are due to compliance limits of 0.25 A. The diagram on the right shows the measurement scheme.

Therefore, the increase in temperature of the copper block became proportional to the current flowing into the device.

The temperature was read out by the thermocouple temperature sensor located on the copper block upon which the sample was mounted and in the close sample proximity (as shown in right part of Figure 4.3), so the temperature readings provided a remote measure of the dissipated power in the thin film. Three regions A, B, and C can be identified in the corresponding

temperature vs. voltage curve, related to the current flow while being in the high resistance state, to the increased current after the switching into the low resistance state, and to the temperature increase while the current remained constant (due to the instrumental compliance setting), respectively. The temperature in region B followed the abrupt increase in the current curve due to the Joule heating in NbO_2 thin films. A continuous decrease in temperature was observed until the voltage reached 5 V, most likely due to the Peltier effect at the metal-semiconductor junction. [118,119]

The temperature increase observed in Figure 4.3 cannot represent the real temperature in the film during the switching because the experimental geometry was not suitable to sense the local heating effect of the film. The maximum temperature of 343 K is rather indicative for the thermal gradient between the film and the attached copper block. Moreover, I estimate a relatively small fraction of the total film volume where MIT threshold switching takes place, therefore the average film temperature was likely below the MIT transition temperature for bulk NbO_2 (1083 K).

Negative differential resistance was observed during *I-V* measurement, where current increased as the applied voltage was decreased, as shown in region B of Figure 4.3. The negative differential resistance was clearly visible applying an input voltage greater than 8.5 V, as shown in Figure 4.3 (black, open circles). Negative differential resistance is also observed by applying a current limiting resistor in series with the device. The current vs. the voltage dropped across the device is plotted in the red curve with solid circles in Figure 4.4. The voltage dropped across the device was obtained by subtracting the voltage dropped across 50 Ω resistor. The magnitude of the slope of the *I-V* curve represents the resistance of the current filament, i.e. the resistance of the
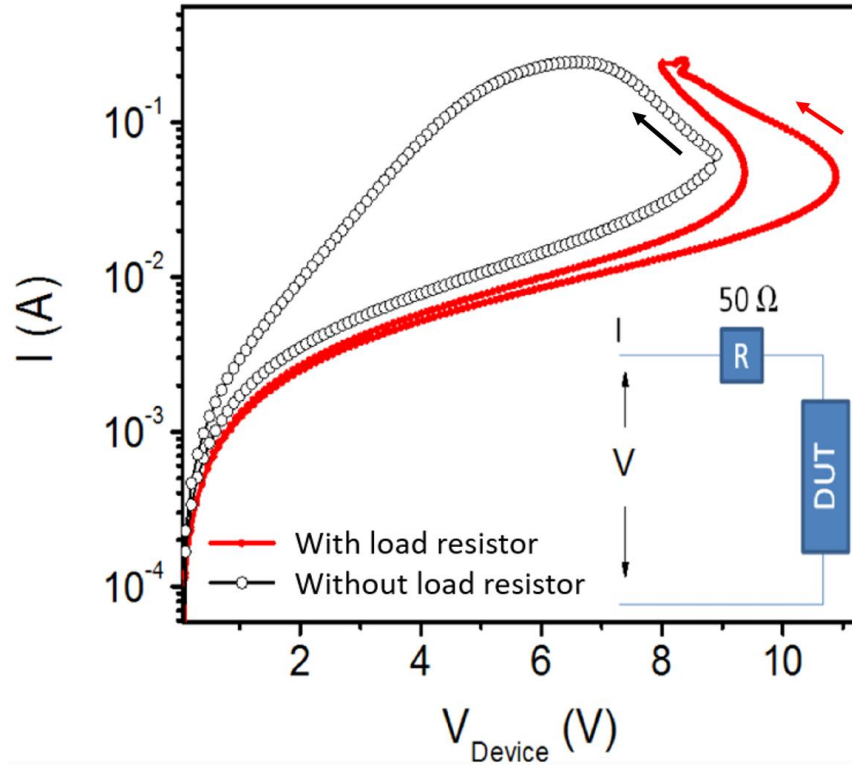
Figure 4.4: Negative differential resistance in a lateral device measured on the sample grown in 10 mTorr pressure. The black curve with open circle symbol was measured without using a load resistor of 50 Ω. Inset figure shows circuit connection diagram.

material while the device was at 'ON' state which was found to be approximately 10 Ω from Figure 4.4.

In contrast to the previous reports[3-7] where non-connected conducting filaments pre-existed and/or were modified by electroforming in non-stoichiometric and amorphous NbO_x phases, volatile and reversible switching were observed in the epitaxial quality NbO_2 films with minimal non-stoichiometry and with no electroforming steps required. Therefore, threshold switching in epitaxial lateral device followed conduction paths associated with defects, such as twin domain
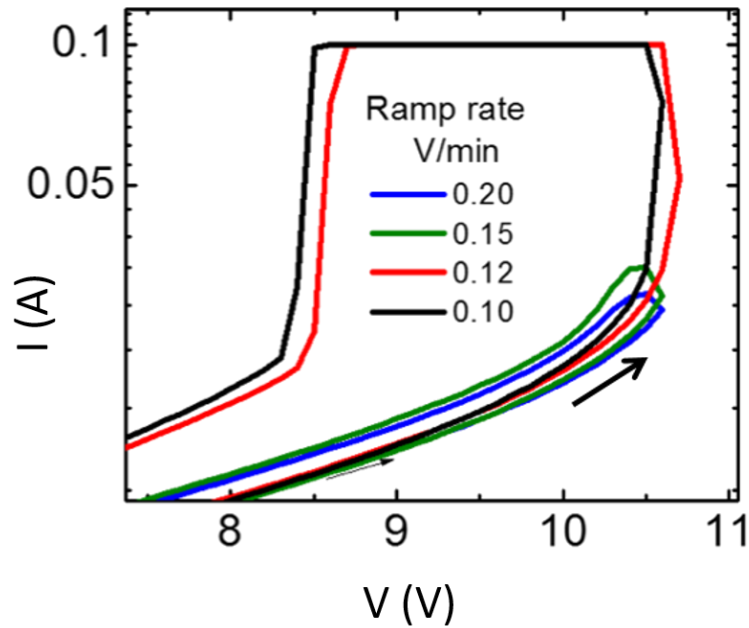
Figure 4.5: *I-V* curves measured using different ramp rate on the sample grown in 10 mTorr pressure. The slower the ramp rate, the larger the current becomes.

boundaries, in which thermally confined filaments were locally heated above the MIT temperature.[120-122]

Alternatively, filamentary paths in NbO_2 films could be confined at the interface with the surface Nb_2O_5 layer similar to Ref. 120. The recent study[123] on nanodevices made from NbO_2 has found no significant contribution to transport properties of NbO_2 films due to the presence of ~2 nm top surface insulating layer of Nb_2O_5.

Assuming that the current flowed through the entire NbO_2 film volume located between the top IDE fingers, the dissipation power per volume imparted at the threshold switching voltage of the *I-V* curves (Figure 4.1) can be estimated to be 1.3×10^{-4} nW/nm^3, which is much less than

the 5 nW/nm^3 reported for 20 nm thick and 60 nm in diameter electroformed NbO$_2$ channel vertically stacked between 110 x 110 nm^2 Pt contacts.[1,2] Despite certain differences in the film crystalline quality between those devices (e.g. density of defects), it appears as more likely that the discrepancy between power density ratios is due to the small fraction of the total volume of NbO$_2$ conducting channels (filaments) in our lateral devices, where the MIT triggered threshold switching takes place, similar to Refs. 1, 2 and 116.

Figure 4.5 shows the ramp rate dependent *I-V* characteristics measured on film grown in 10 mTorr pressure. The input voltage was ramped to 10.5 V with a ramp rate varying from 0.1 V/min to 0.2 V/min. The current at 10.5 V increased with decreasing ramp rate, leading the device toward its insulator-to-metal transition. This indicated that Joule heating produced by the applied electric field was playing an important role in switching, rather than applied electric field itself. Slower ramp rates provided longer time to heat the film above T$_{MIT}$.

4.1.3. Pulsed I-V Measurements

I-V measurements in the NbO$_2$ thin film devices showed that a slower ramp rate leads to an insulator-to-metal transition as discussed in Section 4.1.2. This indicated that heat produced by the current was the decisive factor for MIT rather than the applied electric field itself. This hypothesis was verified using pulsed *I-V* measurements described in this section.

The time dependence of the current switching was studied using triangular voltage pulses [Figure 4.6(b)]. The circuit is shown in Figure 4.6(a). A non-linear current response was observed [Figure 4.6(c)], corresponding to the threshold switching behavior for ramp times $\tau > 1$ ms. At the same time, the maximum current flowing at the half pulse period decreased with decreasing τ values, that is, faster voltage pulses induced a less non-linear current response. This suggests that
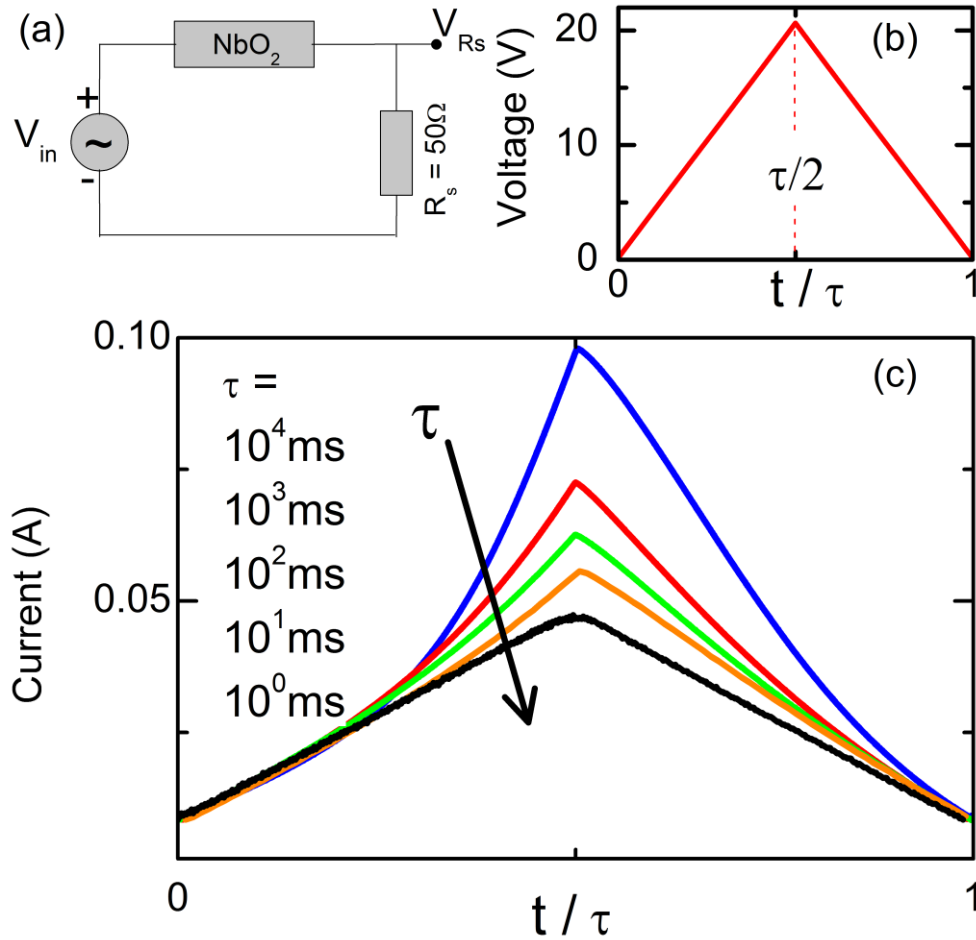
Figure 4.6: Pulsed *I-V* measurement: (a) Principal electric scheme of the pulsed-field measurements. (b) and (c) show applied voltage and measured current pulses vs time in relative units of time periods τ, respectively.

the nature of the threshold current switching in NbO_2 thin films was due to the Joule self-heating. With shorter pulses, the thin film material did not get enough time to heat the material up.

During *I-V* characteristics shown in Figure 4.1, an abrupt transition was not observed, which also agrees the thermally induced MIT with NbO_2. The threshold switching observed was much slower than the one reported in Ref. 2, where characteristic ON-OFF and OFF-ON times

were of the order of nanoseconds. The discrepancy, however, might be due to the larger gap between the electrodes (5 μm vs. 20 nm in Ref. 2) and the complexity of electric field lines in IDE electrodes vs. top and bottom Pt electrodes used in Ref. 2.

4.2. POLYCRYSTALLINE THIN FILMS VERTICAL DEVICES

In the previous chapter, device characterization of the epitaxial thin film lateral devices was demonstrated with the current measured in the lateral direction. Thermally induced insulator-to-metal transitions in NbO_2 were verified using lateral devices. More detailed studies of device switching, however, were not possible because of the complexity of the device structure, as discussed in the following paragraph, suggesting the importance of vertical devices in which current can be measured along vertical direction.

Lateral devices were composed of the IDEs with 25 fingers from each side. The length of each finger was 500 μm so that the total width (w) of the channel became approximately 24.5 mm. The leakage current observed below the threshold switching occurred was in the range of 10^{-2} A. This large leakage current was probably due to the large channel width (assuming uniform current distribution between the channel, $I \propto w$). Also, the device switching speed was very slow. As discussed in Section 4.1, non-linearity in output current characteristic disappeared for input pulse with pulse period below 10 ms (Figure 4.6). No current oscillations could be produced because of this slow current switching.

Previously reported NbO_2 thin film vertical devices were composed of amorphous NbO_2 films.[3-15,114-116] Amorphous film devices suffered from device instability due to the continuous change in crystal grain size upon using device multiple times.[124] Also, a high OFF-state leakage current, which reported to be greater than 10^{-5} A,[5,7,114-116] results in enhanced power dissipation.
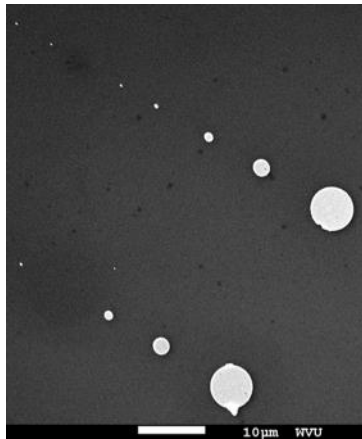
Figure 4.7: Top circular contact pattern with diameter ranging from 6.5 to 0.1 μm fabricated using e-beam lithography technique and depositing 50 nm Pt on the top of the film.

In this section, a detailed investigation of electrical properties of NbO_2 polycrystalline thin films grown on TiN coated SiO_2/Si substrates are reported in which the type of defect density presented in the film and its correlation with switching mechanism is investigated.

4.2.1. Test Device Fabrication

The current-voltage (*I-V*) characteristics were measured using probe station tungsten tips (Picoprobe) from GGB Industries Inc., as top contacts pressed directly on top of the film, to prevent the contact material from melting and diffusing into the film. The nominal size of the probe station tip used was ~2 μm. For contact-size dependent conductivity measurements, top Pt contacts were sputtered in form of circles with the thickness of 50 nm and diameters ranging from 6.5 to 0.1 μm, using the e-beam lithography technique, as discussed in experimental section. The contact patterns with varying diameter are shown in Figure 4.7.

The voltage was applied across the thin film at ramp rates of 0.1 V/sec and the output current was measured using a Keithley 2400 multimeter. For pulsed *I-V* measurements, short triangular ramp pulses were applied to the sample and the output was measured with a resistor R_s = 51 Ω connected in series using Tektronix 224 digital oscilloscope. Contact size dependent *I-V* measurements were performed at the voltage loop frequency of 1 Hz, using an atomic force microscopy setup from Asylum equipped with conducting Pt-coated Si cantilever tips.
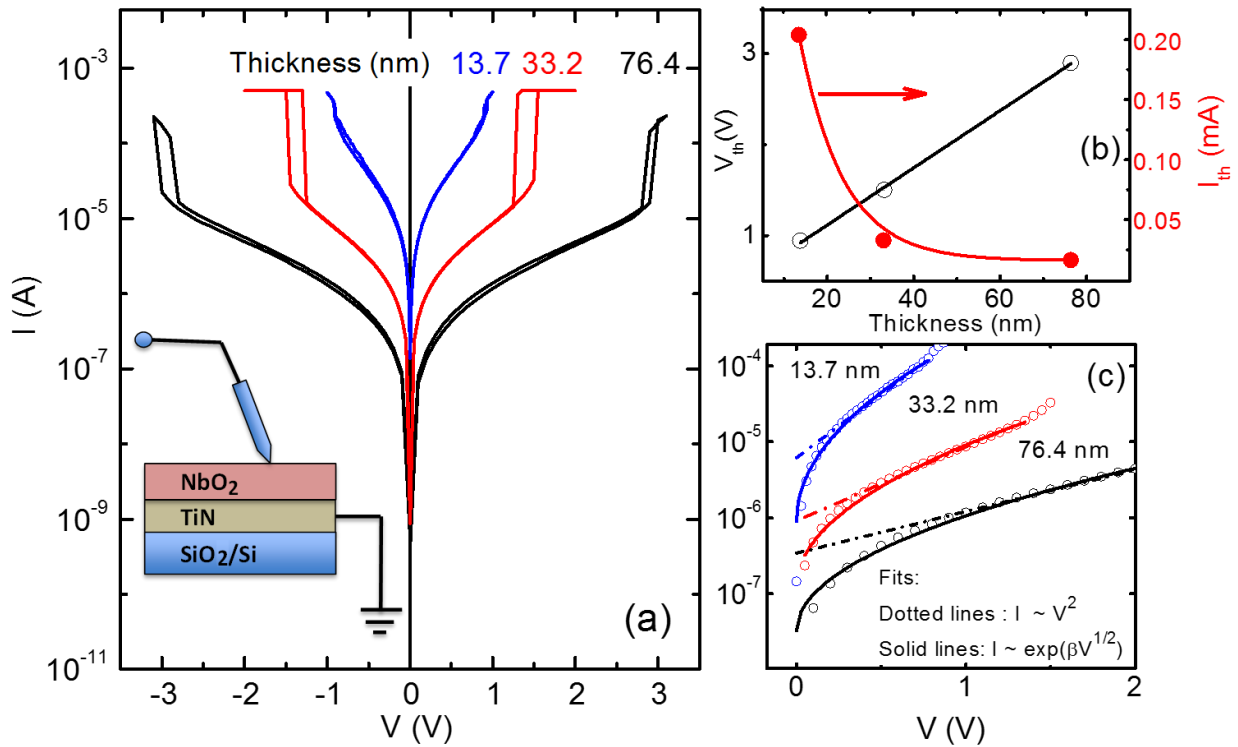
Figure 4.8: (a) *I-V* curves measured using probe station tip at room temperature in air for the film of different thicknesses. Schematics of sample structure and measurement plan is shown in inset figure. (b) threshold current and voltage plotted against film thickness, (c) enlarged view of *I-V* curves from Figure a [symbols] with fits using space-charge-limited (dotted lines) and Poole-Frankel conduction model (solid lines)].

4.2.2. I-V Characteristics

Figure 4.8 shows the *I-V* characteristics measured on three of NbO_2 films with film thicknesses of 13.7, 33.2 and 76.4 nm, using the probe station tip as a top and TiN layers as a bottom contacts, respectively, as shown in Figure 4.8 (inset). The films were grown in 10 mTorr total Ar+O_2 pressure. A clear threshold switching in current characteristics was observed and the threshold switching voltage (V_{th}) depended linearly on the film thickness, as shown in Figure 4.8(b). The linear dependence of V_{th} indicated that the ratio between the threshold voltage and the thickness, i.e. the threshold electric field, was constant and therefore that the bulk portion of the film was playing the main role in the switching, rather than the metal-oxide interface. This contrasts with some other materials, for example Fe_2O_3,[125] which have a resistive switching behavior that is independent of the film thickness because of the metal-oxide interface participating in the switching. The current measured at the threshold voltage, on the other hand, showed an exponential dependence on the film thickness [Figure 4.8(b)]. An exponential dependence of current was also reported in case of some binary and complex oxides.[126] In thinner films, defects at the film-substrate interface contribute more to the conductivity. The diffusion of N- or Ti-atoms from substrate into the film might also be responsible for the increased current conductivity of the film. A detailed study of interfacial chemical reaction, however, has not been reported.

I-V curves in the exponential region are fitted to space-charge-limited (dotted lines) and Poole-Frankel conduction mechanism (solid lines) as shown in Figure 4.8(c). In the low voltage region, the exponential dependence model, $I \sim \exp(\beta V^{1/2})$, fits well, indicating that the conduction in insulating state is due to the trap-assisted Poole-Frenkel (PF) effect.[24,127] Poole-Frankel conduction is based on the field-assisted thermal emission of carriers from Coulombic trap centers.[128] Constant β used in PF-equation varies as $\varepsilon^{-1/2}$, ε being the dielectric constant of the

material. The values of β obtained from the fittings are 5.53, 4.31 and 3.49 for the films with thicknesses 13.7, 33.2 and 76.4 nm, respectively. The increase in value of β, i.e. the decrease in ε, with decreasing thickness was due to the increased disorder induced traps near film-substrate interface as discussed above.

Contact size dependent *I-V* characteristics were further investigated for the NbO(10) thin film sample (see Table 2) using conducting probe AFM. The current compliance was set to 10^{-5} A. *I-V* curves obtained for top contact diameters from 6.5 to 0.1 μm are shown in Figure 4.9(a) with corresponding current density vs applied electric field plotted in Figure 4.9(b). The current flowing through the NbO_2 film device showed contact size dependence, the so-called homogeneous type transition of current distribution.[125,129,130] Sim et al. observed similar behavior in case of Nb:$SrTiO_3$ resistive switching.[123] This phenomenon could be described as the production of multiple parallel current filaments homogenously across the entire area of the contact.[123] As discussed in several reports,[2,128] current filaments are defined as conducting channels produced by chemical defects or structural phase transitions produced by the heating effect of the current.

This indicated that the film conductivity in the insulating state depended on the entire area of the contact rather than the local current pathways. Current measured at different bias voltage showed contact size dependence as shown in Figure 4.10(a) as discussed below. Amorphous NbO_2 thin films[114] as well as some other resistive switching devices have shown inhomogeneity, in which conductivity of the device depends on local filamentary pathways[131] and the current flowing into the device is independent of contact area. In Ref. 114, Cha et al. used 20 nm amorphous NbO_2 thin film with TiN contacts. The threshold switching voltage measured using contacts with contact size ranging from 10 to 150 nm remained constant.[114]
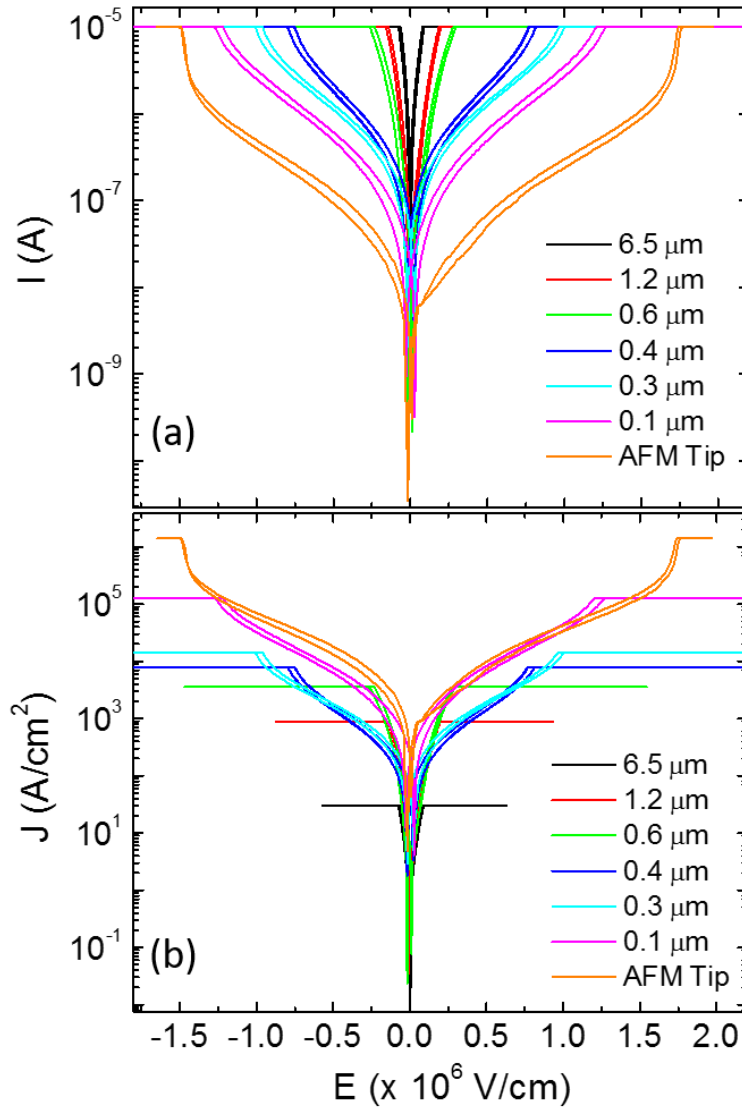
Figure 4.9: *I-V* curves measured using conducting probe AFM at room temperature in air for NbO(10) using different electrode sizes. (a) Current vs. applied electric field and (b) Current density vs. applied electric field.

Similarly, Wang et al.[113] have reported an increase in threshold voltage with increased contact size in NbO_2 polycrystalline film, which is the opposite of my result. They used rectangular shaped Nb top-contacts with contact sizes varying from 30 µm × 50 µm to 130 µm × 150 µm

where threshold field increased from 60 kV/cm to 90 kV/cm, respectively.[113] The lateral dimension and geometry of the device used by Wang et al. were very different in comparison to devices used in this work. The exact mechanism of area dependence is not clearly explained by the authors.

My case can be explained by the fact that the current carriers presented in the films, basically the trap centers induced by oxygen vacancies or grain boundary defects,[120] are distributed uniformly throughout the film. An application of electric field provides multiple parallel current pathways through the device yielding contact size dependence of the current. It is hard to assure that the devices follow contact size dependence after the switching because the devices with larger contacts did not have a complete switching because of the current compliance of the instrument which was limited to 10^{-5} A. The current characteristic of the device with smaller contacts (e.g., AFM Tip), however, clearly followed the current characteristic after the switching.

Leakage currents measured at different regions of *I-V* curves [from Figure 4.9] are shown in Figure 4.10 which indicated that the current densities measured from the contacts with size below and above 0.6 µm in diameter (A ~ 10^{-9} cm^2, indicated by the dotted line) behaved differently. For contact sizes below 0.6 µm, the area dependence of the leakage current with increased bias voltage remained in parallel in the log-log graph. Leakage current for current size above 6 µm, however, were not parallel.

Insulating state leakage current values, *I*, and current densities *J* measured at $V = 0.3$ V vs. contact area *A* are shown in the Figure 4.10(b). The data fits well on a log-log scale with two power law segments, $\ln(I) = n \ln(A)$. For larger area contacts with $A > 2.8 \times 10^{-9}$ cm^2, $n_1 = 0.82 \pm 0.06$, or $I \sim d^2$, whereas for smaller area contacts with $A \leq 2.8 \times 10^{-9}$ cm^2, $n_2 = 0.55 \pm 0.02$, or I ~ d. Thus, below the critical area of A = 2.8×10^{-9} cm^2, the current varies with the diameter rather than the area of the contact.
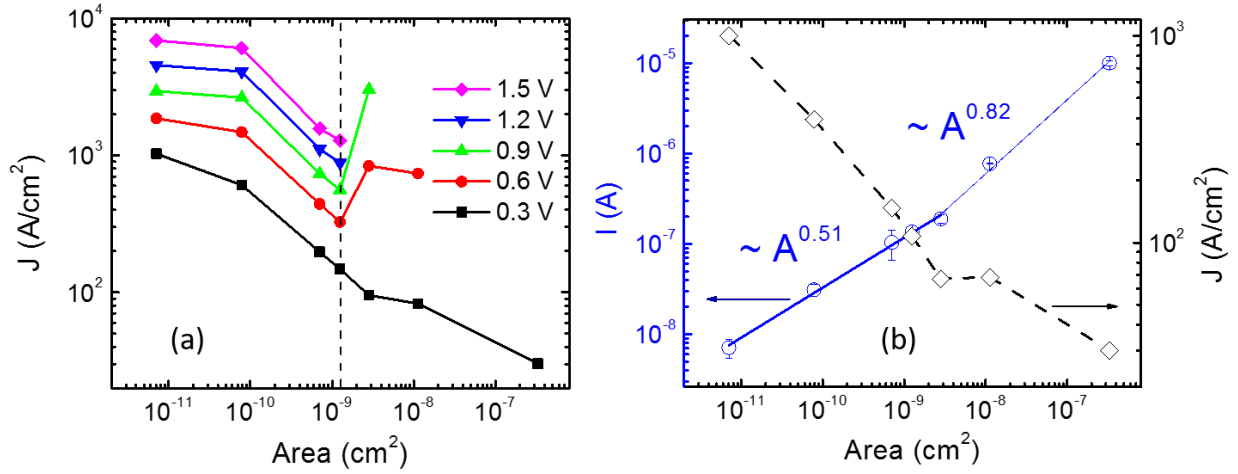
Figure 4.10: Contact size dependent leakage current. (a) Leakage current vs. top contact area measured at different regions of *I-V* curves of Figure 4.9. (b) Leakage current and current density vs. contact area measured at 0.3 V.
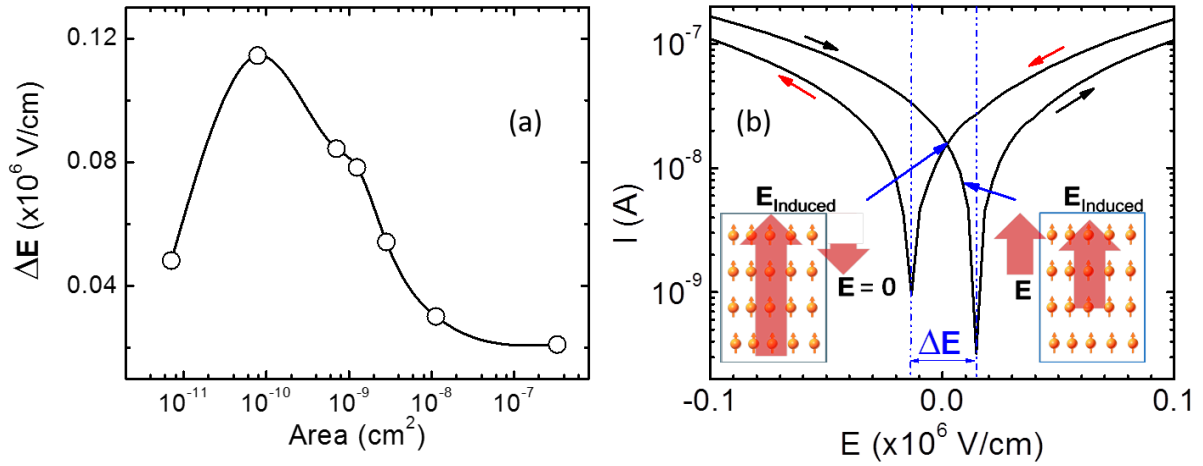
Figure 4.11: (a) Separation between two minima (Δ*E*) calculated from the contact size dependent *I-V* (Figure 4.9). (b) Zoomed part of the *I-V*-curve near E = 0 for contact size 0.1 µm showing two current minima at E ≠ 0.

This unusual dependence of the critical current on diameter could be explained in terms of an induced current produced by the film material due to dipole relaxation as demonstrated in Ref. 135. The effect of induced electric field is larger for smaller contacts, as explained in the next paragraph. As discussed by Prakash et al. in Ref. 136, the bigger contacts include larger number of grains and thus larger number of grain boundary defects yielding larger leakage current. Consequently, larger contacts had the smaller effect of induced field in *I-V* measurement due to the faster dipole relaxation facilitated by larger leakage current.

All of the contact size dependent *I-V* curves had minima near $E = 0$, as shown in Figure 4.11(b), due to the induced field from the thin film material. At $E = 0$, $I_{measured} = I_{induced}$, where $I_{induced}$ is the current induced by dipole field. Per Wang et al., under small applied voltage, O-atoms cannot migrate completely inside the film but slightly shift from the equilibrium position forming dipoles.[135] When the applied field is sufficiently small, $I_{induced}$ has predominant effect in current characteristics. Effect of $I_{induced}$ also depends on dipole relaxation (or, current decay) time which is proportional to the separation between of two minima (ΔE) as shown in Figure 4.11(b) because faster the relaxation, closer the minima will be. Figure 4.11(a) indicated that $I_{induced}$ had larger effect for the smaller contacts except the smallest contact that had a complete switching.

In any case, the dependence of current on contact size has an extreme importance. In current Si technology, FinFET device, for example, reduction in device dimension results in increased leakage current due to the quantum tunneling of the electrons between the gates. In the case of the NbO_2 device, however, lowering the device dimension not only helps to increase the device density but also helps to lower the leakage current. Using the smallest contact size (i.e., AFM tip), the leakage current measured at V_{th} was $I_{th} \sim 10^{-6}$ A which is an order lower in magnitude reported so far.[5,30,114,115]
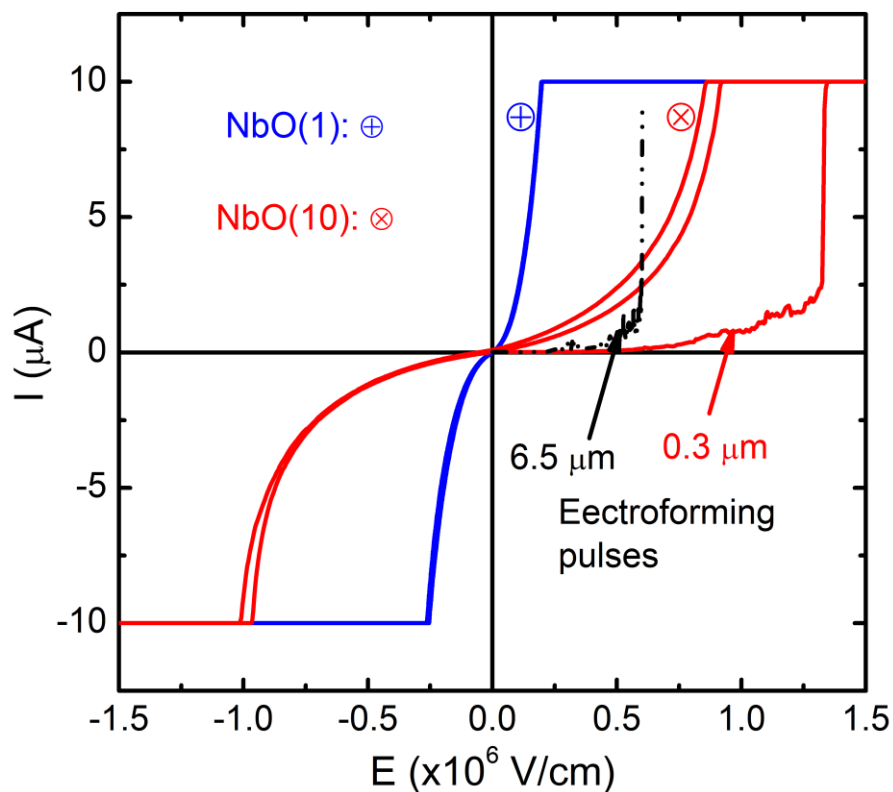
Figure 4.12: *I-V* curves measured using 0.3 µm contact size from sample NbO(1) and NbO(10). NbO(1) has higher leakage current in comparison to the sample NbO(10). Forming pulses are also shown for 6.5 and 0.3 um contact sizes of NbO(10) film.

I-V characteristics measured on two films NbO(1) and NbO(10) are plotted in Figure 4.12 using the same top contact size with a diameter of 0.3 µm. The films were grown in 1 mTorr and 10 mTorr total growth pressures, respectively. The film NbO(1) grown in lower total pressure had current values an order of magnitude higher than those measured on the NbO(10) film. Increased trap density enhanced by increased number of defects (oxygen vacancies) was mainly responsible for higher leakage current in the film grown in lower oxygen pressure. A partial overlap of Coulomb potential wells with increased trap density helps to lower the barrier height, thus

increasing the conductivity.[2,125,135,137] The bulk portion of the film might contain conducting NbO

phase or excess metallic Nb which might also contribute to the larger leakage current. It is not

possible to estimate bulk film stoichiometry using *ex-situ* XPS measurement because of the surface

sensitivity of XPS. NbO or metallic Nb on the surface of the film can be oxidized to NbO_2 or

Nb_2O_5 upon exposure to the atmospheric oxygen.

Prior to observing a threshold switching, a forming pulse with a voltage larger than those

used during normal operation was required. It is believed that during an electroforming step,

accumulation of defects, such as oxygen vacancies or excess niobium atoms, or migration of O-

atoms takes place creating a conductive path for the current. Forming pulses for 0.3 and 6.5 μm

(dotted curve) contacts are shown in Figure 4.12.

The mechanism of the electroforming process in single crystalline or polycrystalline NbO_2

films is not fully understood yet. In case of amorphous films, it has been suggested that a formation

of conducting filamentary channels of crystalline NbO_2 takes place through the film during the

electroforming, where increased temperature by Joule heating assists with a local crystallization

of the film material.[5,124] However, a variety of phenomena, like migration of oxygen vacancies or

excessive oxygen atoms, as well as dissociation or re-incorporation of oxygen atoms within NbO_2,

is possible. Since these measurements were performed in ambient atmosphere, an additional post-

oxidation of Nb might have also been taken place.

To explore the conduction mechanism in pristine state, *I-V* curves were fitted to Poole-

Frenkel (PF) equation,[138]

$$I = I_0 \exp(\beta V^{1/2}) \tag{23}$$

where, $\beta(T) \sim (\mathcal{E}T^2)^{-1/2}$ is the function of temperature (T) and $\mathcal{E}$ is the dielectric constant of the

material. Here, I assumed that *T* remained fairly constant for low bias voltages *V*. Figure 4.13
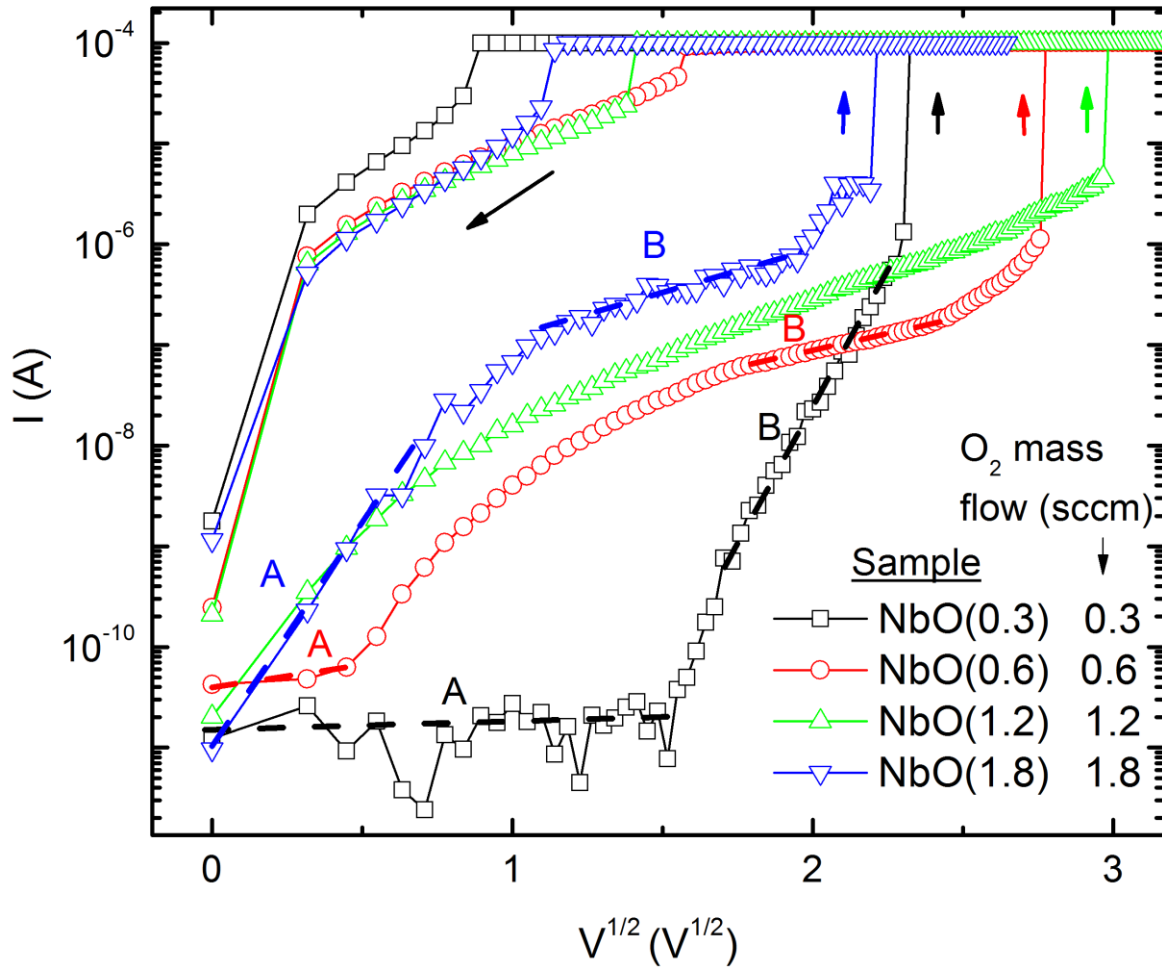
Figure 4.13: Forming pulses measured from the films grown using various O_2 concentration fitted to P-F equation (Eq. 22). Arrows show the direction of *V*-sweep. Different values of β were obtained for different regions of IV curves.

shows the current in logarithmic scale vs $V^{1/2}$ for four of the films represented by symbols NbO(0.3), NbO(0.6), NbO(1.2) and NbO(1.8) grown with different oxygen concentrations as listed in Table 2. The majority of current carriers in the most oxygen deficient film [NbO(0.3)] were expected to be oxygen vacancies. For the oxygen rich film [NbO(1.8)], the majority carriers were expected to be migrating O^{2-} ions, as well as the grain boundary defects between NbO_2 and Nb_2O_5

crystal domains. The term β from PF equation, $ln(I/I_0) = \beta\ V^{1/2}$ was estimated for forming pulses in the pristine state.

For oxygen deficient film [NbO(0.3)], β is small (0.36 $V^{-1/2}$) in region A as shown in Figure 4.13 indicating a larger dielectric constant in comparison to the dielectric constant of the other films in the similar region. This could be explained in terms of oxygen vacancies in the films. Before application of the electric field, vacancies were uniformly distributed. Therefore, I remained flat until $V^{1/2}$ reached 1.5 $V^{1/2}$. With increasing electric field, accumulation of vacancies near the electrode took place with a sharp increase in β (therefore, I) in region B. Oxygen-rich films, on the other hand, had the opposite behavior. Migrating oxygen atoms and/or localized grain boundary defects provided an immediate increase in current after application of electric field (region A). Current started to flatten after $V^{1/2}$ reached 1 $V^{1/2}$ (region B). Migration of excess oxygen in the form of O^{2-} ions resulted in insulating Nb_2O_5 near the electrodes, consequently lowering the current flow. Application of sufficiently large electric field causes dielectric breakdown or tunneling through the insulating layer, resulting in a MIT.

Film NbO(0.6) showed intermediate behavior with an initial constant current region (Region A) similar to the film NbO(0.3) and current flattening above 1.5 $V^{1/2}$ (Region B) similar to NbO(1.8) film. NbO(1.2), on the other hand, behaved in similar way to the NbO(1.8) film. This indicated a gradual transformation in the film quality from a vacancy rich to an oxygen rich film, as expected, while increasing oxygen mass flow from 0.3 to 1.8 sccm.

4.2.3. Pulsed I-V Measurements

Figure 4.14(a) shows a circuit diagram for pulsed *I-V* measurements. Triangular voltage pulses with different pulse widths (τ) were applied across the films and the output current was measured across a test resistor R_s. A non-linear current switching characteristic was observed for
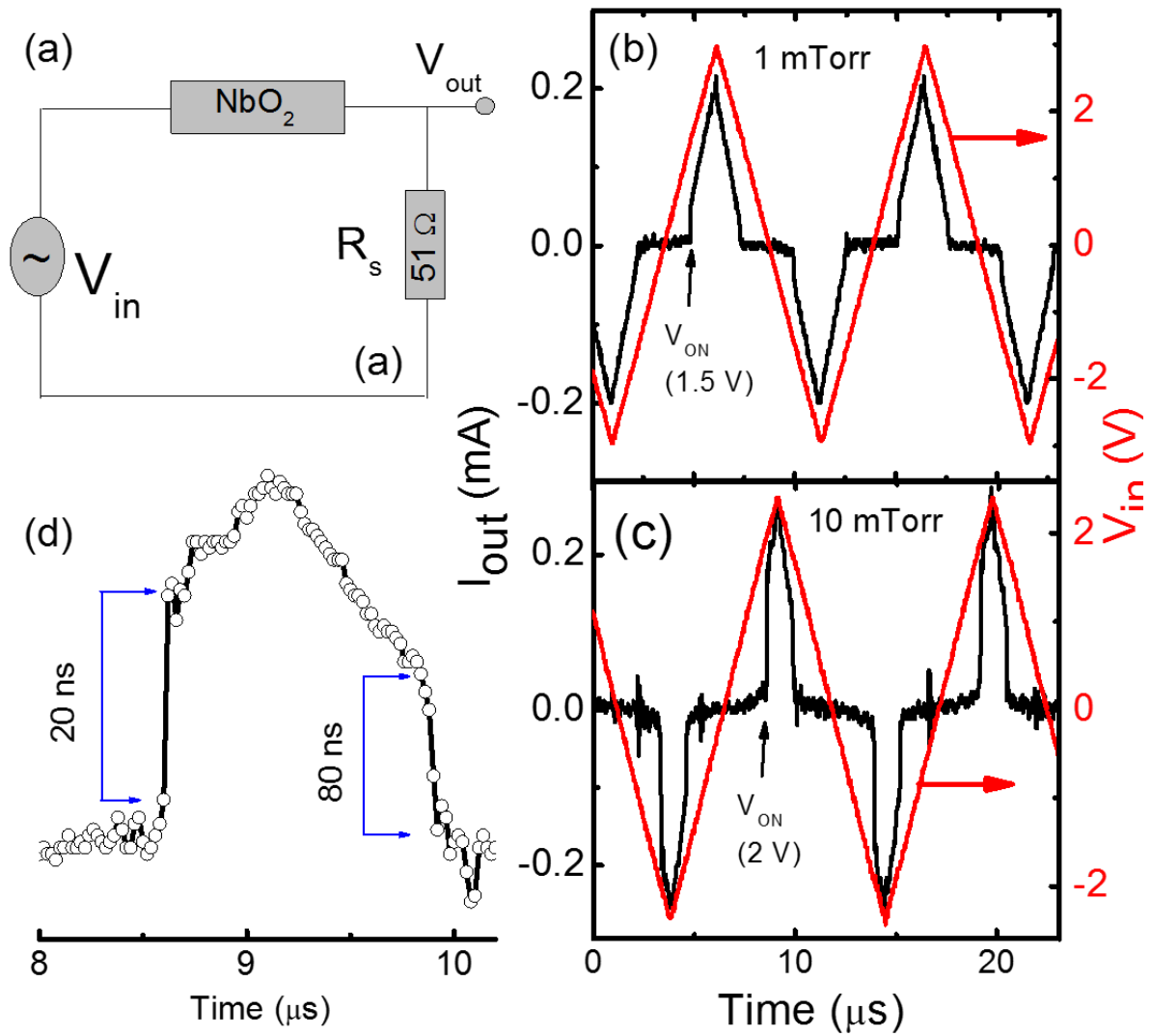
Figure 4.14: Pulsed *I-V* measurement (a) Circuit diagram for pulsed *I-V* measurement. (b), (c) Pulsed input (right scale) and output current characteristics obtained from NbO(1) and NbO(10) films, respectively. (d) a zoomed part of Fig. c showing current switching time of 20 ns while turning 'ON' and 80 ns while turning 'OFF'.

pulse width values $\tau \leq 10$ μs. Output pulses for films NbO(1) and NbO(10) for $\tau/2 \leq 5$ μs are plotted in Figure 4.14(b) and (c), for comparison. The device from NbO(1) film had a turn-on voltage (V_{ON}) of 1.5 V which was smaller than the $V_{ON} = 2$ V of the NbO(10) film device. As discussed previously, the film NbO(1) had a higher defect density because it was grown in lower chamber pressure. Also, the NbO(10) device had sharp switching with narrower output pulse width. A zoomed view of output current pulse, from the film NbO(10) growth pressure, is shown in Figure 4.14(d). The typical ON switching time was found to be $\tau_{ON} \sim 20$ ns while the OFF switching time was $\tau_{OFF} \sim 80$ ns, which is fast enough for a current selection element in any RRAM device.[129] τ_{OFF} was approximately 4 times slower than corresponding ON time, due to the existence of longer thermal relaxation time while lowering electric field.[2] ON/OFF times for the NbO(1) device were found to be approximately 5 times slower than the film NbO(10). The device from the film grown in 10 mTorr pressure provide better performance while used in practical current switching element.

4.2.4. Self-sustained Current Oscillations

Figure 4.15(a) shows the connection diagram with the NbO_2 film as connected in series to a load resistor (R_L) of 10 kΩ and a sense resistor (R_S) of 51 Ω, the latter used for current measurements. The sample is shown as a switchable resistor connected to a parallel capacitor, representing the intrinsic capacitance of the insulating (OFF) state. A low frequency input voltage (V_{in}) with a triangular or a rectangular wave shape was applied and the output signal (i.e. current, I_{out}) was measured across R_S. Figure 4.15(b) shows a current response after a triangular voltage pulse was applied. Current oscillations were observed only within a certain range of the input voltage V_{in} [red, dotted line in zoomed view], starting when $V_{in} = 2$ V and lasted until the input voltage $V_{in} = 5$ V was reached.
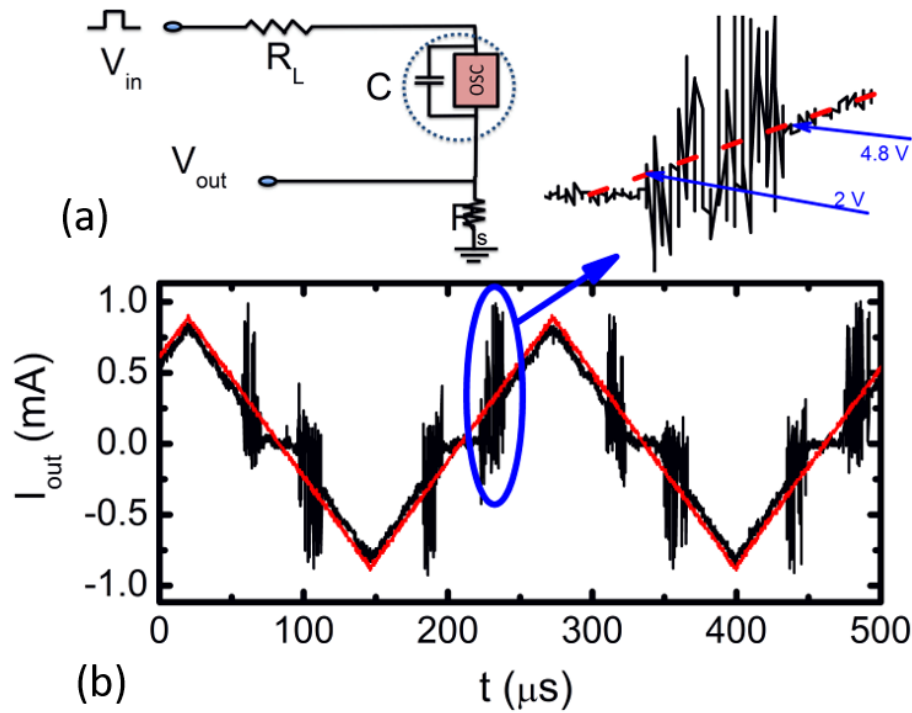
Figure 4.15: Schematic diagram for a current oscillator (a) and current oscillations with a triangular pulse field (b). Zoomed figure showed that the range of input voltage contributing for oscillation was 2 V to 4.8 V.

Figure 4.16 shows the oscillation patterns obtained from films NbO(10) [Figure 4.16(a)] and NbO(1) [Figure 4.16(b)]. An application of input rectangular pulse field of 7.4 and 4.4 V produced oscillations with frequencies 18 and 12 MHz from the films NbO(10) and NbO(1), respectively. The closer views of oscillations are shown in the inset figures. Aside from the main frequency oscillations, other secondary oscillations were present.

Before application of V_{in}, NbO$_2$ device was in its initial high resistance state. The associated capacitor became charged when the field V_{in} was applied. Increasing the current flowing through the film caused it to switch to the low resistance state, resulting in the capacitor beginning to
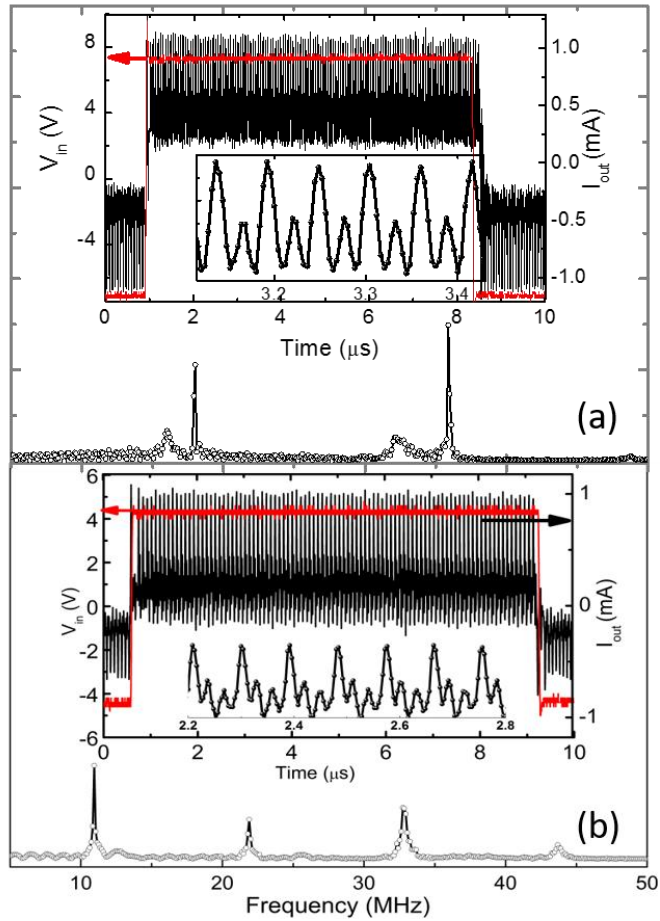
Figure 4.16: Self-sustained current oscillations measured from films (a) NbO(10) grown in 10 mTorr pressure and (b) NbO(1) grown in 1 mTorr pressure. Fast Fourier Transform (FFT) are shown at the bottom of each showing frequency components. Also, insets show the zoomed views of oscillations.

discharge. During this step, the largest voltage V_{in} drop occurred across R_L, and so the film turned itself insulating when the voltage was reduced. A rapid repetition of the process provided large frequency oscillations to output circuit.[116,133,139]

Time dependent oscillations performed with NbO(1) showed that oscillations lasted over 48 hours (10^{12} cycles) with 5% fluctuation in frequency and 33% fluctuation in amplitude which
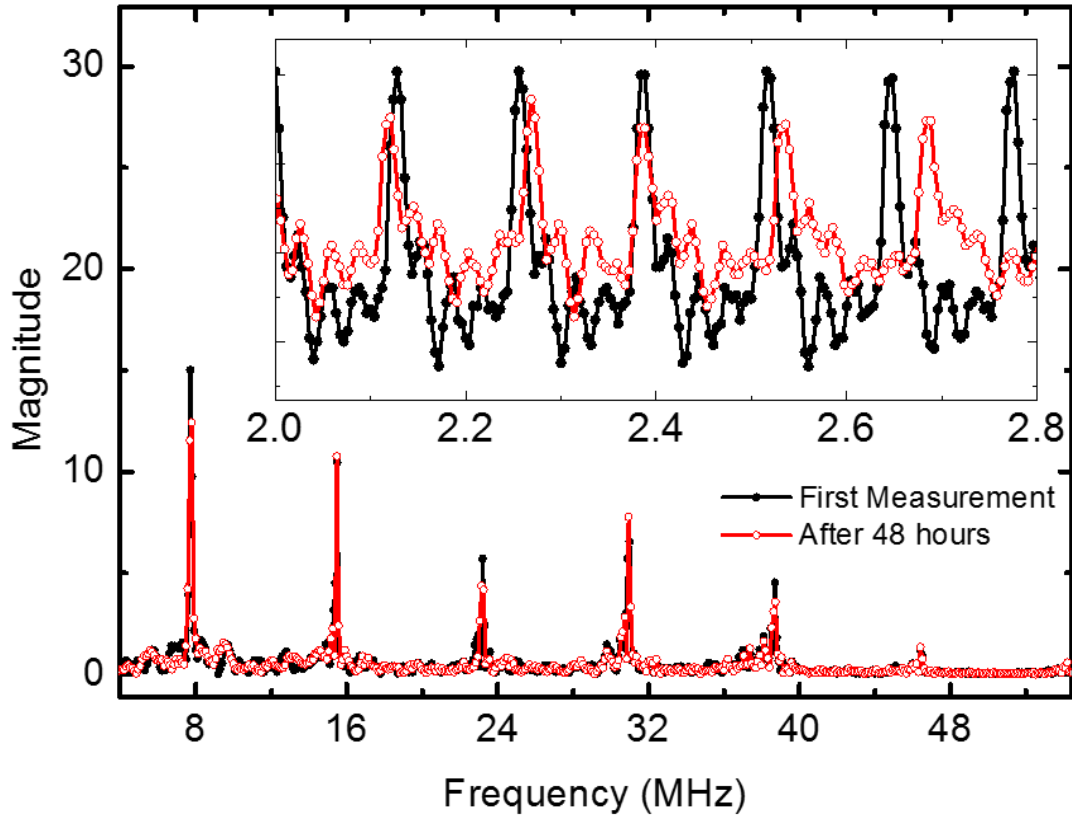
Figure 4.17: Oscillations measured from the NbO(1) film at t = 0 (black, solid circles) and t = 48 hrs (red, open circles). The main figures show FFT and inset shows the oscillation patterns.

was the most stable oscillator so far reported. The oscillations measured at t = 0 (black solid symbols) and t = 48 hrs (red with open symbols) are shown in Figure 4.17 with corresponding FFTs. The peak-to-peak amplitude (I_{pp}) of current oscillations was about 1.1 mA, which are the largest oscillations by amplitude observed so far.

Input voltage vs. frequency determined for all films listed in Table 2 are plotted in Figure 4.18. For the film grown in 1 mTorr, the range of V_{in} where self-sustained oscillations were
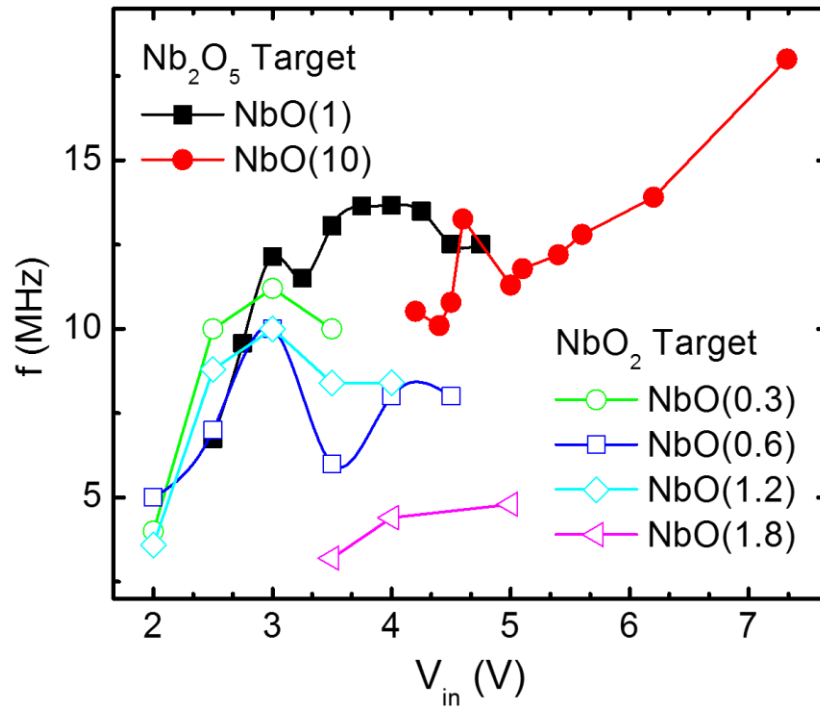
Figure 4.18: Input V versus f of films NbO(1) and NbO(10) (solid symbols) and NbO(0.3) to NbO(1.8) films (open symbols).

observed was found between 2.5 V to 4.8 V, in agreement with the study on the same film under triangular pulse application [Figure 4.15(b)]. The oscillation frequency f_{osc} increased with increasing input voltage amplitude V_{in} until $V_{in} = 4$ V. Upon further increase of V_{in}, f_{osc} started to decrease and oscillations disappeared. Lalevic et al.[130] in 1980 have reported a similar trend in frequency variation: linear increment followed by a saturated region using polycrystalline thin film devices.

Film NbO(10) did not have a clear peak frequency behavior, and the range of V_{in} resulting in stable oscillations was located at higher values, between 4 to 7.5 V, in comparison to the film NbO(1). Because of the lower defects presented in the film, the film grown in 10 mTorr pressure
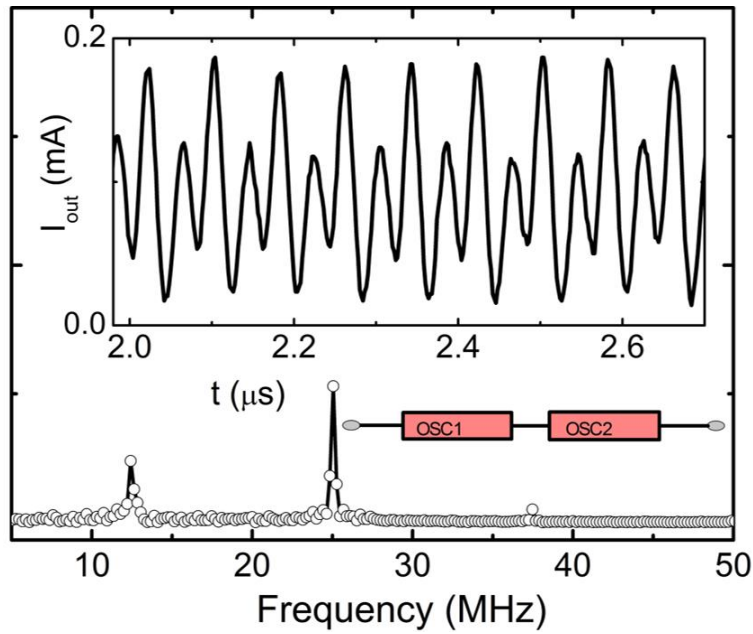
Figure 4.19: Combination of oscillators in parallel. The oscillators were designed using two probe tips on the same film NbO(1). Oscillations produced by a parallel combination of two oscillators (OSC1 // OSC2) are shown in inset and FFT is shown in the main figure.
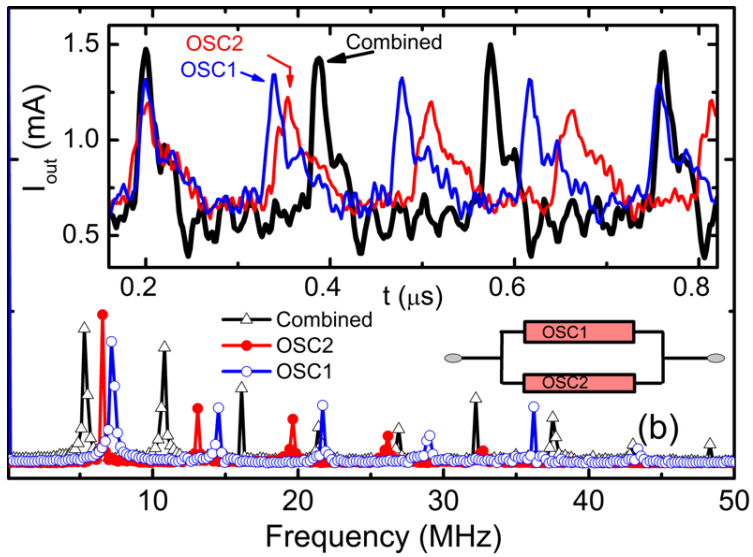
Figure 4.20: Combination of oscillators in series. Oscillations produced by a series combination oscillators OSC1 and OSC2 are shown in inset and FFT is shown in the main figure including individual oscillators.

had higher threshold voltage and, thus, higher range of V_{in} producing oscillations. Other films grown using the NbO_2 target behave similarly to the NbO(1) film with a peak frequency at ~3 V. NbO(1.8), which had a large content of Nb_2O_5, had a smaller frequency than other films.

An experiment performed with NbO(1) film showed that a modification in frequency was possible by combining two oscillators in series and parallel. Two of the probe tips were used to make contacts on the same film and connected in parallel and series circuits as shown in the inset figures. Figure 4.19 shows the output oscillations obtained while combining two oscillators, OSC1 and OSC2, in series as shown in inset figure. FFT shows that the main frequency component was at 25 MHz. Oscillations obtained from the parallel combination of oscillators (Figure 4.20) showed that the resultant frequency of the oscillators after parallel combination became smaller in comparison to the individual ones. By performing the FFT analysis, the first order frequency components were found at 7 and 6 MHz for OSC1 and OSC2, respectively and 5 MHz for combined oscillator as shown in Figure 4.20. It was previously reported that the frequencies of two oscillators coupled in parallel synchronize to a single frequency providing larger stability to the oscillatory system.[131] These oscillatory behaviors are applicable to the current oscillatory antenna and neuromorphic computing.

4.3. EPITAXIAL VS. POLYCRYSTALLINE FILMS: THE ROLE OF DEFECTS

In this section, the electric properties of the devices made from low defect density (epitaxial) and high defect density (polycrystalline) NbO_2 thin films are compared. A polycrystalline film has a higher defect density because of the presence of a large number of domain grain boundaries. The *I-V* characteristics were measured using tungsten tips (Picoprobe)

from GGB Industries Inc. pressed directly on top of the film to avoid contact material from melting and diffusing into the film. The nominal diameter of the probe tip used was 2 µm. The voltage was applied across the thin film at a ramp rate of 0.1 V/sec. The role of defects in thin film switching was investigated in terms of switching stability, switching rapidity and current oscillatory behavior.

4.3.1. I-V Characteristics

Figure 4.21 shows the *I-V* characteristics (10^4 loops) measured on polycrystalline [Figure 4.21(a), (b)] and epitaxial [Figure 4.21(c), (d)] NbO$_2$ films using the probe station tip as a top electrode and TiN [polycrystalline] or Si:GaN [epitaxial] layers as bottom contacts. A clear threshold switching in the current characteristics was observed for both samples. For the polycrystalline film, a large fluctuation in switching characteristics was found during the initial 10^3 cycles, where V_{th} fluctuated by 0.9 V and the leakage current at $V_{th} = 1.8$ V changed by a factor of two [curves labeled by A in Figure 4.21(a)]. V_{th} remained highly stable over the next 10^4 cycles with a 14% fluctuation in leakage current [curves labeled by B in Figure 4.21(b)].

When the compliance current (I_C) was increased from 5 x 10^{-4} to 1 x 10^{-3} A, V_{th} decreased and was stabilized after 500 cycles to a new $V_{th} = 1.2$ V [curves labeled by C in Figure 4.21(b)]. The change in V_{th} was likely due to the elevated substrate temperature due to the higher heat generated by the larger I_C.[106] In contrast, for the epitaxial film no significant fluctuation in V_{th} was found from the beginning of the measurement. The first 10^3 cycles measured with the epitaxial film are plotted in Figure 4.21(c) (curves labeled by A). A 12% variation in leakage current at V_{th} = 2.4 V was observed. For the next 10^4 cycles, the variation in I_{th} increased by 32% at $V_{th} = 2.4$ V, but V_{th} remained unchanged when I_C was increased, in contrast to the polycrystalline film's behavior (curves labeled by B and C in Figure 4.21(d), respectively).
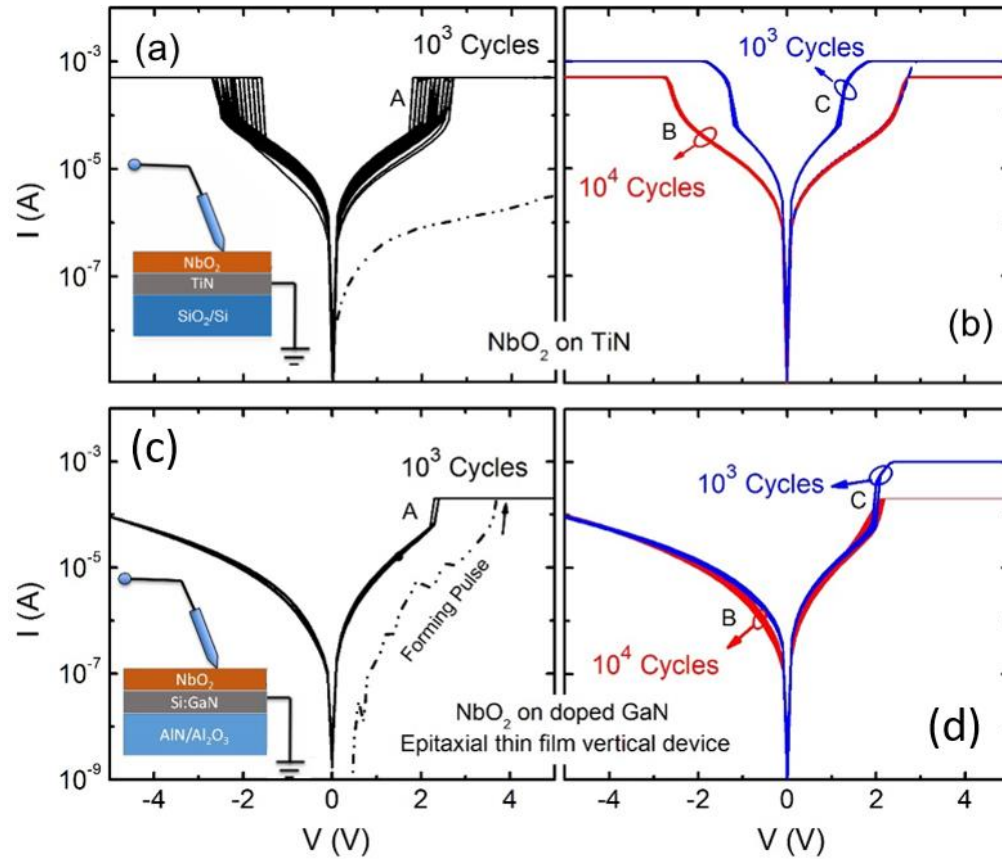
Figure 4.21: *I-V* curves measured using probe station tip at RT in air for the polycrystalline film (a) - (b) and epitaxial film (c) – (d). Inset figures shows sample structures and connection plans. The dotted lines in (a) and (b) are the forming pulses.

Interestingly, no switching was observed during the negative cycles of the *I-V* loops for the epitaxial film, possibly due to a Schottky barrier formation at GaN/NbO$_2$ interface and/or the fact that GaN is a well-known polar material along (0001) orientation. R_{OFF}/R_{ON} ratios of polycrystalline and epitaxial films were 12 and 26, with R_{ON} = 10.3 and 14.9 kΩ, respectively. R_{OFF} and R_{ON} were defined by the inverse slope of the *I-V* curve sections just before and just after switching occurs, respectively.

Both types of films needed a forming pulse [dotted curves in the right insets of Figure 4.21(a) and (c)] which required a forming voltage to switch the device that was higher than the normal switching voltage V_{th}. It is generally assumed that during forming, movement of oxygen vacancies or oxygen atoms causes the formation of a conducting channel, although the exact details of the forming process are still not well understood. It is possible that during the first *I-V* cycle, the temperature of the film material increased due to the current flowing into the device, resulting in a lower V_{th} and higher I_{th}. After 10^4 highly stable *I-V* cycles, no further ionic movement occurred, and only the increase in temperature caused a decrease in V_{th}. It is also possible that a Nb_2O_5 top layer formed after exposure of NbO_2 to air, which acted as an insulating barrier before dielectric breakdown, might be responsible for the forming behavior.[106]

4.3.2. Pulsed I-V Measurement

The circuit diagram for pulsed *I-V* measurement is shown in the inset of Figure 4.22(a) with $R_L = 0$. The regions where the current remained in the 'OFF' and 'ON' states are illustrated by shaded areas in Figure 4.22(a). An abrupt non-linear current switching characteristic was observed for pulse width values 10 μs for the case of the polycrystalline film, whereas for the epitaxial films no abrupt switching was observed. This indicates that grain-boundary-related defects are essential for an abrupt threshold switching behavior. Normalized output pulses for both samples for 2.5 μs are plotted in Figure 4.22(a). The polycrystalline film device switches during both positive and negative cycles with a typical switching time t_{ON} ~ 10 ns, while the turn-off time t_{OFF} was approximately 4 times slower than t_{ON} due to the longer thermal relaxation time while lowering applied voltage.[2] The polycrystalline film device turned on when the input ramp voltage reached $V_{ON} = 1.5$ V. For the epitaxial film, the current remained in the off state during negative pulses of V_{in} and current switching was induced when the input ramp voltage reached 3.5 V.
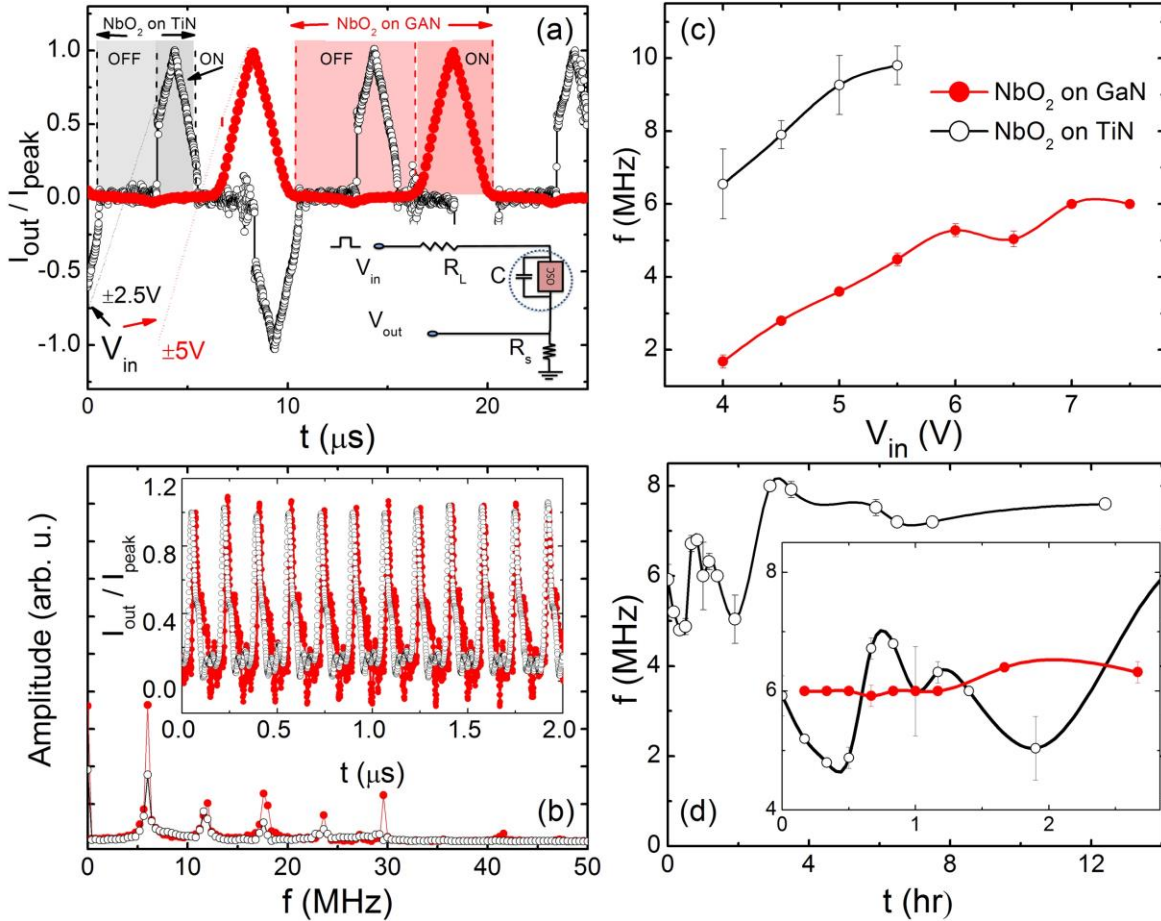
Figure 4.22: (a) *I-V* measurements performed using a triangular waveform for the polycrystalline (○) and epitaxial (●) films. Output currents *I_out* are normalized to I_{peak} = 1.7 mA and 12.3 mA for the polycrystalline and epitaxial films, respectively. Gray- and red-shaded areas indicate on and off states for the polycrystalline and epitaxial films. The inset shows the effective measurement circuit. For the *I-V* measurements, R_L = 0, and R_S = 51 Ω. Input waveforms are shown for the rising side by the dotted lines. (b) Current oscillations and corresponding FFTs showing frequency components measured with R_L = 10 kΩ. Current oscillation amplitudes (*I_out*) are normalized to the first peak I_{peak} = 0.6 mA and 1.2 mA for the polycrystalline and epitaxial films, respectively. (c) Oscillation frequency *f* vs *V_in* and (d) *f* as a function of time *t* for both of the films. Inset in (d) is a zoom for the first 3 hours showing data from both samples.

4.3.3. Self-Sustained Current Oscillation

Self-sustained current oscillations in both type vertical devices were also measured using the circuit diagram in Figure 4.22(a) with $R_L = 10$ kΩ and a sense resistor $R_S = 51$ Ω. In the diagram, the sample is shown as a switchable resistor connected to a parallel capacitor, representing the intrinsic capacitance of the insulating (OFF) state. A low frequency input voltage (V_{in}) with a rectangular wave shape was applied and the output signal (i.e. current) was determined from the voltage drop across R_S. Figure 4.21(b) shows the normalized output current characteristics from both samples having a 6 MHz oscillation frequency while applying rectangular pulses. Frequency components obtained using a fast Fourier transform (FFT) are also shown in Figure 4.22(b) and the frequency of the first harmonic f as a function of the input voltage V for both devices is plotted in Figure 4.22(c). Polycrystalline films had self-sustaining oscillations in the input voltage range of 4 to 5.5 V with the frequency ranging from 6 to 9.8 MHz. For the epitaxial film, the voltage range that produced oscillations was much larger, from 2.5 to 8 V. The frequencies produced by the epitaxial film were smaller than those of the polycrystalline film, but the frequency was better defined for the epitaxial film, as illustrated by the sharper and larger peaks of the epitaxial film in the FFT spectra [Figure 4.22(b)]. In addition, the frequency produced by the polycrystalline film was found to be unstable during the first 3 hrs of operation. After 3 hrs, the frequency increased and stabilized. On the other hand, oscillations remained constant over time for the epitaxial film device. This indicated that the low defect density and high crystalline quality of NbO_2 films grown on GaN guaranteed stable threshold current switching.

The initial fluctuations of the *I-V* characteristics [in Figure 4.21(a)] and oscillation frequency of the polycrystalline film [in Figure 4.22(d)] can be explained using the learning mechanism proposed by Matveyev et al.[118] for the case of HfO_2-based synaptic devices. During

learning, readjustment in oxidation state or vacancy concentration over time leads the system to the corresponding value of V_{th} or oscillation frequency. Thermal equilibrium is also important to stabilize the *I-V* characteristics. An increase in I_C, for example, requires an additional adjustment of V_{th}, as shown in Figure 4.21(a), where V_{th} decreases due to the elevated film temperature induced by the higher current. Epitaxial films required no initial learning and had stable threshold switching and current oscillations.

CHAPTER 5

CONCLUSIONS

NbO$_2$ thin films were prepared using PLD and their structural and electrical properties were thoroughly characterized. Films grown on Al$_2$O$_3$ (0001) and GaN/Al$_2$O$_3$ substrates grew epitaxially with single phase NbO$_2$ (110)$_T$ out of plane orientation. The oxidation state of Nb was controlled by the total growth pressure of the O$_2$/Ar mixture. X-ray diffraction (XRD) and x-ray photoelectron spectroscopy (XPS) analysis confirmed the formation a pure phase NbO$_2$ and major phase Nb$_2$O$_5$ in the films grown in 1 and 20 mTorr total growth pressure, respectively. Optical band gap measurements performed with the film grown on Al$_2$O$_3$ showed the material had a band gap of 0.6 eV. Current-voltage measurements of two terminal lateral devices showed reversible threshold resistance switching behavior with switching fields of approximately 2.2 x 10^6 V/m and 34.6 x 10^6 V/m for films with predominant NbO$_2$ and Nb$_2$O$_5$ phases, respectively. The stoichiometric and epitaxial NbO$_2$ thin films showed volatile threshold resistance switching while Nb$_2$O$_5$ films exhibited irreversible phase transformation when relatively large electric fields were applied. Pulsed field-measurements yielded typical switching times above 1 ms in lateral devices made of NbO$_2$. Using pulsed-width dependent *I-V* measurement and a simultaneous measurement of the sample temperature, the Joule heating threshold switching mechanism was verified.

Polycrystalline NbO$_2$ thin films grown on TiN coated SiO$_2$/Si substrate were also investigated. The polycrystalline films were also grown using PLD and structural quality was verified using both θ-2θ XRD and grazing incidence x-ray diffraction (GIXRD). The *I-V*

measurements showed that threshold switching voltage (V_{th}) had thickness dependence and the conduction mechanism in the insulating state was mainly governed by trap-charge assisted PF-conduction mechanism. Contact size dependent *I-V* measurements confirmed that the conductivity of the device did not depend on local filamentary pathways. The pulsed *I-V* measurements performed with as grown sample showed a current switching time of 20 and 80 ns while switching the device on and off respectively. Also, self-oscillatory current behavior with oscillations frequencies greater than 5 MHz were obtained depending on the input voltage and defect density present in the film.

Finally, the current switching behavior produced by an epitaxial film and a polycrystalline film grown using similar growth conditions was compared. Threshold switching, as well as current oscillation characteristics, were found to be more stable in epitaxial films having low defect density.

The current switching in NbO_2 was induced by Joule heating produced by applied electric field rather than the applied field itself. The slow transitions, in the case of both lateral and vertical epitaxial thin film devices, indicated that the insulator-to-metal transition occurred due Peierls type second order structural transitions. In the case of polycrystalline thin film devices, switching phenomena were likely controlled by ionic or vacancy movement assisted leakage current.

REFERENCES

1. M. D. Pickett, G. Medeiros-Ribeiro and R. S. Williams, *Nat. Mater.* **12**, 114 (2013).
2. M. D. Pickett, R. S. Williams, *Nanotechnology* **23**, 215202 (2012).
3. K. Jung, Y. Kim, W. Jung, H. Im, B. Park, J. Hong, J. Lee, J. Park, and J-K. Lee, *Appl. Phys. Lett* **97**, 233509 (2010).
4. J. Bae, I. Hwang, Y. Jeong, S.-O. Kang, S. Hong, J. Son, J. Choi, J. Kim, J. Park, M.-J. Seong, Q. Jia and B.H. Park, *Appl. Phys. Lett* **100**, 062902 (2012).
5. S. Kim, J. Park, J. Woo, C. Cho, W. Lee, J. Shin, G. Choi, S. Park, D. Lee, B. H. Lee, H. Hwang, *Microel. Eng.* **107**, 33 (2013).
6. S. Spiga, A. Lamperti, C. Wiemer, M. Perego, E. Cianci, G. Tallarida, H. L. Lu, M. Alia, F. G. Volpe, M. Fanciulli, *Microelectronic Eng.* **85**, 2414 (2008) .
7. X. Liu, S. Md. Sadaf, S. Kim, K. P. Biju, X. Cao, M. Son, S. H. Chaudhury, G. Gung and H. Hwang, *ECS Solid St. Lett.* **1**, Q35 (2012).
8. F. J. Wong, S. Ramanathan, *J. Mater. Res.* **28**, 2555, (2013).
9. B. Posadas, A. O'Hara, S. Rangan, R. A. Bartynski and A. A. Demkov, *Appl. Phys. Lett.* **104**, 092901 (2014).
10. F. J. Wong, N. Hong, S. Ramanathan, *Phys. Rev. B* **90**, 115135 (2014).
11. Z. Weibin, W. Weidong, W. Xueming, C. Xinlu, Y. Dawei, S. Changle, P. Liping, W. Yuying and B. Li, *Surf. Interface Anal.* **45**, 1206 (2013).
12. F. J. Morin, *Phys. Rev. Lett. 3, 34 (1959)*.
13. J. Jeong, N. Aetukuri, T. Graf, T.D. Schladt, M. G. Samant, S. P. Parkin, *Science* **339**, 1402 (2013).
14. J.B. Torrance, P. Lacorre, A. I. Nazzal,E. J. Ansaldo, and Ch. Niedermayer, *Phys. Rev. B* **45**, 8209 (1992).
15. M. Imada, A. Fujimori, and Y. Tokura, *Rev. Modern Phys.* **70**, 1039 (1998).
16. A. Bolzan, C. Fong, and B. J. Kennedy, *J. Solid St. Chem.* **113**, 9, (1994).
17. Y. Sakai, N. Tsuda, and T. Sakata, J. Phys. Soc. Jpn 54, 1514 (1985).
18. K. L. Chopra, *IEEE* **51**, 941 (1963).
19. D. V. Geppert, IEEE 51, 223 (1963).
20. G. Dearnaley, D. V. Morgan, and A. M. Stoneham, *J. Non-Cryst. Solids* **4**, 593 (1970).
21. F. A. Chudnovskii, L. L. Odynets, A. L. Pergament, and G. B. Stefanovich, *J. Solid State Chem.* **122**, 95 (1996).
22. H. R. Phillipp, and L. M. Levinson, *J. Appl. Phys.* **50**, 4814 (1979).
23. J. C. Lee, W. W, Durand, *J. Appl. Phys* **56**, 3350 (1984).

24. S. H. Shin, T. Halpern, and P. M. Raccah, *J. Appl. Phys.* **48**, 3150 (1977).

25. J. G. Simmons and R. R. Verderber, *Proc. R. Soc. A*, **301**, 77 (1967).

26. L. Chua, IEEE Trans., *Circuit Theory*, **18**, 5, 507 (1971).

27. G. Dearnale, A. Stoneham, and D. Morgan, *Rep. Prog. Phys.*, **33**, 1129 (1970).

28. A. Beck, J. G. Bednorz, C. Gerber, C. Rossel, and D. Widmer, *Appl. Phys. Lett.*, **77**, 139 (2000).

29. V. V. Zhirnov, R. K. Cavin, J. A. Hutchby, and G. I. Bourianoff, *Proc. of the IEEE* **91**, 1934 (2003).

30. X. Liu, S. M. Sadaf, M. Son, J. Shin, J. Park, J. Lee, S. Park, and H. Hwang, *Nanotech.* **22**, 475702 (2011).

31. J. J. Yang, M. D. Pickett, X. Li, D. A. A. Ohlberg, D. R. Stewart, and R. S. Williams, *Nat. Nanotech.* **3**, 429 (2008).

32. E. Linn, R. Rosezin, C. Kugeler, and R. Waser, Nat. Mat. **9**, 403 (2010).

33. Y. Li, Y. Zhong, L. Xu, J. Zhang, X. Xu, H. Sun, X, Miao, *Scientific Reports*, 3: 1619, DOI: 10.1038/srep01619.

34. S. Hyun Jo, K-H Kim, T. Chang, S. Gaba, W. Lu, *Proceedings of 2010 IEEE International Symposium on Circuits and Systems,* pp. 13-16 (2010).

35. S. Balatti , S. Larentis , D. C. Gilmer , and D. Ielmini, Adv. Mater. **25**, 1474 (2013).

36. Y. Zhou, S. Ramanathan, *Proceeding of the IEEE* **103**, 1289 (2015).

37. P. Lacorre, J. B. Torrance, J. Pannetier, A. I. Nazzal, P. W. Wang and T. Huang, *J. Solid State Chem.* **91**, 225 (1991).

38. G. Thornton, F.C. Morrison, S. Partington, B.C. Tofield, D.E. Williams, *J. Phys. C: Solid State Phys.* **21**, 2871 (1988).

39. J. Sebastian, D. Seidman, K. Yoon, P. Bauer, T. Reid, C. Boffo, and J. Norem, *Physica C* **441**, 70 (2006).

40. A. K. Cheetam, C. N. R. Rao, *Acta Crystallogr*. B **32**, 1579 (1976).

41. Q. Ma and R. A. Rosenberg, *Appl. Surf. Sci.* **206**, 209 (2003).

42. J. K . Hulm, C. K. Jones, R. A. Hein, J. W. Gibson, *J. of L.T. Phys.* **7**, 291 (1972).

43. C. Carlisle, T. Fujimoto, W. Sim, and D. King, *Surf. Sci.* **470**, 15 (2000).

44. G. Thornton, A. F. Orchard, and C. N. R. Rao, Phys. Lett. 54, 235 (1975).

45. C. Nico, T. Monteiro, M. P. F. Graca, *Prog. In Mat. Sc.* **80**, 1 (2016).

46. J. Halbritter, *Appl. Phys. A* **43**, 1 (1987).

47. R. Pynn, J. Axe, and R. Thomas, *Phys. Rev. B* **13**, 2965 (1976).

48. G. Samsonov, The Oxide Handbook (*IFI/Plenum, New York,* 1973).

49. T. Hurlen, *J. Inst. Metals.* **89**, 273 (1961).

50. H. Schäfer, R. Gruehn, F. Schulte, *Angew. Chem. internat. Edit.* **5**, 40 (1966).

51. G. Brauer, Z. *Anorg. Chem.* 248, 1 (1941).

52. L.K. Frevel, H.W. Rinn, *Analyt. Chem.* **27**, 1329 (1955).

53. J.L. Waring, R.S. Roth, H.S. Parker, *J. Res. Natl. Bur. Stand.* **77**A, 705 (1973).

54. V. Eyert, *Euro. Phys. Lett.* **58**, 851 (2002).

55. C. Weber, D. D. O'Regan, N. D. M. Hine, M. C. Payne. G. Kotliar, and P. B. Littlewood,

Phys. Rev. Let. **108**, 256402 (2012).

56. A. O'Hara, A. A. Demkov, *Phys. Rev. B* **91**, 094306 (2015).

57. N. F. Mott, *Rev. of Modern Phys.* **40**, 677 (1945).

58. R. E. Peierls, Quantum Theory of Solids, *Oxford University* Perss (1955).

59. J. B. Goodenough, *Phys. Rev.* **117** 1442 (1960).

60. N. Beatham, and A. F. Orchard, Journal of Electron and Related Phenomena 16, 77 (1979).

61. T. M. Rice, H. Launois and J. P. Pouget, *Phys. Rev. Lett.* **73** 3042 (1994).

62. C. N. Berglund And H. J. Guggknhkim, *Phys. Rev.* **185**, 1022 (1969).

63. K. Sakata, *J. Phys. Soc. Japan* **26**, 582 (1969).

64. R. M. Wentzcovich, W. W. Schulz and P. B. Allen, *Phys. Rev. Lett.* **72 ,**3389 (1994).

65. D. Adler and H. Brooks, *Phys. Rev.* **155** 826 (1967).

66. G. Stefanovich, A. Pergament and D. Stefanovich, J. Phys., *Condens. Matter* **12** (2000) 8837–8845.

67. H-T. Kim, B.-G. Chae, D.-H. Youn, G. Kim, and K-Y. Kang, *Appl. Phys. Lett.* **86**, 242101 (2005).

68. B-J Kim, Y W Lee, S Choi, J-W Lim, S J Yun, and H T Kim, *Physical Review B* 77, 235401 (2008).

69. J. S. Lee, M. Ortolani, and U. Schadea, Y. J. Chang and T. W. Noh, *Appl. Phys. Lett.* **90**, 051907 (2007).

70. J. Duchene, M. Terraillion, P. Pailly, and G. Adam, *Appl. Phys. Lett.* 19, 115 (1971).

71. A. Zimmers, L. Aigouy, M. Mortier, A. Sharoni, S. Wang, K. G. West, J. G. Ramirez, I. K. Schuller, *Phys. Rev. Lett.* **110**, 056601 (2013).

72. R. F. Jennick, and D. H. Whitemore, *J. Phys. Chem. Solids* **27**, 1183 (1966).

73. S. Slesazeck, H. M̈ahne, H. Wylezich, A. Wachowiak, J. Radhakrishnan, A. Ascoli, R. Tetzlaff, and T. Mikolajick, *RSC Adv.* **5**, 102318 (2015).

74. K. Simeonov, D. Lederman, *Surface Science* **603**, 232 (2009).

75. D. H. Lowndes, D. B. Geohegan, A. A. Puretzky, D. P. Norton and C. M. Rouleau, *Science* **273**, 898 (1996).

76. M. Stafe, A. Marcu, N. N. Puscas, Pulses Laser Ablation of Solids: Basic Theory and Application, *Springer Series in Surface Science*, Vol. **53** (2014).

77. D. B. Chrisey and G. K. Hubler, Pulsed Laser Deposition of Thin Films (*New York: John Wiley & Sons*) (1994).

78. A. Ichimiya, and P. I. Cohen Reflection High Energy Electron Diffraction, *Cambridge University Press*, Cambridge, UK (2004).

79. Z. Zhu, X.J. Zheng, W. Li, Physica B 403, 4074 (2008).

80. M. Lagally, Methods of Experimental Physics **22**, 237 (*Academic Press*, NY, 1985).

81. M. C. Lagally, and D. B. Savage, *MRS Bull.*, **18**, 24 (1993).

82. G. Rijnders, D. H. A. Blank, *Appl. Phys. Lett* **84**, 505 (2004).

83. T. Kojima, N. J. Kawai, T. Nakagawa, K. Ohta, T. Sakamoto, and M. Kawashima, *Appl. Phys. Lett.* **47**, 286 (1985).

84. W. H. Bragg, *Proc R. Soc. Lond. A*. **88** 428 (1913).

85. H. P. Myers, Introductory Solid State Physics, *Taylor-Francis,* Philadelphia, 1997.

86. C. Giacovazzo, Fundamentals of Crystallography, *Oxford Science Publications*, New York, 2002.

87. H. Ibach and H. Lüth, Solid State Physics: An Introduction to Principles of Materials Science, *Springer*, Berlin 1995.

88. B. E. Warren, X-Ray Diffraction, *Dover Publications, Mineola*, 1990.

89. C. Suryanarayan and M. G. Norton, X-ray Diffraction: A Practical Approach, Plenum Press, 1998.

90. J. McChesney, M. Hetzer, H. Shi, T. Charlton, and D. Lederman, J. Mater. Res. 16, 1769 (2001).

91. P. Scherrer, Gottinger Nachrichten **191**8, 98 (1918).

92. E. Fullerton, I. K. Schuller, H. Vanderstraetan, and Y. Bruynseraede, *Phys. Rev. B* **45**, 9292 (1992).

93. M. Bjo¨rck and G. Andersson, *Journal of Applied Crystallography* **40**, 1174 (2007).

94. D. Grier and G. McCarthy, North Dakota State University, Fargo, ND, ICDD Grand-in-Aid (1991).

95. C. D. Wagnr, W. M. Riggs, L. E. Davis, J. F. Moulder, G. E. Muilengerg, Handbook of x-ray photoelectron spectroscopy, *Perkin-Elmer Corp.*, (1979).

96. *http://www.ggb.com/PdfIndex_files/mod7.pdf*.

97. *https://www.asylumresearch.com/Applications/Orca/ORCADSHR.pdf*.

98. B. Capella, G. Dietler, *Surface Sc. Reports* **34**, 1, 1999.

99. G. Binning, and C. F. Quate, *Phys. Rev. Lett.* 56, 930 (1986).

100. P. Eaton and P. West, Atomic Force Microscopy, *Oxford University Press*, 2010.

101. Y. Wang, R. B. Comes, S. Kittiwatanakul, S. A. Wolf, and J. Lu, J. Vac. Sci. Technol. A 33, 021516 (2015).

102. T. Hadamek, A. B. Posadas, A. Dhamdhere, D. J. Smith, and A. A. Demkov, J. Appl. Phys. 119, 095303 (2016).

103. T. Joshi, T. R. Senty, P. Borisov, A. D. Bristow, and D. Lederman, J. Phys. D: Appl. Phys. 117, 013908 (2015).

104. A. Darlinski and J. Halbritter, *J. Vac. Sci. Technol.* A **5,** 1235 (1987).

105. S. A. Chambers, Y. Gao, S. Thevuthasan, Y. Liang, N. R. Shivaparan and R. J. Smith, *J. Vac. Sci. Technol.* A **14** 1387 (1992).

106. *Y.* Gao, Y. Liang and S. A. Chambers, *Surf. Sci.* **348,** 17 (1996).

107. D. D. Sarma and C. N. R. Rao, *J. Electron Spectrosc. Relat. Phenom.* **20,** 25 (1986).

108. D. Adler, *Rev. Mod. Phys.* **40,** 714 (1997).

109. Kurmaev E Z, Moewes A, Bureev O G, Nekrasov I A, Cherkashenko V M, Korotin M A and Ederer D L, *J. Alloys Compd.* **347,** 213 (2002).

110. G. Agrawal and G. B. Reddy, *J. Mater. Sci.: Mater. Electron.* **16,** 21 (2005).

111. J. I. Pankove, *Optical Processes in Semiconductors* (Englewood Cliffs, NJ: Prentice-Hall) (1971).

112. T. Detchprohm, K. Hiramatsu, K. Itoh and I. Akasaki, *Japanese Journal of Applied Physics* **31**, 1453 (1992).

113. Y. Wang, R. B. Comes, S. A. Wolf, and J. Lu, *J. of the Electron Device Society* **4**, 11 (2016).

114. E. Cha, J. Park, J. Woo, D. Lee, A. Prakash, and H. Hwang, *Appl. Phys. Lett.* **108**, 153502 (2016).

115. E. Cha, J. Woo, D. Lee, S. Lee, J. Song, Y. Koo, J. Lee, C.G. Park, M.Y. Yang, K. Kamiya, K. Shiraishi, B. Magyari-Kope, Y. Nishi, and H. Hwang, in 2013 IEEE Int. Electron Devices Meet. IEEE, 2013, pp. 10.5.1.

116. S. Li, X. Liu, S. K. Nandi, D. K. Venkatachalam, and R. G. Elliman, *Appl. Phys. Lett.* **106**, 212902 (2015).

117. D. J. Wouters, R. Waser, and M. Wuttig, *Proceedings of the IEE* **103**, 1274 (2015).

118. J. Cao, W. Fan, H. Zheng and J. Wu, *Nano Lett.* **9,** 4001 (2009).

119. R. F. Janninck and D. Whitmore, *J. Phys. Chem. Solids* **27** 1183 (1965).

120. X. Liu, S. K. Nandi, D. K. Venkatachalam, K. Belay, S. Song and R. G. Elliman, *IEEE Electron Device Lett.* **35** 1055 (2016).

121. M. D. Pickett, J. Borghetti, J. J. Yang, G. Medeiros-Ribeiro and R. S. Williams, *Adv. Mater.* **23** 1730 (2011).

122. D. Ielmini and C. Cagli, *Nanotachnology* **22**, 254022 (2011).

123. M. Kang, S. Yu and J. Son, J. Phys. D: Appl. Phys. 48, 095301 (2015).

124. D. J. Wouters, R. Waser, and M. Wuttig, *Proceedings of the IEE* **103**, 1274 (2015).

125. I. H. Inoue, S. Yasuda, H. Akinaga, and H. Takagi, *Phys. Rev. B* **77**, 035105 (2008).

126. R. Meyer, L. Schloss, J. Brewer, R. Lamberson, W. Kinney, J. Sanchez, and C. Rinerson, NVMTS (2008).

127. A. Ongaro, A. Pillonnet, *IEEE Proceeding*, **138**, 127 (1991).

128. M. Son, J. Lee, J. Park, J. Shin, G. Choi, S. Jung, W. Lee, Se. Kim, S. Park, and H. Hwang, *IEEE Electron Device Letters*, **32**, 1579 (2011).

129. S.-E. Ahn, M.-J. Lee, B. S. Kang, D. Lee, C.-J. Kim, D.-S. Kim, and U-I. Chung, *IEEE Transactions on Nanotechnology* **11**, 6 (2012).

130. R. Muenstermann, R. Dittmann, K. Szot, S. Mi, C.-L. Jia, P Meuffels, and R Waser, *Appl. Phys. Lett.* **93**, 023110 (2008).

131. I. G. Beak, M. S. Lee, S. Seo, M. J. Lee, D. H. Seo, D.-S. Suh, J. C. Park, S. O. Park, H. S. Kim, I. K. Yoo, U-In. Chang, and J. T. Moon, Electron Device Meeting, 2004, IEEE.

132. H. Sim, H. Choi, D. Lee, M. Chang, D. Choi, Y. Son, E.-H. Lee, W. Kim, Y. Park, I-K. Yoo, and H. Hwang, *IEEE* 2005.

133. J. Y. Son and Y.-H. Shin, *Appl. Phys. Lett.* **92**, 222106 (2008).

134. H. Shima, F. Takano, H. Akinaga, Y. Tamai, I. H. Inoue, and H. Takagi, *Appl. Phys. Lett.* **91**, 012901 (2007).

135. G. Wang, C. Li, Y. Chen, Y. Xia, Di Wu, Q. Xu, Scientific Reports 6:36953 (2016).

136. A. Prakash, S. Maikap, W.-S. Chen, H.-Y. Lee, F. Chen, T-C Tien, C.-S. Lai, and M.-J. Tsai, IEEE Transactions on Nanotechnology 13, 409 (2014).

137. K. Szot R. Dittmann, W. Speier, and R. Waser, *Phys. Stat. Sol. (RRL)* **1**, No. 2 (2007).

138. J. Frenkel, Phys. Rev. 54, 647 (1938).

139. S. O. Pearson, and H. S. G. Anson, Proc. Phys. Soc. Lon. 34, 175.

140. B. Ialevic and M. Shoga, *Thin solid films*, **75**, 199 (1981).

141. N. Shukla, A. Parihar, E. Freeman, H. Paik, G. Stone, V. Narayanan, H. Wen, Z. Cai, V. Gopalan, *Scientific Reports* **4**, 4964 (2014).

142. Y. Matveyev, R. Kirtaev, A. Fetisova, S. Zakharchenko, D. Negrov, and A. Zenkevich, *Nanoscale Research Letters* **11**, 1 (2016).